# Timber Grid-shell Structures: form-finding, analysis and optimisation

**Bernardino D'Amico**
**Ph.D.**

**2015**

# Timber Grid-shell Structures: form-finding, analysis and optimisation

*by*

**Bernardino D'Amico**

*Thesis*

*submitted in partial fulfilment*

*of the requirements of*

**Edinburgh Napier University**

*for the award of*

*Doctor of Philosophy*

**August 2015**

# Declaration

I hereby declare that: this work has been entirely carried out by myself at the Edinburgh Napier University and contains no material that have been accepted for the award of any other degree or diploma in any other University. To best of my knowledge, this thesis contains no material previously written by another person, except where due reference is provided in regard.

(Bernardino D'Amico)

Signature 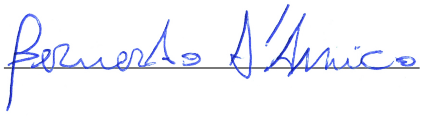

Date _____

*"If we assume the equations of Structural Mechanics, by considering the stresses as known data and the structural geometry as the unknown of the problem, we will make a step forward, toward a new way of using our scientific heritage."*

Sergio Musmeci

# Contents

# List of Figures

# List of Tables

# Abstract

This thesis aims to provide a set of tools for analysis and design of free-form timber grid-shells. It provides a brief introduction on the relationship between shape and structural behaviour of grid-shells, followed by an introduction to actively-bent structural systems. The design issues are then individuated and three main themes are defined, namely: Form-finding, Structural Analysis and Optimisation. The development and use of a numerical framework, based on a six Degree-of-Freedom (DoF) co-rotational beam-element in conjunction with the Dynamic Relaxation method, has formed the basis, on which a unified procedure for the Form-finding and Structural Analysis tasks are defined.

A two-step analysis procedure allows setting a target shape for the grid-shell with the aid of a reference surface, whilst taking into account the effect of internal (bending) reactions on the final geometry. Coupling constraints are numerically simulated by development of a single-node cylindrical joint. An algorithm for grid cutting (mesh manipulation) is described, as well as a modified co-rotational beam-element, based on assumption of 'equivalent' bending stiffness. The modified formulation allows taking into account the change in stiffness of the double-layer members, when passing from the Form-finding to the analysis of the structure under working loads, by simply setting a dimensionless parameter. A numerical framework for optimisation of the members' cross-section is then introduced. The optimisation problem is decomposed in two main sub-problems, to be separately solved by iterative techniques: The seeking of an 'allowable' thickness, for the laths under bending action, is pursued with a procedure based on Newton-Raphson method, whilst: a local-search approach is used to find (for a given load configuration) the optimal variation in thickness of the composite cross-section. The proposed methods are validated by several numerical and full-size experimen-

tal test, as well as comparison with the corresponding analytical solution, where available.

# Acknowledgements

It is out of question, for a PhD candidate not to acknowledge his/her supervisor, and my case makes no exception; notwithstanding, I want to thank my supervisor Professor Abdy Kermani, for all the experienced support, advices and constant availability he provided throughout the development of this research work. But most important, I thank him for consenting me to develop my own ideas, by never posing boundaries a-priori, but rather indicating the way to prove the validity of an hypothesis or idea. Ultimately, he taught me how to carry out original research in an independent way, and this is undoubtedly the best thing I could have learned.

I thank my co-supervisor Dr Hexin (Johnson) Zhang, for making available to me his experience and outstanding knowledge in the field of Structural Engineering and Computation. Also, I thank him for such a kind attitude with which he assisted me throughout my research.

I thank Dr Jack Porteous, who through his master's course on Structural use of timber, provided me a deep understanding of the backgrounds upon which Design-code's requirements and rules are based.

I thank Dr Paul Shepherd and Professor Chris Williams, for all the invaluable feedbacks and suggestions they provided me. I can say without any doubt, it has been an honour and a privilege for me to have managed having them involved into my research. I must pay a special thank to Paul, who roughly three years ago invited me to Bath, and over a cup of coffee, pointed out to me about the opportunity for a PhD on free-form timber structures in Edinburgh. It is somehow also because of him if this piece of work came to life.

I cannot forget to thank Professor Sergio Pone, that with his work on grid-shells, in some way started all this journey. I still remember when, about six years ago, I went to his office in Naples, looking to join his group and learn about timber

grid-shells.

Acknowledgements are also extended to the Edinburgh Napier University, in particular to the School of Engineering and the Built Environment, which provided financial support for this research. A thank also to my colleague-room and friend Olubukola (Bukky) Tokede, for his cheerfulness attitude by which he kept high the moral in the room, especially during those dark Nordic winter afternoons.

# Chapter 1

# Introduction

The final goal of this thesis is to provide a 'hands-on' tool-set of computational methods, to address practical issues usually involved with the design and structural analysis of free-form timber grid-shells, with particular focus on (so-called) *actively bent* structures.

Prior to describing such methods, it may be worth in here to introduce some very basic concepts about the shape and structural behaviour of grid-shells (and shells in general), in first instance, to provide a better understanding on how shells work, and ultimately, to allow for a 'conscious' use of the tools under description when modelling 'free' and 'proper' grid-shell shapes.

## 1.1 How does a shell work?

By assuming the 'shape' as main parameter to distinguish shells from other kinds of structures: a shell is indeed a three-dimensional object having one dimension (thickness) much smaller than the other two, which from a geometrical point of view, makes it assimilable to a surface. Further aspects however, needs to be considered in order to exclude planar structural systems (such as plates, slabs, and

**Figure 1.1:** Great court grid-shell roof at the British Museum. Photo by David Iliff. (License: CC-BY-SA 3.0).

*developable* surfaces in general) from this category. It can be stated that: a shell is a structural system working prevalently in *membrane* action. Let's consider for instance a barrel vault with a *funicular* profile (see Figure 1.2a). Thanks to the chosen profile (an inverted hanging chain) under uniformly distributed vertical load, the vault experiences a compression-only stress distribution, assimilable to a membrane-like behaviour. If we consider now, for the same vault, an unevenly distributed load (e.g. due to wind action on one side of the vault only) in such a case, bending stress arises along the shell's cross-section, corresponding to a variation of normal stress between the extrados and intrados of the vault. Accordingly, the previously manifested membrane-like behaviour, is lost.

Let's consider now a barrel vault with a funicular and corrugated profile (see Figure 1.2b). Under lateral wind load, in-plane shear forces will arise along the

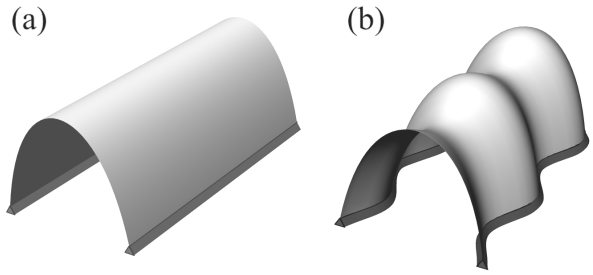


**Figure 1.2:** Funicular barrel vault: (a) Constant profile; (b) Corrugated profile.

surface of the shell as a combination of tension and compression. Consequently, the *inextensional* deformations associated with the bending out of the plane are somehow 'replaced' by *extensional* deformations in the plane of the corrugated barrel vault.[1] In other terms: providing a 'certain' amount of double curvature (corrugation) assures for the structure to work in membrane action even in case of unevenly distributed loads.

In addition to the use of non-developable surfaces, a further aspect to consider when shaping a shell (or grid-shell) structures, is the definition of proper boundary conditions. Since boundaries represent a discontinuity of the shell's surface, for normal-to-surface applied loads, the membrane distribution of forces is likely to be lost. Therefore, unless a 'closed' surface is taken into account, (e.g. a whole sphere) proper supports need to be added at the boundaries to provide that stiffness, which: preventing the shell to locally displace out of the plane (inextensional deformations) it rehabilitates the 'open' structural shape from being a *mechanism*[2] to become a *statically determinate* system.

[1] A quantitative assessment, of the effect of double curvature on the load carrying capacity of corrugated barrel grid-shell vaults, was carried out by Malek et al. [2013] according to which corrugation allows to increase the buckling load up to eight times for less than 3% increase of volume.

[2] From Statics: a structure is a *mechanism* when the total number of Degrees of Freedom is greater than the total number of Constraints.

**Figure 1.3:** Heinz Isler: Wyss Garten Haus, Zuchwil, Switzerland, 1962.

In this regard, see for instance the concrete shell shown in Figure 1.3: the four cantilevers placed normal to the shell surface (sidewise the openings) in addition to increasing the covered area, they provide out-of-plane stiffness, necessary to avoid inextentional deformations.

An insight, of the effect of boundary conditions/supports on shells' behaviour, is provided by Hoogenboom [2014] with the following 'real-life' example: Figure 1.4a shows a simply supported spherical cap subjected to point load. When pressing the cap, the load is primarily carried by forces in the plane of the surface while only a small part is carried out by bending. Since the shell is undergoing extensional deformations (up to the point of snap-through) a stiff behaviour is experienced by the person applying the load. On the contrary, by applying this time the load on the shell free from its supports (Figure 1.4b) inextensional deformations occur: most of the load is carried by bending (whilst only a small part by in-plane forces) and the person feels that the shell is not stiff at all.

For a more exhaustive understanding of the topic, the reader is referred to Chapter three (*What is a shell?*) of Adriaenssens et al. [2014], whilst *Theory of shell structures* by Calladine [1989] is an authoritative source on the mechanics of shell structures.

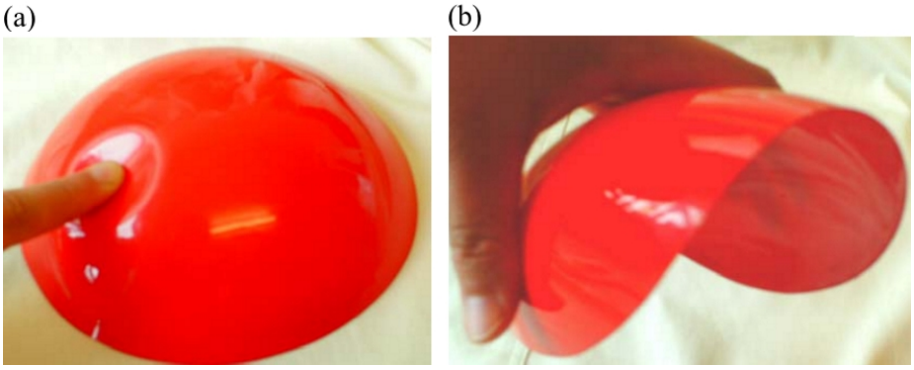


**Figure 1.4:** Spherical cap [Hoogenboom, 2014]: (a) *Extensional* deformations – snap-through; (b) *Inextensional* deformations.

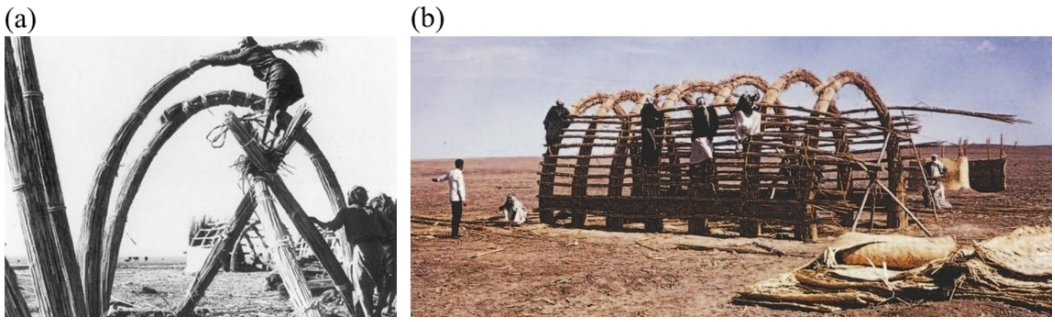


**Figure 1.5:** Iraqi Mudhif: (a) Image source: Oliver and Press [2003]; (b) Image source: Ochsenschlager [1998].

## 1.2 Actively bent grid-shells

According to Lienhard et al. [2013] the term 'Active-Bending' refers to those design cases in which the structural shape is obtained as a result of bending frameworks/assemblies of elastic members such as (but not limited to) rods or beams. Examples of constructing shelters and huts 'by bending' branches, sticks or laths, probably date back to prehistoric times.

Excepting those episodes of vernacular architecture, as for instance, the iconic Mongolian *Yurt*, or the Iraqi *Mudhif* (see Figure 1.5) design solutions, in which

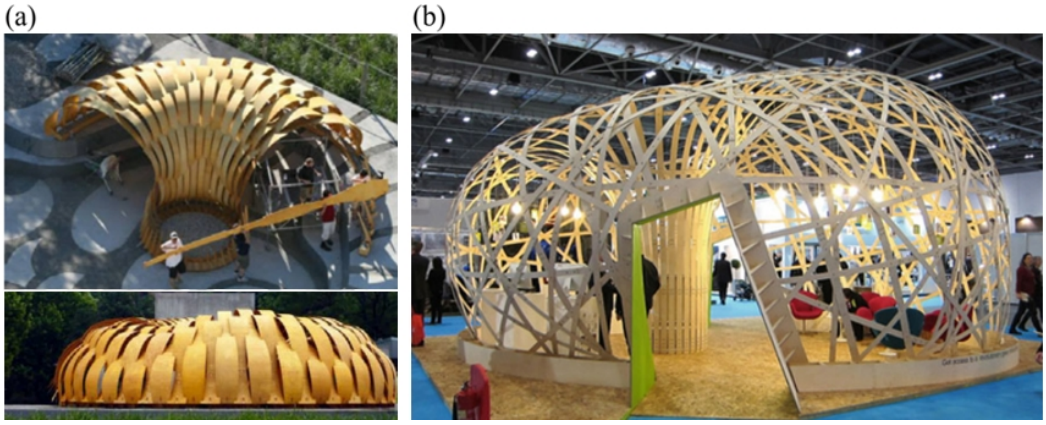


**Figure 1.6:** Active-Bending structures: (a) ICD/ITKE pavilion [Fleischmann and Menges, 2012]; (b) Ongreening pavilion [Harding et al., 2015].

bending has been used as a self-forming process, are fairly recent. Particularly, in the last few years, an increasing number of (actively bent) experimental pavilions have been built by academics/professionals, such as: [Fleischmann and Menges, 2012, Nicholas et al., 2013, Naicu et al., 2014, Harding et al., 2015].

A clear statement, on the 'benefits' of using Active-bending systems, is given by Gengnagel et al. [2013] according to which:

*"The advantage of elastically bent elements is that the production process is potentially identical for all elements, regardless of their curvature. The transportation of straight profiles is easier owing to volume reductions. The use of straight elements can also facilitate the assembly and erection processes, as the flat elements can be laid out on the ground, pre-assembled and erected afterwards. This can reduce or circumvent the use of scaffolding".*

Within the context of grid-shells, the advantages of Active-bending as a forming process can be further highlighted as follows: For grid-shells having a free-form shape, and made of 'short' straight members connected into nodes, each member will converge to the node at a different angle, which leads to non-standard

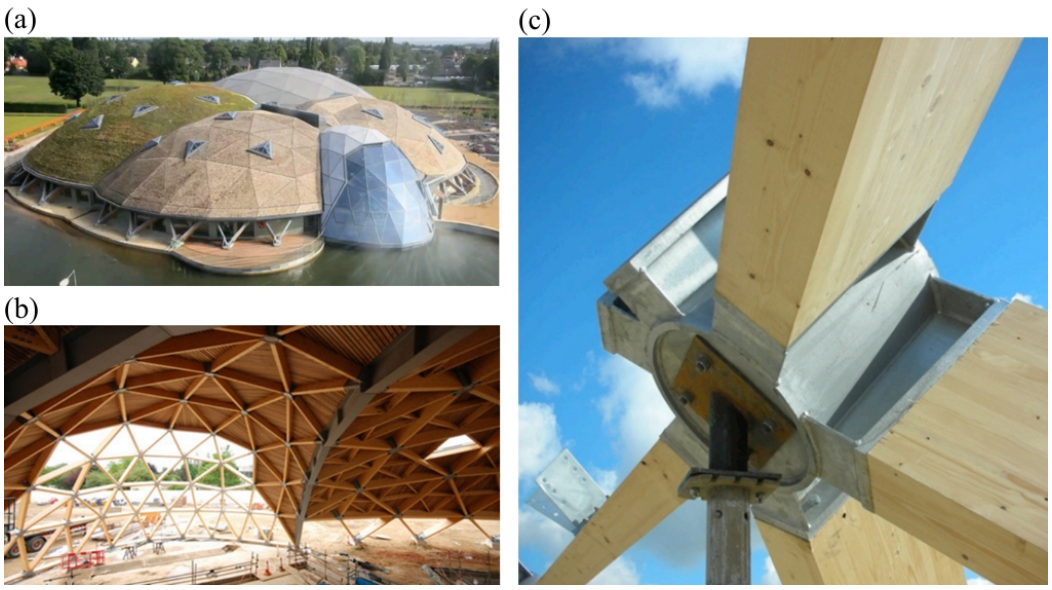


**Figure 1.7:** Grid-shell roof of The Pods sports academy [Harris et al., 2012]: (a) Aerial view; (b) Internal view; (c) Detail of the connection.

connection systems, (e.g. see Figure 1.7c) requiring Computer-Aided-Manufacturing methods to be used. Conversely: bending initially straight elastic members, such as timber planks/laths, into actual continuous curves consents to utilise 'simpler' (bolted/screwed) standard connections, as shown for instance in figure 1.8b. For timber grid-shells, made of continuous bending members, two subcategories can be defined as follow [Harris, 2011], differentiating on the geometric parameters assumed to generate a discrete grid on a surface:

If screwed laminated timber ribs are arranged following *geodesic* patterns,[3] the planks composing the rib will only be subjected to bending around the weak axis [Pirazzi et al., 2006] thus enhancing the 'allowable' width of the plank's cross-section. An example of timber grid-shell, in which such an approach was adopted,

[3]The term *geodesic* indicates in here the shortest curve, on a surface, passing for two given points.

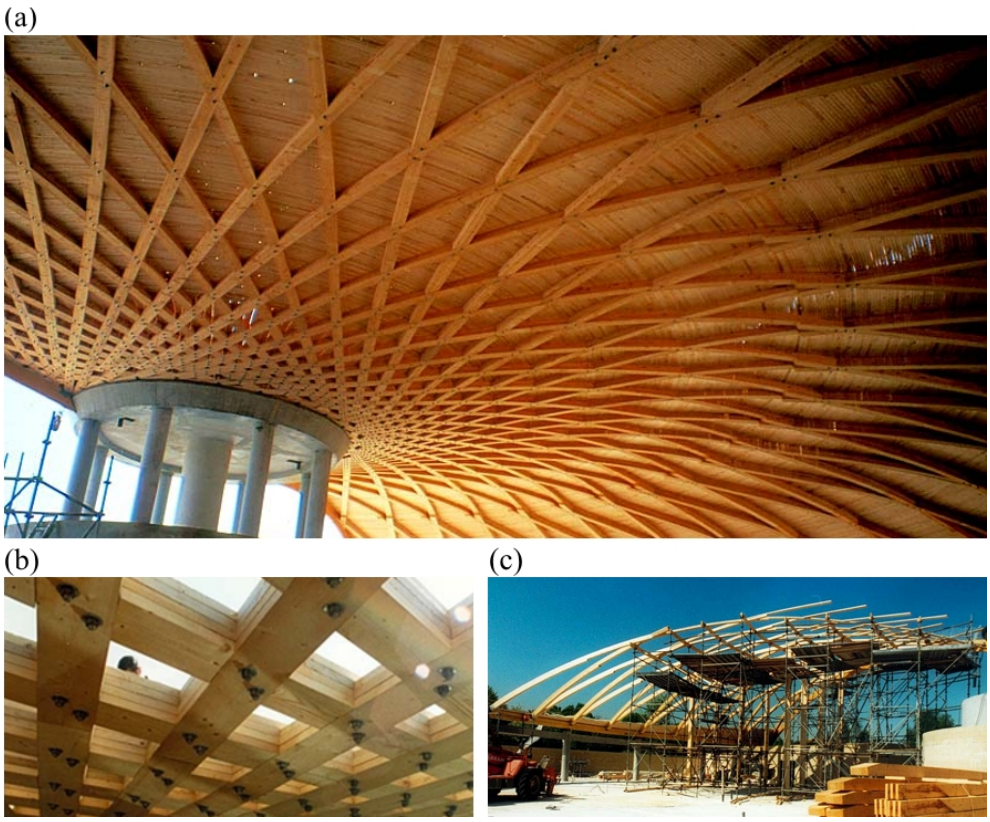


**Figure 1.8:** Geodesic rib-shell: wave pool roof in Saint-Quentin-en-Yvelines, France, 1997: (a) Internal view; (b) Connection detail; (c) Construction phase. – Structural engineer: ICS-Bois. Images source: www.cecobois.com (Accessed: 20/04/2015).

is shown in Figure 1.8. The same method was also adopted for the giant roof at the Hannover Exhibition in 2000, by Natterer et al. [2001].

A different approach was adopted instead for the design of the Mannheim timber grid-shell, for the Garden Festival [Happold and Liddell, 1975] shown in Figure 1.9. In this case, it was assumed a constant distance (50 mm) between consecutive nodes belonging to the same rib, which was built-up with two overlapping laths (double layer technique). Accordingly, the resulting geometry of the grid did not follow *geodesic* paths (hence, lateral bending occurs as well). However, this second

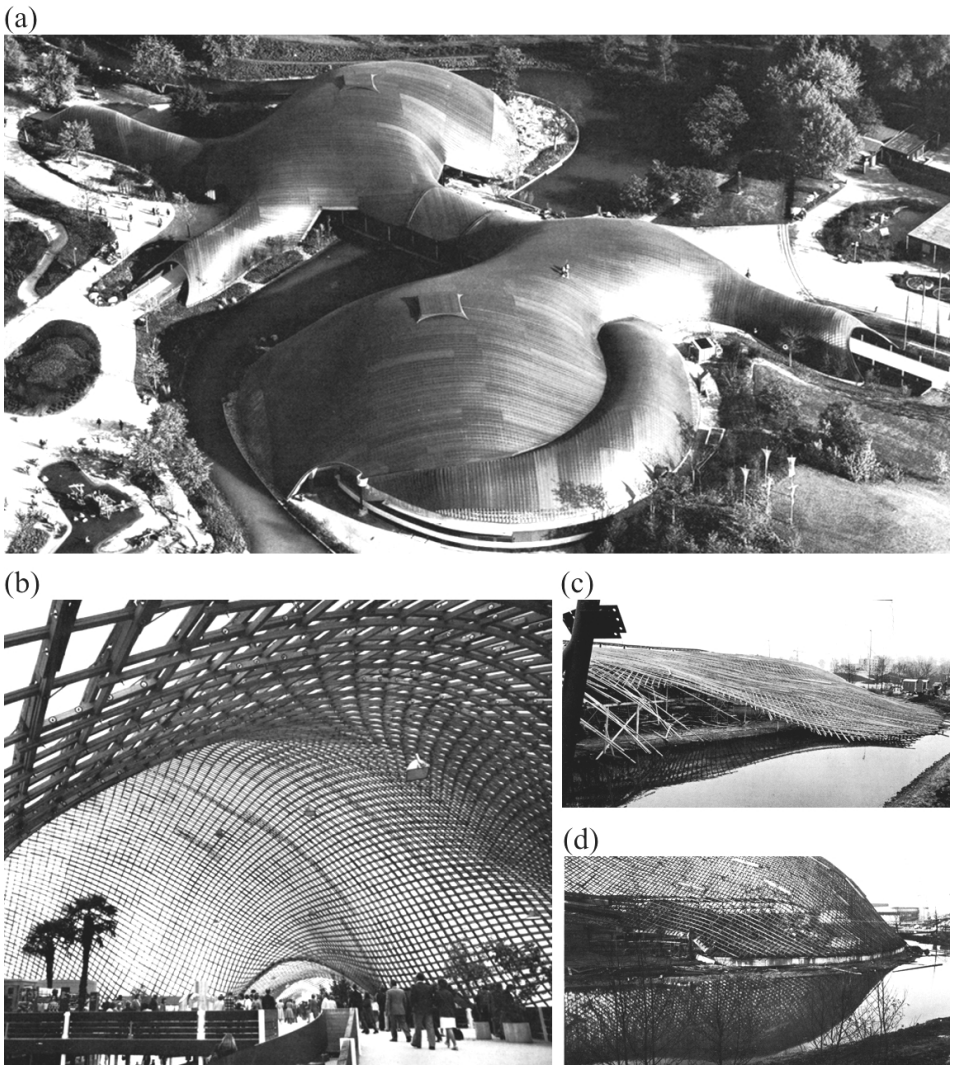


**Figure 1.9:** Mannheim Multihalle [Otto, 1978]: (a) Aerial view; (b) Internal view; (c) Initial flat mat; (d) Formed grid-shell.

design approach allowed the possibility of assembling the grid-shell laid out flat, as a two-way mat of straight continuous ribs (see Figure 1.9c) and eventually post-forming it in a doubly curved shape, by imposing external displacements, with the aid of temporary supports. With the main grid eventually formed, additional bracing elements were added to the system, in order to 'triangulate' the quadran-

**Figure 1.10:** Weald and Downland grid-shell, Singleton, Sussex, UK, 2002: Construction phases [Dickson and Harris, 2004].

gular grid pattern, thus adding in-plane shear stiffness, needed for the grid-shell to 'withstand' operating loads.

The roofs of the Weald and Downland museum (Figure 1.10) and the Savill Garden visitor centre (Figure 1.11) are major, more recent, examples of timber grid-shells bent from an initially flat mat.

### 1.2.1 Bending timber

As already mentioned, bracing members such as cables or struts, provide in-plane stiffness needed for the grid-shell to resist inextensional deformations, whilst: *"...the only way to increase the out-of-plane bending stiffness is to increase the moment of inertia of the individual members."* [Happold and Liddell, 1975]. Nonetheless, for a given elastic modulus ($E$) and bending strength ($f_m$), the increase of the cross-sectional size corresponds to a diminution of the curvature at which the bent member will break. Such an issue, justifies for instance the use of materials with high $f_m/E$ ratios, like Fibre Reinforced Polymers (e.g. NFRP, GRP, etc.) hence confining timber outside the range of 'suitable' materials for Active-bending (see for instance Figure 1.12 in regard). Remarkably, this issue was brilliantly overcame in the design of the Mannheim grid-shell by using a double-layer system

(a)

(b)

**Figure 1.11:** Savill Garden grid-shell, Surrey, UK, 2006: (a) External view; (b) Internal view. Images source: http://glennhowells.co.uk (Accessed: 23/04/2015).

of overlapping timber laths. Compared to a single-layer system with equivalent cross-sectional area, this technique allowed for tighter curvatures to be reached: the sliding between upper and lower laths was made possible during the forming (erection) process by providing slotted-holes to the outer laths (see Figure 1.13a). Then, at completion of the forming process, the sliding was restrained by inserting

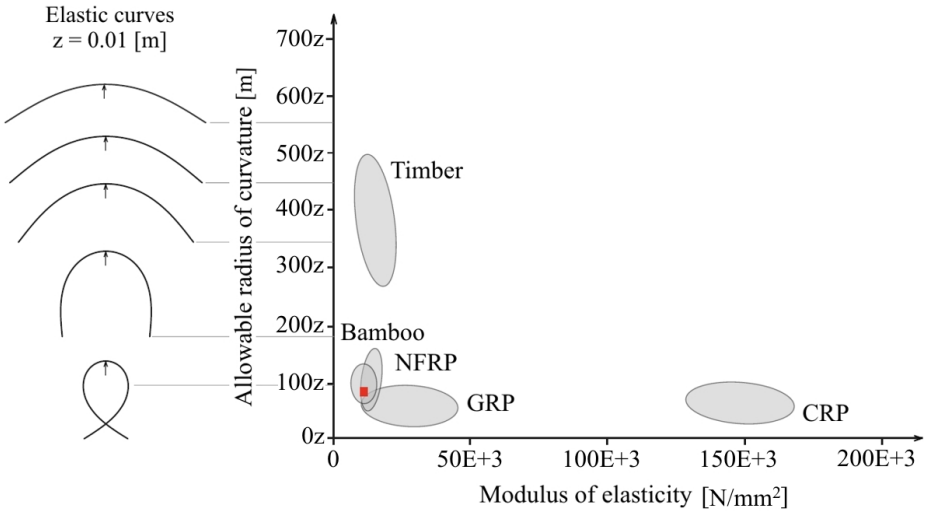


**Figure 1.12:** Material properties with respect to Active-bending. Figure adapted from: [Gengnagel et al., 2013].

shear blocks in-between the laths and tightening the connection bolts, thus greatly increasing the moment of inertia (second moment of area) of the built-up member.

The double-layer technique has been pushed forward even more in the design of the Downland grid-shell, where clamping systems, [Harris et al., 2001] as shown in Figure 1.13b, provided higher stiffness for the connections in taking horizontal shear, thus enhancing the member's bending stiffness, whereas, for the Savill Garden grid-shell, the enhancement in bending stiffness of the built-up members was achieved by increasing the thickness of the shear blocks (see Figure 1.13). This latter is a very interesting design solution, as it consents to 'separate' the coupled problem of member sizing in two distinct sub-problems, that can be solved in a sequential manner: the cross-section of the single laths can be sized by only considering the issue of 'allowable' curvatures, while the bending stiffness of the built-up member, required for the grid-shell to withstand applied loads, can be 'tuned' by solely sizing the thickness of the shear blocks. Drawback of this con-

struction method is that only one layer of the grid-shell can be assembled flat out and then post-formed, while the second one will have to be screwed on lath by lath.

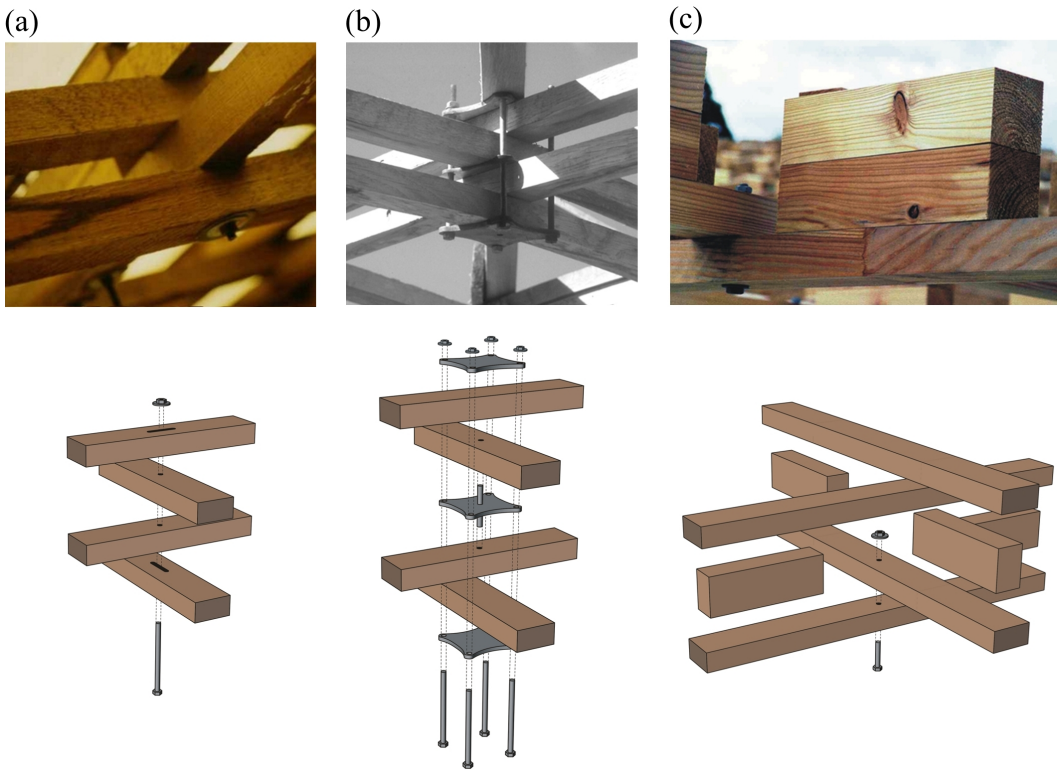


**Figure 1.13:** Double-layer technique according to the connection system: (a) Slotted-holes; (b) Clamping plate; (c) 'Thick' shear blocks.

## 1.3 Problems definition

Clearly, timber grid-shells have the potentials to create formidable architectural solutions in covering large-span open spaces, by using a minimum amount of material. Also, active-bending techniques consent realization of geometrically complex free-form shapes by means of simple, standardised, connection systems. De-

spite this, they have been rarely utilised in construction. Motivations in regard are suggested by Kelly et al. [2001] according to which: *"The reason for the apparent lack of enthusiasm may stem from the unique challenge associated with the design and formation process..."*

The main issues, concerning the design and construction of free-form (actively bent) timber grid-shells, are established in this Section by assuming three main subjects of investigation: the form-finding task, the structural analysis, and the design/optimisation of the members' cross-section.

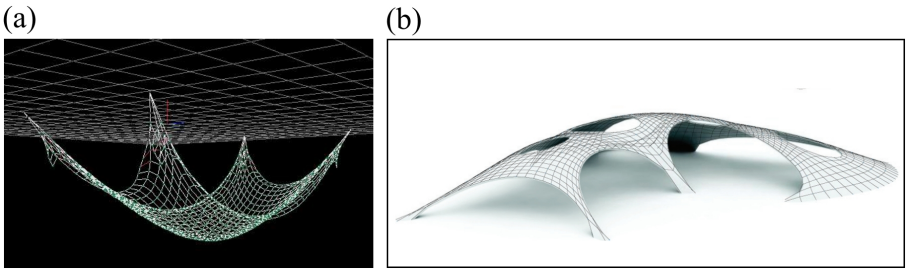


**Figure 1.14:** Numerical form-finding for the design of compression-only shells: (a) Particle Spring System, from [Kilian and Ochsendorf, 2005]; (b) Thrust Network Analysis, from [Rippmann et al., 2012].

### 1.3.1 Form-finding

Within the context of shell design, the term 'form finding' usually refers to procedures involving the use of physical [Chilton and Isler, 2000] or numerical [Kilian and Ochsendorf, 2005, Block, 2009] models in order to find optimal shapes that work in membrane (e.g. compression-only) action (see Figure 1.14). For instance, so-called *hanging models* are a typical example involved with such procedures.

These are usually made of materials working well in traction, but offering null rigidity in compression/bending, thus settling into funicular shapes if subjected to

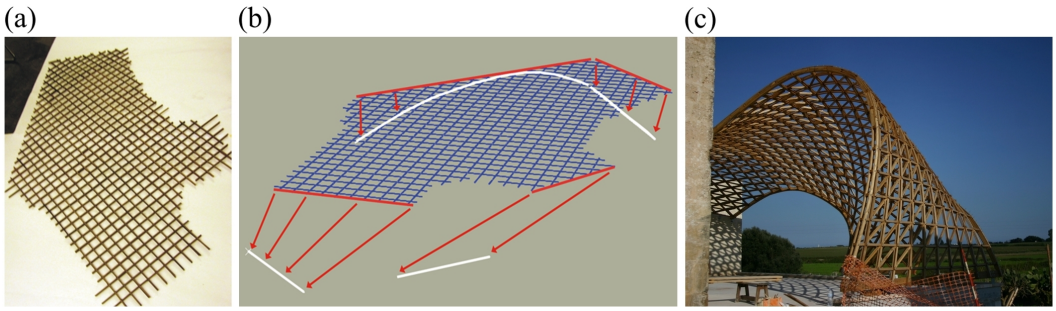


**Figure 1.15:** Trio grid-shell, Lecce, Italy, 2010 by CMMKM Architettura e Design, [D'Amico, 2010]: (a) Flat grid cutting pattern; (b) Set of imposed displacements for the form finding analysis by non-linear FE method; (c) Built structure.

gravitational loads. The shapes so found are then 'inverted' for the real structure, which indeed is then built using materials working well in compression such as concrete, bricks, stone. As underlined in Section 1.1: for lightweight (grid-shell) structures, the seeking of funicular shapes is not of primarily importance, (at least, it is not the only parameter to consider) and a form-finding procedure for grid-shell structures includes a wider range of meanings and objectives.

Further parameters to consider are related to the particular construction process of actively bent structural systems, according to which, the final shape cannot be chosen 'arbitrarily'. Rather, it has to comply with the equilibrium of external (shaping) forces and internal reactions due to material and geometric stiffnesses.

For instance, the physical models used for preliminary form finding of the Trio grid-shell (shown in Figure 1.15) were made of the same material (wood) used for the real structure, in order to include the bending stiffness effects informing the shape. On this basis, the form finding of actively bent timber grid shells can be conceived, in first instance, as a mechanical simulation of the forming (erection) process, to be carried out by either physical scale models or, more preferably, by numerical models, involving for example the use of non-linear Finite Element (FE)

procedures. In fact, this second option allows to avoid approximation errors induced e.g. by the scale factor, as well as allowing for assessment of the internal stress field, induced by the forming process itself. It has to be noted that, in order to carry out such a FE simulation of the forming process, a series of inputs are required to be known in advance. Namely:

- The initial unstressed geometry, or in other words, the *cutting pattern* of the flat mat (Figure 1.15a).
- A list of the vectors of imposed displacements, required to shape the mat according to the desired shape that we are looking for (Figure 1.15b).

According to Harris et al. [2003], for the numerical form finding of the Downland grid-shell, preliminary scale models were used to determine the displacements to impose at the mat's boundaries, whilst the flat mat, was (a priori) established to have a rectangular contour perimeter (cutting pattern).

Without doubt, a form finding procedure in which the cutting pattern of the flat mat is obtained as 'output' of the problem, (e.g. according to a desired final shape) would be preferable to a 'mere' simulation of the forming process. In facts, an approximate idea of the final, doubly curved shape, may be 'already' in mind, or it might be established according to various design requirements,[4] consequently, time and efforts will have to be spent with scale models in a trial-and-error approach, in order to find out a cutting pattern for the mat such that, once bent, it will (roughly) resemble the desired curved shape.

In light of this, and assuming to neglect the 'materiality' aspects involved in the forming process: a geometric procedure — consisting in 'mapping' a discrete

[4] According to Harris et al. [2012]: architectural and regulation parameters were driving the grid-shell shape of The Pods sports academy, (Figure 1.7) and only in a successive design phase: *"a number of trials were made to establish a grid onto a surface."*

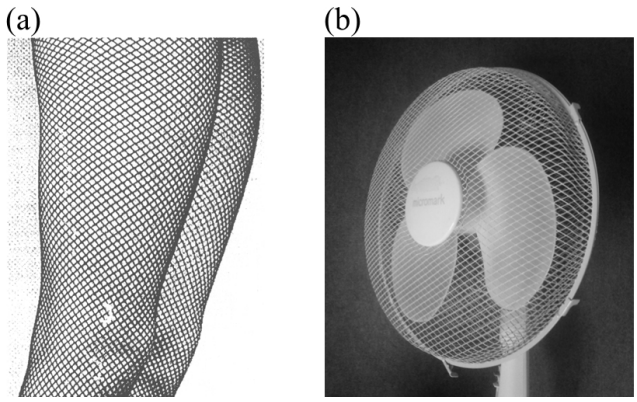


**Figure 1.16:** Real life examples of Chebyshev net: (a) Fishnet stockings [Koenderink and van Doom, 1998]; (b) Fan guard.

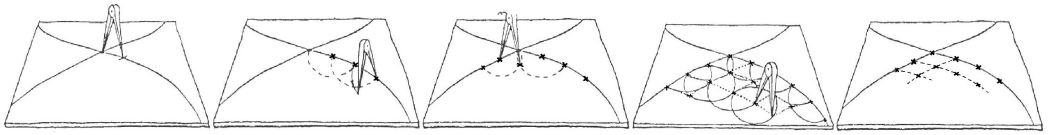

**Figure 1.17:** Compass method to map a Chebyshev net on a continuous surface [Otto et al., 1974]. The method requires the definition of two 'generating' curves intersecting each other.

grid onto a continuous surface — may be adopted as an alternative. In fact, by representing the free-form shape by a continuous surface, then a discrete geometry can be drawn directly onto it, therefore obtaining the grid-shell geometry and the cutting pattern of the corresponding flat mat.[5] Discrete 'two-way' grids with constant edge-length mapped on a continuous surface, are also known as *Chebyshev nets*,[6] (see Figure 1.16) and a practical way for their finding is the so-called *Compass method* [Otto et al., 1974]. Unfortunately, as previously mentioned, such a 'purely' geometric approach does not consider the effect of bending stiffness affecting the grid-shell shape.

[5]The flat mat and the curved mat have different geometries but same topology.

[6]From the Russian mathematician Pafnuty Chebyshev.

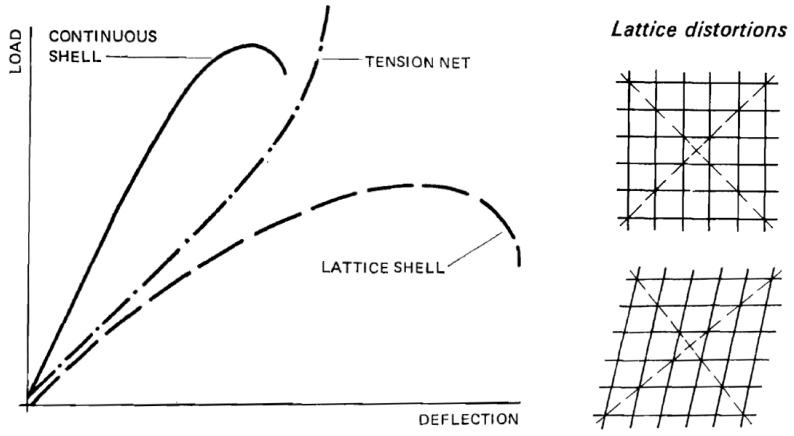


**Figure 1.18:** Qualitative comparison between the load-deflection curves of a continuous shell and a lattice shell [Happold and Liddell, 1975].

### 1.3.2 Structural analysis

Because of their shape-resistant behaviour, stability aspects are probably the most 'delicate' issue to deal with, when assessing the load-carrying capacity of shell structures. Whereas, the intrinsic stiffness of doubly-curved shapes allows for a more 'homogeneous' stress distribution — hence, for high load levels to be carried prior to reach the material's limit strength — on the other hand, the failure mode can be quite catastrophic, and ironically: *"The more efficient the shape, the more sudden the buckling collapse"* [Adriaenssens et al., 2014]. Shell buckling can occur at a local level (e.g. snap-through) globally, or as a combination of both modes [Bulenda and Knippers, 2001].

Furthermore, for grid-shell systems, an extra factor is represented by the failure of local members — in terms of (both) elastic buckling, and material's plastic-failure/rupture. Nevertheless, as noted by Happold and Liddell [1975], a two-way grid-shell results in a lower membrane (shear) stiffness (depending on the bracing' s axial stiffness) if compared to that of a continuous shell. When approaching the

buckling point, the lower stiffness leads to a larger deflection (Figure 1.18) which indeed is more favourable from a safety point of view. Because of the high sensitivity of shell structures to imperfections: 'typical' numerical methods for buckling, such as linear eigenvalue analyses, misguide to overoptimistic results. Accordingly, approaches that take geometric and material non-linearities into account are required, in order to obtain a more accurate characterisation of the structure's response.

Stability of shell structures is a fundamental research topic, finding application in many fields of engineering, from Aerospace to Construction etc., and even though, a central part of this thesis is dedicated to the implementation of a non-linear FE method — for (both) form finding and analysis — focus in here is given to the modelling and analysis of some aspects very much peculiar of actively bent timber grid-shells. In particular, the following issues will be addressed:

- Modelling of the connection system joining the structural members.
- Modelling of the connection system at the interface between shear blocks and upper/lower laths and assessment of the corresponding reactions.
- Modelling the change in bending stiffness of the structural members and assessment of the corresponding stress field during the forming process, as well as, under working loads.
- Assessment of the influence of pre-stress (due to mat's bending) on the elastic buckling load of the grid-shell.

### 1.3.3 Design and optimisation of the cross-section

As already mentioned, the double-layer technique allows tighter curvatures to be obtained compared to a single-layer mat made from rods with equivalent cross-

sectional area. Furthermore, the double-layer solution adopted for the Savill Garden grid-shell (Figure 1.13c) consents to provide shear blocks with a thickness arbitrary big, not limited to the thickness of the single laths. This may suggests to 'simplify' the coupled design problem — of sizing the cross-section of the built-up members — in two separate problems, to be solved in two consecutive design steps:

- Computing a value for the thickness of the laths (TL).
- Computing a value for the thickness of the shear blocks (TSB).

Accordingly: Total thickness of the built-up members = 2TL + TSB

For instance, if bending modulus and limit strength of timber are both set: an allowable TL value can be established during the form-finding stage according to the resulting curvature values. Then, the structure's behaviour under working loads is analysed, hence, the TSB can be established according to the bending stiffness demand of the built-up members.

## 1.4 Aims and objectives

Providing practical methods, to solve the design issues of actively bent timber grid-shells in here exposed, represents the main objective of this work. After a 'qualitative' description of the mechanics of shell structures, and an introduction to actively bent systems, three main subject of investigation have been defined, namely: Form-finding, Structural analysis and Optimisation of the member's cross-section. Methods have been developed in regard to solve these three design issues, and a detailed description of the developed methods, their application and validation, are all contents of the following Chapters (2-5).

# Part I

# Form-finding and Analysis

# Chapter 2

# Form-finding and Analysis: theory

In the Introduction it was outlined that: for the form-finding of actively bent gridshells, a mechanical simulation of the forming process implies a series of input data, which are usually obtained by preliminary scale models. On the other hand, a purely geometric approach would lack taking into account the influence of members' bending stiffness informing the grid's geometry. Let's imagine in regards, an elastic mesh constrained to lie on a given (curved) surface: it will assume a geometric configuration of minimum strain energy. Instead, a simply drawn mesh would behave like a fishnet.

## 2.1 A two-step analysis

Different authors addressed such a form-finding problem: [Bouhaya et al., 2010, Li and Knippers, 2011, Kuijvenhoven and Hoogenboom, 2012] and among these, an interesting concept that comes out is that of performing a geometrically non-linear analysis involving the use of a *reference surface* on which the elastic mat is 'forced' to bend. In general, the analysis contemplates two consecutive steps:

- An initially flat two-way mesh is bent by means of axial springs, pulling the mesh on the surface, or by means of external (gravitational) forces and contact interaction constrains. Alternatively, the mesh is positioned directly on the surface and constrained to slide on it.

- Once the equilibrium shape is found, the mesh exceeding the reference surface is 'deleted' (hence, a cutting pattern is so found) and translational Degrees of Freedom (DoF) of the boundary nodes are restrained, while the springs, forces or constrains (previously shaping the grid on the ref. surface) are disabled, hence the system will assume a new equilibrium geometry, settling down in its final configuration.

Clearly, a two-step analysis scheme allows to find the equilibrium geometry of minimum bending strain energy that closely matches a reference surface, which, acting basically as a form-work, can be modelled in accordance with a wide range of design requirements. Moreover, with such an approach there is no need for preliminary scale models since, the mat's cutting pattern and boundary displacements are obtained through the first analysis step.

## 2.2 Resolution method: Implicit or Explicit?

Established to address the form-finding task by performing the described (two-step) non-linear analysis, a suitable numerical method needs to be adopted for its implementation. For the mechanical simulation of elastic rods, and (in general) for every procedure aimed to numerically solve systems of ordinary and partial differential equations, implicit methods are preferred over explicit ones in describing the system's transient behaviour over the time domain (pseudo-time for static analyses). Implicit methods are generally preferred as they allow for larger

(a)

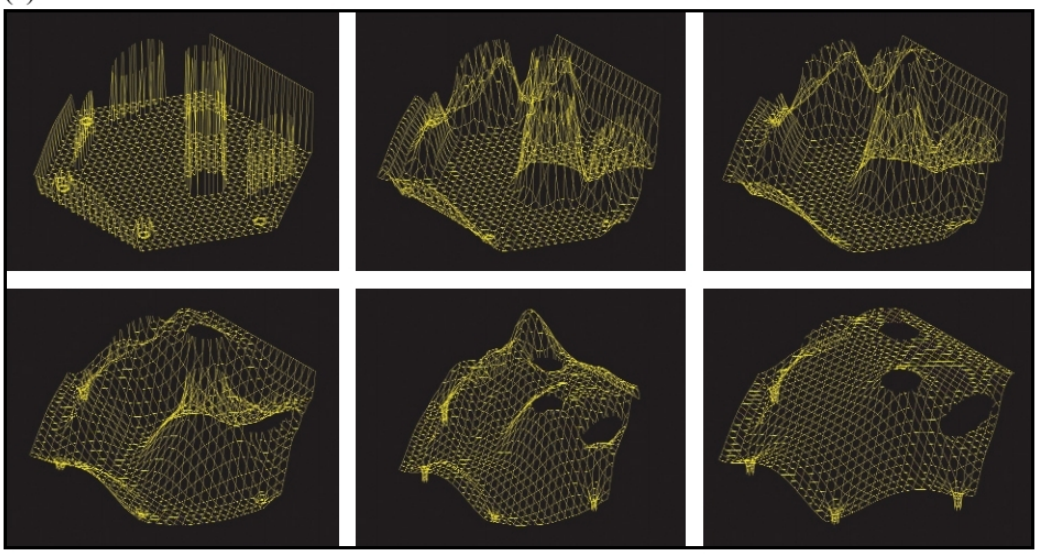

(b)

**Figure 2.1:** Centre Pompidou in Metz, France, 2010: (a) Form-finding analysis of the grid-shell roof by Dynamic Relaxation method, using Oasys GSA® (Image©: Arup, source: [Lewis, 2011]; (b) Completed construction. Image source: www.arup.com (Accessed: 09/05/2015).

(numerically stable) time increments to be considered and are insensitive to *numerical stiffness.* For instance, emblematic in this regard is the introduction by Baraff and Witkin [1998] of implicit methods to the Computer Graphics community for physically-based cloth simulation. On the other hand, explicit methods

have their own advantages, in particular: for those cases in which the given initial condition is 'very far' from equilibrium solution, explicit formulations are more advantageous, since, the root-finding algorithm (e.g. the well-known Newton-Raphson) allowing to 'implicitly' proceed over each time increment, works very well (quadratic convergence) when the integrating function is convex, whereas it is likely to fail otherwise.[1] This is a common situation when dealing with form-finding analyses, in which, the problem's unknown (namely, the structural shape) is sought by initializing the analysis with a geometry arbitrarily out-of-equilibrium (e.g. see Figure 2.1) likely to experience 'gross' deformations in converging to the equilibrium shape. Perhaps, this may explains why, an explicit method such as the Dynamic Relaxation (DR) is a standard choice in the form-finding/analysis of tension structures (see [Barnes, 1999] for instance).

## 2.3 The Dynamic Relaxation method

According to 'classic' (Stiffness Matrix) FE analysis procedures [Bathe, 2006], the continuum model, of the mechanical system under consideration, is 'converted' into an equivalent discrete system of equations as follow:

$$\mathbf{K}\boldsymbol{x} = \boldsymbol{f} \tag{2.1}$$

in which $\boldsymbol{x}$ represents the vector of nodal displacements, whilst $\mathbf{K}$ is the *global* stiffness matrix and $\boldsymbol{f}$ the vector of nodal forces (and constraints' reactions). In general, a static solution to Eq. (2.1) is pursued by operations of matrix inversion

[1] In some cases such a 'limitation' inherent to implicit methods can have useful applications, as for instance, the critical buckling load of a structure can be obtained as the load increment at which the analysis fails to converge, since at that point, the load-displacement curve becomes flat. Such a method was adopted for instance, for the structural analysis of the Mannheim Multihalle grid-shell [Happold and Liddell, 1975].

of the kind:

$$\boldsymbol{x} = \mathbf{K}^{-1}\boldsymbol{f} \tag{2.2}$$

and, in case of *small displacement* theory, a linear relation is assumed between the displacement vector and the vector of forces, hence the problem can be solved by computing the global stiffness matrix according to the initial unstressed geometry (Direct Stiffness Method). Such an assumption is obviously unacceptable in our case, therefore an iterative technique is required. The 'dominant' method in Structural Engineering for solving the system on non-linear equations (2.1) is known as the Transient Stiffness Method (TSM). As noted by Lewis [2003] the method *"...evolved from the conventional small displacements theory"* in that of keeping a linear relation between the vector of nodal forces and corresponding nodal displacements. But unlike in the small displacements theory, the vector load is applied incrementally so that, the linearised displacements are 'corrected' and the stiffness matrix 'updated' at each increment (Full Newton-Raphson) in order to minimize the residual error (vector of out-of-balance forces) occurring as a consequence of the linearisation.

A quite different approach is that of considering the problem as a 'dynamic' one, thus converting the original non-linear system of Eqs. (2.1) into a system of equations of motion:

$$\mathbf{M}\boldsymbol{a} + \mathbf{C}\boldsymbol{v} + \mathbf{K}\boldsymbol{x} = \boldsymbol{f} \tag{2.3}$$

by introduction of a matrix $\mathbf{M}$ of lumped nodal masses and a matrix $\mathbf{C}$ of viscous damping terms, required to 'force' the system converging to a rest configuration.[2] Eq. (2.3) can be expressed at time $t$ in the following form:

$$\mathbf{M}\boldsymbol{a}^t + \mathbf{C}\boldsymbol{v}^t = \mathbf{R}^t \tag{2.4}$$

[2]For a DR schemes: the Kinetic Damping method, first proposed by Cundall [1976], can be used as alternative to (or in conjunction with) viscous damping.

thus, with $\mathbf{R} = \boldsymbol{f} - \mathbf{K}\boldsymbol{x}$ representing the vector list of out-of-balance forces (residuals) as resultant of the applied loads and constraints reactions $\boldsymbol{f}$ plus members' internal reactions $\mathbf{K}\boldsymbol{x}$. In doing this, the stiffness matrix disappears and the system can be solved at a node-by-node level (this is a peculiar characteristic of the DR method) hence, the nodal displacements $\boldsymbol{x}$ are computed by explicit numerical integration of the acceleration ($\boldsymbol{a}$) and velocity ($\boldsymbol{v}$) terms.

### 2.3.1 Six Degrees of Freedom DR theory

Mostly, the DR method is implemented by only considering three DoF per node, corresponding to the translational components in the Cartesian space. Despite considering only translational DoF, DR procedures that efficiently simulate mechanical properties usually associated to rotational DoF (e.g. flexural and torsional stiffnesses) have been proposed [Adriaenssens and Barnes, 2001, Barnes et al., 2013]. In general, the theoretical assumptions, upon which these DR formulations are built, require limitations for the cross-sectional geometry or the *natural* (unstressed) geometry of the member's centreline.[3] For this reason, a generalised DR formulation (not restricted to the aforementioned limitations) with six DoF per node, is here adopted.

Developments of six DoF beam-elements and their resolution by DR scheme, were first proposed by Wakefield [1980] and Ong [1992]. In these, the orientation of the cross-section was handled by introducing a third node for each element. In more recent developments [Senatore and Piker, 2015] mainly based on the work of Williams and reported by Adriaenssens [2000]: a co-rotational formulation (see [Crisfield, 1990]) is adopted for the beam-element. Unlike *Total Lagrangian* and *Updated Lagrangian* formulations [Bathe and Bolourchi, 1979], in the co-rotational

[3] Let consider the simple case of a straight rod submitted to a torque: There is no way to simulate the torsion by only considering the nodal displacements: they remain null.

approach the motion of the element is treated as a result of a rigid motion plus a deformation. The six DoF DR scheme adopted in this work is based on this latter formulation.

### 2.3.2 Translations

Let assume an elastic rod represented by a discrete list **P** of nodal coordinates $\bar{r}_i$ with arbitrary initial position in the Cartesian space:

$$\mathbf{P} = \{\bar{r}_0 \dots \bar{r}_i \dots \bar{r}_{m^\circ}\} \quad ; \quad \bar{r}_i = [x \quad y \quad z] \tag{2.5}$$

and a connectivity list **N** storing the nodes' indexes of the element ends (1, 2):

$$\mathbf{N} = \{\mathbf{n}_0 \dots \mathbf{n}_j \dots \mathbf{n}_{n^\circ}\} \quad ; \quad \mathbf{n}_j = \{i_1, i_2\} \tag{2.6}$$

Further, for the $i$th node is associated a right-handed local frame $\{\bar{x}_i, \bar{y}_i, \bar{z}_i\}$ of unit vectors, with $\bar{z}_i$ oriented along the direction tangent to the rod's centreline, and $\bar{x}_i, \bar{y}_i$ representing the *principal* directions of the cross-section (see Figure 2.2). Note that, as for the nodes position, the initial local frame orientation can be arbitrary given. Indicating the vector list of residuals **R** in Eq (2.4) as:

$$\mathbf{R} = \left\{\bar{R}_0 \dots \bar{R}_i \dots \bar{R}_{m^\circ}\right\} \tag{2.7}$$

the out-of-balance force $\bar{R}_i$ acting at the $i$th node, as resultant of external applied loads $\bar{P}_i$ and internal reaction forces $\bar{F}_{prec.}$ and $\bar{F}_{succ.}$ of the elements preceding and succeeding the node:

$$\bar{R}_i = [R_{i,x} \quad R_{i,y} \quad R_{i,z}] = \bar{P}_i + \bar{F}_{prec.} + \bar{F}_{succ.} \tag{2.8}$$

it is used to compute the acceleration of the $i$th node at time $t$ according to Newton's second law of motion. Considering for instance the Cartesian $x$ direction only:

$$\ddot{x}_i^t = \frac{R_{i,x}^t}{m_i} \tag{2.9}$$

with $m_i$ the fictitious nodal mass. Accordingly, the updating velocity and displacement components are obtained by explicit numerical integration of the acceleration term. Using for instance a *Velocity Verlet* scheme [Tuckerman et al., 1992] the recurrence equation for the velocity term $\dot{x}_i$ at time $t$ is:

$$\dot{x}_i^t = C\dot{x}_i^{t-\Delta t} + \frac{\Delta t}{2}(\ddot{x}_i^{t-\Delta t} + \ddot{x}_i^t) \tag{2.10}$$

and the updated $x_i$ coordinate projected at time $t + \Delta t$:

$$x_i^{t+\Delta t} = x_i^t + \dot{x}_i^t \Delta t + \frac{\Delta t^2}{2}\ddot{x}_i^t \tag{2.11}$$

where $C \in [0, 1]$ is a viscous damping term. At the first analysis iteration, the velocity term $\dot{x}_i^{t-\Delta t}$ and acceleration term $\ddot{x}_i^{t-\Delta t}$ of Eq. (2.10) can be set to zero. Repeating Eqs. (2.9 to 2.11) for the remaining $y$ and $z$ components of the node, for all the node set $\mathbf{P}$, provides the updated geometry $\mathbf{P}^{t+\Delta t}$ to submit for the next DR iteration (to be run subsequently the re-positioning of constrained nodes).

The choice of an appropriate mass/time-increment ratio is of fundamental importance for DR analyses. Small lumped masses and a large time increment clearly reduce the number of iterations needed for equilibrium convergence, however, over a certain limit, numerical instability occurs. Another important parameter choice regards the value to assign for the viscous damping factor $C$, which should be proportional (for each node) to the fundamental modes of the system in order to avoid under (over) dumped vibrations, thus assuring fast equilibrium convergence. For an automatic assessment of the DR parameters see [Papadrakakis, 1981].

### 2.3.3 Rotations

Like for translations, a residual moment $\bar{H}_i$ is assumed at node $\bar{r}_i$ as the resultant of external applied moments $\bar{Q}_i$ and internal reaction moments $\bar{M}_{prec.}$ and $\bar{M}_{succ.}$

of the two elements surrounding the node:

$$\bar{H}_i = [H_{i,x} \quad H_{i,y} \quad H_{i,z}] = \bar{Q}_i + \bar{M}_{prec.} + \bar{M}_{succ.} \tag{2.12}$$

Accordingly, the angular acceleration of node $\bar{r}_i$ around the Cartesian $x$ direction at time $t$ is:

$$\ddot{\vartheta}^t_{i,x} = \frac{H^t_{i,x}}{\jmath_i} \tag{2.13}$$

where $\jmath_i$ is the fictitious lumped moment of inertia (angular mass). Therefore, the recurrence equations of angular velocity $\dot{\vartheta}_i$ at time $t$ and angle of rotation $\vartheta_i$ at time $t + \Delta t$ around the global $x$ direction are:

$$\dot{\vartheta}^t_{i,x} = C\dot{\vartheta}^{t-\Delta t}_{i,x} + \frac{\Delta t}{2}(\ddot{\vartheta}^{t-\Delta t}_{i,x} + \ddot{\vartheta}^t_{i,x}) \tag{2.14}$$

$$\vartheta^{t+\Delta t}_{i,x} = \dot{\vartheta}^t_{i,x}\Delta t + \frac{\Delta t^2}{2}\ddot{\vartheta}^t_{i,x} \tag{2.15}$$

noting that: whilst Eq. (2.11) provides an *absolute* coordinate value, the angle $\vartheta_{i,x}$ given by Eq. (2.15) is an *increment* of rotation. By applying Eqs. (2.13 to 2.15) for the Cartesian directions $y$ and $z$ too: the remaining rotational increments $\vartheta_{i,y}$ and $\vartheta_{i,z}$ can be obtained. Unlike for the translational increments, the three rotational increments (of the local frame around the Cartesian directions) so obtained, are non-commutative quantities and an appropriate way to update the orientation of the local frame $\{\bar{x}_i, \bar{y}_i, \bar{z}_i\}$ form time $t$ to time $t + \Delta t$ is that of pre-multiplying each unit vector with a rotation matrix $\mathbf{A}$ such that:

$$\bar{x}^{t+\Delta t}_i = \mathbf{A} \cdot \bar{x}^t_i \tag{2.16}$$

with $\mathbf{A}$ defined as:

$$\mathbf{A} = \mathbf{I}\cos\alpha + \mathbf{V}\sin\alpha + \mathbf{V}^2(1 - \cos\alpha) \tag{2.17}$$

where $\mathbf{I}$ is a $3 \times 3$ *Identity* matrix and $\mathbf{V}$ is a *Skew-symmetric* matrix:

$$\mathbf{V} = \begin{bmatrix} 0 & -v_z & v_y \\ v_z & 0 & -v_x \\ -v_y & v_x & 0 \end{bmatrix} \tag{2.18}$$

Eq. (2.17) is a matrix form of the *Rodrigues' rotation formula* [Rodrigues, 1815] to spatially rotate a vector ($\bar{x}_i^t$) around an axis (defined by the unit vector $\bar{v}$) by a given angle ($\alpha$). As proposed by Williams (see ref. [Adriaenssens, 2000]) the values of $\bar{v}$ and $\alpha$ can be obtained from the previously found rotational increments by using the *non-linear vector product* of Aharonov et al. [1977] (see Appendix A.1: Non-linear vector product). Assuming $\bar{x}$, $\bar{y}$ and $\bar{z}$ the unit vectors of the Cartesian space:

$$\bar{x} = [1 \quad 0 \quad 0] \quad ; \quad \bar{y} = [0 \quad 1 \quad 0] \quad ; \quad \bar{z} = [0 \quad 0 \quad 1] \tag{2.19}$$

and indicating with $\otimes$ the *non-linear vector product* operator, the rotation axis is obtained by the following expression:

$$\bar{a} = \left[\bar{x}\left(\tan\frac{\vartheta_{i,x}}{2}\right)\right] \otimes \left[\bar{y}\left(\tan\frac{\vartheta_{i,y}}{2}\right)\right] \otimes \left[\bar{z}\left(\tan\frac{\vartheta_{i,z}}{2}\right)\right] \tag{2.20}$$

with the non-zero entries of $\mathbf{V}$ and rotation angle $\alpha$ needed to apply Eq. (2.17) given by:

$$\bar{v} = \frac{\bar{a}}{|\bar{a}|} \quad ; \quad \alpha = \arctan\left(2|\bar{a}|\right) \tag{2.21}$$

Now that the rotation matrix $\mathbf{A}$ is determined, Eq. (2.16) can be applied for the remaining unit vectors $\bar{y}_i$ and $\bar{z}_i$ of the $i$th local frame as well.

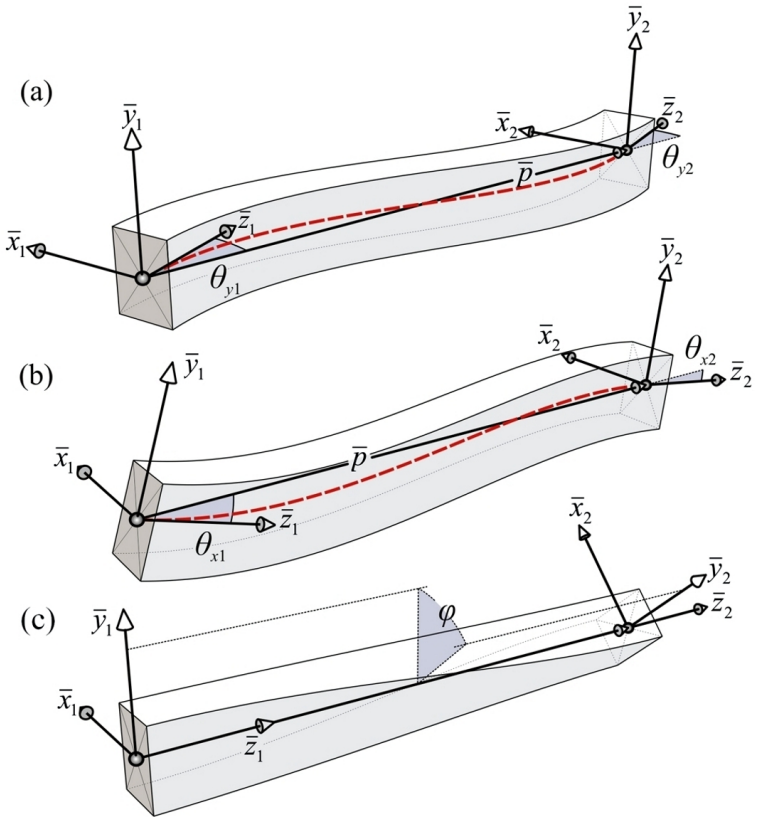


**Figure 2.2:** Co-rotational formulation: *Local displacements* for a three dimensional beam element: (a) Rotations around the local $\bar{y}$ axes; (b) Rotations around the local $\bar{x}$ axes; (c) Angle of twist.

## 2.4 Computing Residuals: co-rotational beam element

In order to implement the described time-marching scheme: the out-of-balance forces $\bar{R}_i$ and moments $\bar{H}_i$ need to be computed at each time increment. For load analyses, the system of external applied loads is (a priori) known, while it will be set to null in case of form finding analyses. Therefore, only the reaction components, in Eqs. (2.8 and 2.12) need to be computed. These vector quantities (ex-

pressed in the global coordinate system) acting on the $i$th node, can be obtained from the scalar force/moment reactions at the extremities of the elements surrounding $\bar{r}_i$. In turn, such (local) force and moment reactions are obtained from the *local displacements* of the element: With reference to Figure 2.2 the displacement's angles $\theta_{x,1}$, $\theta_{y,1}$, $\theta_{x,2}$, $\theta_{y,2}$ around the local $\bar{x}_1$, $\bar{y}_1$, $\bar{x}_2$, $\bar{y}_2$ axes; the angle of twist $\varphi$ and the axial shortening/elongation $e$, of the generic $n_j$ element, are assumed to be:

$$\theta_{x,1} = \frac{\bar{y}_1 \cdot \bar{p}}{|\bar{p}|} \quad ; \quad \theta_{y,1} = -\frac{\bar{x}_1 \cdot \bar{p}}{|\bar{p}|} \quad ; \quad \theta_{x,2} = \frac{\bar{y}_2 \cdot \bar{p}}{|\bar{p}|} \quad ; \quad \theta_{y,2} = -\frac{\bar{x}_2 \cdot \bar{p}}{|\bar{p}|} \tag{2.22}$$

$$\varphi = \frac{\bar{x}_1 \cdot \bar{y}_2 - \bar{x}_2 \cdot \bar{y}_1}{2} \tag{2.23}$$

$$e = \frac{|\bar{p}|^2 - L_0^2}{2L_0} + \frac{L_0}{60}\left[4\left(\theta_{x,1}^2 + \theta_{y,1}^2\right) - 2\left(\theta_{x,1}\theta_{x,2} - \theta_{y,1}\theta_{y,2}\right) + 4\left(\theta_{x,2}^2 + \theta_{y,2}^2\right)\right] \tag{2.24}$$

with $\bar{p} = \bar{r}_{i_2} - \bar{r}_{i_1}$ the vector connecting the beam end-nodes at time $t$ and $L_0$ the unstressed length of the element (which may not correspond to the initial length). From Eqs. (2.22) it can be noticed that the local displacements for the beam-element are based upon *large-displacements; small-strains* theory, hence by making assumptions of the kind: $cos(angle) \approx angle$. Noting also that, because of the chosen reference frame (at a node level instead of element level) expressions for the local shear displacements are not explicitly set out.

Differentiating the beam's expression of total strain energy $U$ with respect to the given local displacements, and indicating with $A$, $I_x$, $I_y$, $J$, $E$ and $G$ respectively: Cross sectional area, moments of area, torsional constant, Young's and shear moduli, the resulting element ends reactions are:

$$N = \frac{EA}{L_0}e \quad ; \quad M_\varphi = \frac{GJ}{L_0}\varphi \tag{2.25}$$

$$M_{x,1} = \frac{NL_0}{30}(4\theta_{x,1} - \theta_{x,2}) + \frac{2EI_x}{L_0}(2\theta_{x,1} + \theta_{x,2}) \tag{2.26}$$

$$M_{x,2} = \frac{NL_0}{30}(4\theta_{x,2} - \theta_{x,1}) + \frac{2EI_x}{L_0}(2\theta_{x,2} + \theta_{x,1}) \tag{2.27}$$

$$M_{y,1} = \frac{NL_0}{30}(4\theta_{y,1} - \theta_{y,2}) + \frac{2EI_y}{L_0}(2\theta_{y,1} + \theta_{y,2}) \tag{2.28}$$

$$M_{y,2} = \frac{NL_0}{30}(4\theta_{y,2} - \theta_{y,1}) + \frac{2EI_y}{L_0}(2\theta_{y,2} + \theta_{y,1}) \tag{2.29}$$

where $N$ is the internal axial force, $M_\varphi$ the torsion moment around $\bar{p}$ and $M_{x,1}$, $M_{x,2}$, $M_{y,1}$, $M_{y,2}$ the bending moments about the $\bar{x}_1$, $\bar{x}_2$, $\bar{y}_1$, $\bar{y}_2$ local axes.

For a derivation of Eqs. (2.22 to 2.29) the reader is referred to [Adriaenssens, 2000]. However, it is worth in here to note that the coupling between translations and rotations has been taken into account: In Eq. (2.24) the total shortening/elongation ($e$) is obtained as summation of the element's axial displacement plus the contribution caused by element bowing (the first and second terms of the expression, respectively). This leads to the appearance of the axial force term $N$ in Eqs. (2.26 to 2.29) taking into account the amount of moment generated by an axial force acting on a bent member. The local force-displacement relations for the *j*th element (Eqs. 2.25 to 2.29) may be written in matrix form:

$$\mathbf{f} = \{\mathbf{K}_A^t + \mathbf{K}_B\} \cdot \mathbf{d} \tag{2.30}$$

where:

$$\mathbf{f} = \begin{bmatrix} N \\ M_{x,1} \\ M_{x,2} \\ M_{y,1} \\ M_{y,2} \\ M_{\varphi} \end{bmatrix} \quad ; \quad \mathbf{d} = \begin{bmatrix} 1 \\ \theta_{x,1} \\ \theta_{x,2} \\ \theta_{y,1} \\ \theta_{y,2} \\ \varphi \end{bmatrix} \tag{2.31}$$

$$\mathbf{K}_A^t = EAe \begin{bmatrix} 1/L_0 & 0 & 0 & 0 & 0 & 0 \\ & 2/15 & -1/30 & 0 & 0 & 0 \\ & & 2/15 & 0 & 0 & 0 \\ & & & 2/15 & -1/30 & 0 \\ & & & & 2/15 & 0 \\ \text{Symmetric} & & & & & 0 \end{bmatrix} \tag{2.32}$$

$$\mathbf{K}_B = \frac{1}{L_0} \begin{bmatrix} 0 & 0 & 0 & 0 & 0 & 0 \\ & 4EI_x & 2EI_x & 0 & 0 & 0 \\ & & 4EI_x & 0 & 0 & 0 \\ & & & 4EI_y & 2EI_y & 0 \\ & & & & 4EI_y & 0 \\ \text{Symmetric} & & & & & GJ \end{bmatrix} \tag{2.33}$$

As it can be seen, the stiffness matrix $\mathbf{K}_B$ only depends on the material properties and unstressed beam geometry, while $\mathbf{K}_A$ takes into account, at each time increment, the stiffness contribution due to element's shortening/elongation and bowing ($e$).

The nodal vector forces $\bar{F}_1$, $\bar{F}_2$ and moments $\bar{M}_1$, $\bar{M}_2$ generated by the above scalar quantities, and needed to computing the residuals $\bar{R}_i$ and $\bar{H}_i$ (see Eqs. (2.8

and 2.12)) are so obtained:

$$\bar{F}_1 = \frac{N}{|\bar{p}|}\bar{p} + \bar{T} \quad ; \quad \bar{F}_2 = -\bar{F}_1 \tag{2.34}$$

$$\bar{M}_1 = \bar{x}_1 M_{x,1} + \bar{y}_1 M_{y,1} + \bar{z}_1 M_\varphi \tag{2.35}$$

$$\bar{M}_2 = \bar{x}_2 M_{x,2} + \bar{y}_2 M_{y,2} - \bar{z}_2 M_\varphi \tag{2.36}$$

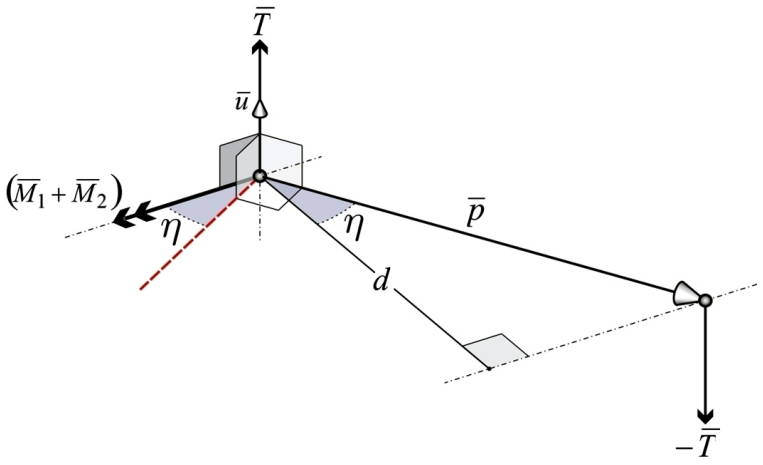


**Figure 2.3:** Shear reaction force $\bar{T}$ at the element's end nodes.

The free-body shear force $\bar{T}$ in Eq. (2.34), which was missing at a local reference frame level, can be found by imposing the equilibrium to rotation of the element: The resultant moment $\bar{M}_1 + \bar{M}_2$ acting on the element, will generates a shear force oriented in the $\bar{u}$ direction orthogonal to both $\bar{p}$ and $\bar{M}_1 + \bar{M}_2$ itself, as shown in Figure 2.3. Accordingly:

$$\bar{u} = \frac{(\bar{M}_1 + \bar{M}_2) \times \bar{p}}{|(\bar{M}_1 + \bar{M}_2) \times \bar{p}|} \tag{2.37}$$

The scaling value $|\bar{T}|$ of $\bar{u}$ to obtain $\bar{T}$ is given by the torque lever-arm relation:

$$|\bar{T}| = \frac{|\bar{M}_1 + \bar{M}_2|}{d} \quad ; \quad d = |\bar{p}| \cdot \cos\eta \tag{2.38}$$

where $\cos\eta$ can be found by dot product between $\bar{M}_1 + \bar{M}_2$ and a vector lying on the dashed line shown in Figure 2.3, orthogonal to both $\bar{p}$ and $\bar{u}$:

$$\cos\eta = \frac{(\bar{M}_1 + \bar{M}_2) \cdot (\bar{p} \times \bar{u})}{|\bar{M}_1 + \bar{M}_2||\bar{p} \times \bar{u}|} \tag{2.39}$$

Rearranging Eqs. (2.38 and 2.39) gives the following expression for shear force:

$$\bar{T} = \bar{u}\frac{|\bar{M}_1 + \bar{M}_2|^2|\bar{p} \times \bar{u}|}{|\bar{p}|\left[(\bar{M}_1 + \bar{M}_2) \cdot (\bar{p} \times \bar{u})\right]} \tag{2.40}$$

## 2.5 Application to grid-shells: constraints

With the described co-rotational beam-element formulation, and its resolution by DR method, we are now able to simulate the mechanical behaviour of elastic members. For the form-finding and analysis of actively bent timber grid-shells, coupling constraints (joining the members into a grid framework) and global constraints (forcing the grid onto the surface) need to be taken into account.

### 2.5.1 Cylindrical hinge-joints

For any of the connection systems previously discussed in the Introduction (see Figure 1.13), a 'hinge' mechanism occurs at the nodal connections of the two-way mat. In general, such hinge-like connections are numerically modelled by placing the beam-elements (representing the members of the mat) on two staggered levels and connecting them by means of *link* elements which allow rotation around their longitudinal axis (see Figure 2.4b). Although faithful to the real geometry, doubling the nodes at each connection generates local eccentricities.

On the contrary, a 'simpler' model with only one node per connection (Figure 2.4c) it is numerically more stable. Such single-node model can be implemented by assuming a double connectivity list (**N**; **M** for instance) thus having two separate

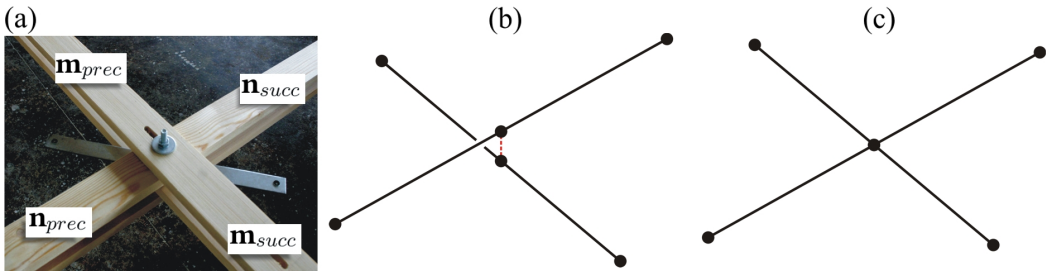


**Figure 2.4:** Connection system: (a) Two distinct **N** and **M** connectivity lists are used to define the equivalent numerical model; (b) Numerical model with *link* elements; (c) Numerical model by using one node only per connection.

lists, one for each direction of the two-way mat (see Figure 2.4a):

$$\mathbf{M} = \{\mathbf{m}_0 \dots \mathbf{m}_k \dots \mathbf{m}_{n^\circ}\} \quad ; \quad \mathbf{m}_k = \{i_1, i_2\} \tag{2.41}$$

and a second local coordinate system such that each connection is defined by a single position vector $\bar{r}_i$ but two local systems:

$$\{\bar{x}_{i,n}, \bar{y}_{i,n}, \bar{z}_{i,n}\} \quad ; \quad \{\bar{x}_{i,m}, \bar{y}_{i,m}, \bar{z}_{i,m}\} \tag{2.42}$$

Accordingly: the residual out-of-balance force $\bar{R}_i$ is obtained as the resultant of reactions of the four elements surrounding $\bar{r}_i$:

$$\bar{R}_i = \bar{P}_i + \bar{F}_{prec,n} + \bar{F}_{succ,n} + \bar{F}_{prec,m} + \bar{F}_{succ,m} \tag{2.43}$$

whilst the rotational DoFs can be nodally decoupled by computing two distinct out-of-balance moments:

$$\bar{H}_{i,n} = \bar{Q}_{i,n} + \bar{M}_{prec,n} + \bar{M}_{succ,n} \quad ; \quad \bar{H}_{i,m} = \bar{Q}_{i,m} + \bar{M}_{prec,m} + \bar{M}_{succ,m} \tag{2.44}$$

The resulting kinematic mechanism of the described model resembles a spherical joint acting between two rods ($n$ and $m$). In order to simulate a (more suitable) cylindrical joint, with $\bar{y}_{i,n} \equiv \bar{y}_{i,m}$ coincident with the joint rotational axis, the resulting angle $\beta$ between $\bar{y}_{i,n}$ and $\bar{y}_{i,m}$ at the end of the DR iteration, has to be reset

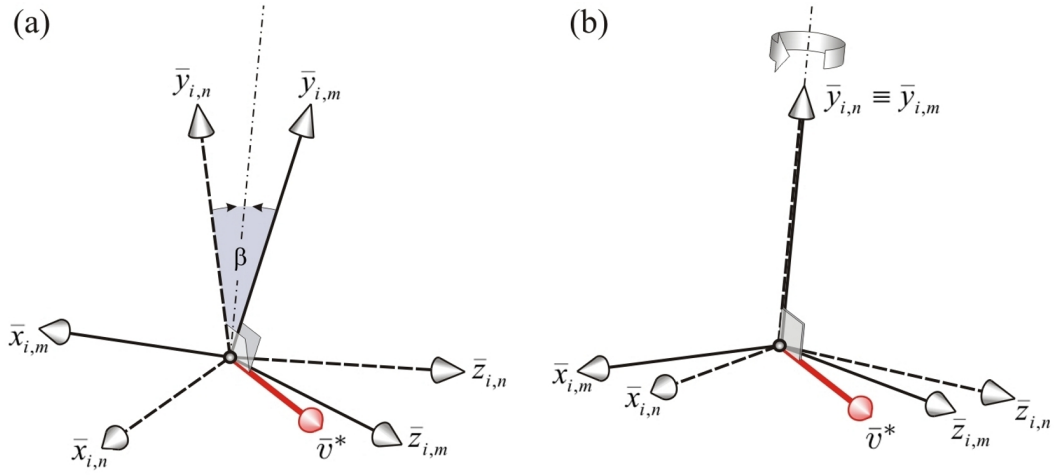


**Figure 2.5:** Local coordinate systems of the surrounding $n$ and $m$ elements at node $i$: (a) Spherical hinge. The rotations of the two systems are decoupled; (b) Cylindrical joint. The $\bar{y}_{i,n}$ and $\bar{y}_{i,m}$ local axes are constrained along the same direction.

to zero (see Figure 2.5). This task is performed by pre multiplying once more the local system orientations resulting from Eq. (2.16) with a rotation matrix (Eq. 2.17) whose entries this time are given by:

$$\bar{v}^* = \frac{\bar{y}_{i,m} \times \bar{y}_{i,n}}{|\bar{y}_{i,m} \times \bar{y}_{i,n}|} \quad ; \quad \alpha_n = \beta/2 \quad ; \quad \alpha_m = -\beta/2 \tag{2.45}$$

where: $\alpha_n$ applies in Eq. (2.16) to rotate $\{\bar{x}_{i,n}, \bar{y}_{i,n}, \bar{z}_{i,n}\}$ and $\alpha_m$ applies to rotate $\{\bar{x}_{i,m}, \bar{y}_{i,m}, \bar{z}_{i,m}\}$. Of course, the local system orientations found by using Eqs. (2.45) do not correspond to an equilibrium configuration, as well as the nodes position at the current time anyway. Since we are only interested in the (final) static equilibrium configuration, the out of balance moment generated by the described 'artificial' rotation will gradually decrease with the residuals, eventually becoming small enough to be neglected (at analysis completion). Moreover, the described procedure allows semi-rigid behaviour to be simulated as well (e.g to take into account the connection stiffness) by scaling, at every time increment, the resulting $\alpha_n$ and $\alpha_m$ angles with a reducing factor $s \in [0, 1]$. Accordingly:

- For $s = 1 \Rightarrow$ a cylindrical-hinge joint is obtained.
- For $s = 0 \Rightarrow$ a spherical-hinge mechanism occurs.

### 2.5.2 Surface constraints

Provided an appropriate mass/time-increment ratio, the DR methods will always converge to an equilibrium configuration of minimum strain energy (which is typical of explicit numerical schemes such as DR) no matter how gross is the deformation of the initial grid on the reference surface. Nonetheless, a mere random distribution of the initial nodes' position may results in a grid which will 'fold back' on itself on the reference surface at analysis completion. A simple measure to prevent the analysis converging to such an equilibrium configuration of 'local' minimum strain energy, is assuring a 'certain' degree of geometric regularity for the initial grid pattern, which for instance, may be generated by projection maps (e.g. Cartesian, gnomonic, cylindrical, spherical, etc.) from a matrix of point.

Clearly, fundamental requirement for the initial position of the grid nodes is obviously that they have to lie on the reference surface. Assuming the reference surface described by a *real* function of the kind $f(\bar{r}) = 0$ with $\bar{r}$ a coordinate vector defined in $\mathbb{R}^3$:

$$\mathbf{P} = \{\bar{r} \mid f(\bar{r}) = 0\} \tag{2.46}$$

In addition, we have to define a subspace of interest, of the Cartesian space, containing the part of mesh (a subset of the node list **P**) that we want constrained to slide on the surface. Indicating with $\mathbf{B} \subset \mathbb{R}^3$ the subspace of interest, in case the *i*th node falls into **B** ($\bar{r}_i \in \mathbf{B}$) then, only the tangent-to-surface component ($\bar{R}_{i\|}$) of the out-of-balance force ($\bar{R}_i$) is considered:

$$\bar{R}_{i\|} = \bar{w}_i \times (\bar{R}_i \times \bar{w}_i) \tag{2.47}$$

On the opposite, for $\bar{r}_i \notin \mathbf{B}$, the full residual obtained by Eq. (2.43) is inserted in Eq. (2.9) to eventually obtain the updated node position. The unit vector normal to the surface $\bar{w}_i$ appearing in Eq. (2.47) is given by [Williams, 2011]:

$$\bar{w}_i = \frac{\dfrac{\partial f}{\partial x}\bar{x} + \dfrac{\partial f}{\partial y}\bar{y} + \dfrac{\partial f}{\partial z}\bar{z}}{\sqrt{\left(\dfrac{\partial f}{\partial x}\right)^2 + \left(\dfrac{\partial f}{\partial y}\right)^2 + \left(\dfrac{\partial f}{\partial z}\right)^2}} \tag{2.48}$$

with $x$, $y$ and $z$ the components of $\bar{r}_i$, while $\bar{x}$, $\bar{y}$ and $\bar{z}$ are the unit vectors of the Cartesian space (see Eqs. (2.19)) not to be confused with the local frame unit vectors $\{\bar{x}_i, \bar{y}_i, \bar{z}_i\}$. Even though, we constrained certain nodes of the mesh to move along the tangent-to-surface direction, their updated node position (given by Eqs. 2.11) will almost surely be off the surface (meaning that $f(\bar{r}_i) \neq 0$). Therefore, prior running the next DR iteration, those nodes have to be pulled back on the surface. The closest coordinate position on the surface ($\bar{r}_i^*$) of the $\bar{r}_i$ node is given by [Williams, 2011]:

$$\bar{r}_i^* = \bar{r}_i - \frac{f(\bar{r}_i)\left[\dfrac{\partial f}{\partial x}\bar{x} + \dfrac{\partial f}{\partial y}\bar{y} + \dfrac{\partial f}{\partial z}\bar{z}\right]}{\left(\dfrac{\partial f}{\partial x}\right)^2 + \left(\dfrac{\partial f}{\partial y}\right)^2 + \left(\dfrac{\partial f}{\partial z}\right)^2} \tag{2.49}$$

As alternative to the computing of tangential residuals and node repositioning (Eqs. 2.47 to 2.49) an external 'pulling' force $k(\bar{r}_i^* - \bar{r}_i)$ can be added in Eq. (2.43) to constrain the elastic grid moving close to the reference surface but allowing some clearance as well, e.g. in order to reduce the resulting bending stress. Such pulling force can be conceived as the effect of an axial spring linking each grid node $\bar{r}_i$ to the surface in $\bar{r}_i^*$. The spring stiffness $k$ is calibrated to reduce/increase the clearance amplitude. Noting that: by re-computing the surface node position $\bar{r}_i^*$ at every time increment as the closest to $\bar{r}_i$, the corresponding spring force will not induce any undesirable axial stress to the elastic grid during the forming

simulation. Of course, a value of $k$ varying for each node may be provided as well, in order to (smoothly) reduce the clearance in some areas, as for example, at the surface boundary.

## 2.6 A mesh-cutting algorithm

By implementing the theory described earlier in this Chapter (form Section 2.3.2 to 2.5.2) we can now perform the first analysis step of the form-finding procedure under description, or in other words, we can force an elastic two-way grid with constant edge-length to 'relax' on a given reference surface, by starting the analysis with an arbitrary geometry. Once the elastic grid, constrained to the surface, reaches a static equilibrium configuration, at completion of the first DR analysis step, the grid geometry is initialized (thus submitted to the second analysis step) by 'cutting' the excess part. This task is performed by interrogating the connectivity lists **N** and **M** checking for each element, whether the corresponding end nodes fall into the subspace **B**, thus the connectivity lists are updated accordingly, discharging all the elements outside **B**. However, if an element crosses the subspace of interest, manipulation of the geometry list **P** is required. In other terms, we need to find the nodal coordinates $\bar{r}_0$ at the point of intersection between the boundary of **B** and the element's shape function: Let assume that **B** is lower bounded by $z \geq 0$ and $\bar{r}(t)$ is the iso-parametric (*Hermite*) shape function of the crossing element, defined by the end nodes ($\bar{r}_{i_1}$; $\bar{r}_{i_2}$), tangent unit vectors ($\bar{z}_1$; $\bar{z}_2$), as shown in Figure 2.2, and a parameter $t \in [0, 1]$:

$$\bar{r}(t=0) = \bar{r}_{i_1} \quad ; \quad \bar{r}(t=1) = \bar{r}_{i_2} \tag{2.50}$$

The problem is reduced to find the value of $t_0$ for $t$ such that $\bar{r}(t_0)$ lies on the

global $(x, y)$ plane:

$$t_0 \rightarrow \bar{r}(t_0) = [x \quad y \quad 0] \quad ; \quad t_0 \in [0, 1] \tag{2.51}$$

hence we take into account only the third component of $\bar{r}$ in Eq. (2.51):

$$t_0 \rightarrow z(t_0) = 0 \tag{2.52}$$

A solution of the cubic function (2.52) may be pursued analytically (e.g by Cardano's method or Vieta's substitution). Alternatively, an iterative method such us Newton's method can be used:

$$t^{\mathrm{n}+1} = t^{\mathrm{n}} - \frac{z(t^{\mathrm{n}})}{\left(\dfrac{\partial z}{\partial t^{\mathrm{n}}}\right)} \tag{2.53}$$

The value of $t_0$ so found is then inserted in the remaining two $x(t)$ and $y(t)$ of $\bar{r}(t)$ thus obtaining $\bar{r}_0$. Extending the problem to the general case of **B** bounded by a plane with arbitrary orientation, Eq. (2.52) becomes:

$$t_0 \rightarrow \bar{\omega}_p \cdot [\bar{r}(t_0) - \bar{r}_p] = 0 \tag{2.54}$$

with $\bar{\omega}_p$ the vector normal to the plane and $\bar{r}_p$ a point of the plane. Therefore, the recurrence Eq. (2.53) becomes:

$$t^{\mathrm{n}+1} = t^{\mathrm{n}} - \frac{\bar{\omega}_p \cdot [\bar{r}(t^{\mathrm{n}}) - \bar{r}_p]}{\bar{\omega}_p \cdot \left(\dfrac{\partial \bar{r}}{\partial t^{\mathrm{n}}}\right)} \tag{2.55}$$

The new boundary node so found is added to the node list **P** and the connectivity index of the crossing element is updated accordingly.

A description of the algorithm is given with reference to Figure 2.6: The element *'12'* crosses the subspace of interest **B** with its *start* node 4, thus the new node 8 is computed and the element's connectivity is updated, while, element *'19'*

remains connected to node 4 (see Figure 2.6b). By adding a new node to the **P** list, rather updating the coordinate values of the former (start/end) node, there is no need for following any particular (geometric/spatial) order in inspecting the connectivity list, thus allowing parallel access and computing schemes.

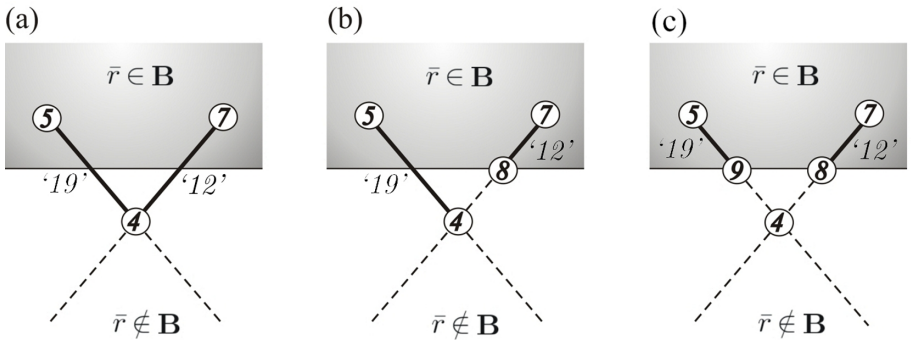


**Figure 2.6:** Cutting algorithm: (a) Two elements crossing the subspace **B** are connected to the same node 4; (b) At the 12th iteration the *end* node of element *'12'* is updated, while element *'19'* remains linked to node 4; (c) The boundary node 9 can be (independently) computed at the 19th iteration.

## 2.7 Modelling double-layer systems

As already explained, the double layer technique allows tighter curvatures to be obtained compared to a single layer mat made of laths with equivalent cross-sectional area. Once the forming process is complete, sliding between overlapping laths is constrained (thus, enhancing the bending stiffness of the built-up rib) by inserting timber shear blocks in between the laths making up the single rib. Accordingly, in order to perform load analyses continuously during the form-finding design task, the change in bending stiffness due to the presence of shear blocks needs somehow to be taken into account.

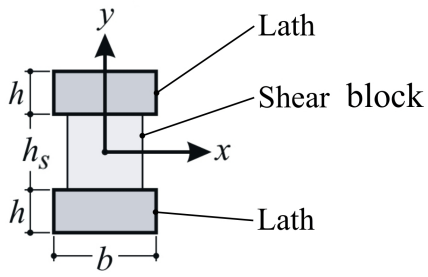


**Figure 2.7:** Built-up cross-section.

### 2.7.1 Equivalent bending stiffness

For a built-up member subject to bending due to external loads, the slip between overlapped laths leads to a discontinuity of strains at the interface, resulting in a difference in curvature of the individual laths. Consequently, a 'correct' numerical model should consider a single element for each overlapping lath in order to fully model the mechanical behaviour of the composite member. *"An alternative, slightly less accurate method..."* [Porteous and Kermani, 2013] assumes compatibility in the displacements and curvatures at the interface of overlapped laths, by considering the fasteners of the shear block connections as a series of linear springs having shear stiffness ($K$), therefore modelling the built-up member as a single element, having an 'equivalent' $EI$ value, as a function of the shear stiffness of the spring.

Since during the forming process, sliding between overlapping laths is allowed, the values of cross-sectional area and second moment of area, to use for the co-rotational beam-element previously described, are twice that of the corresponding single lath value (see Figure 2.7):

$$I_x^* = bh^3/6 \tag{2.56}$$

Then, for a load analysis, the increase of bending stiffness due to presence of shear blocks needs to be taken into account. Assuming an infinitely rigid connection between laths and shear blocks (absence of slip at the interfaces), the resulting

second moment of area around the local $\bar{x}$ axis is:

$$I_x^{**} = \frac{b(2h + h_s)^3}{12} - \frac{bh_s^3}{12} \tag{2.57}$$

On the other hand, assuming the contribution to stiffness given by shear blocks as null, the resulting second moment of area is obviously that given by Eq. (2.56). Therefore, by considering that:

$$\begin{aligned} I_x^{**} &= \frac{b(2h + h_s)^3}{12} - \frac{bh_s^3}{12} = \\ &= \frac{b}{6}(4h^3 + 6h^2 h_s + 3hh_s^2) = \\ &= \frac{4}{6}bh^3 + \frac{b}{6}(6h^2 h_s + 3hh_s^2) = \\ &= \frac{1}{6}bh^3 + \frac{3}{6}bh^3 + \frac{b}{6}(6h^2 h_s + 3hh_s^2) = \\ &= \frac{bh^3}{6} + \left(\frac{h^2}{2} + \frac{h_s^2}{2} + hh_s\right) bh \end{aligned} \tag{2.58}$$

a general equation can be arranged:

$$I_x = c_s \frac{(h + h_s)^2}{2} bh + \frac{bh^3}{6} \quad ; \quad c_s \in [0, 1] \tag{2.59}$$

where, $c_s$ is set to zero to simulate the forming process, while a value $> 0$ is set for load analyses, in order to take into account the increase in bending stiffness due to the presence of shear blocks. The *connection efficiency factor* $c_s$ of Eq. (2.59) will be a function of the elastic modulus, cross-sectional area ($A = bh$), rod's length ($L$), stiffness ($K$) of the springs in taking horizontal shear, and springs (fastener) spacing ($s$):

$$c_s = f(E, b, h, L, K, s) \tag{2.60}$$

Where: for $K \approx \infty$ (e.g. glued connection) then $c_s = 1$ while, for $K = 0$ (e.g. no shear blocks) $\Rightarrow c_s = 0$.

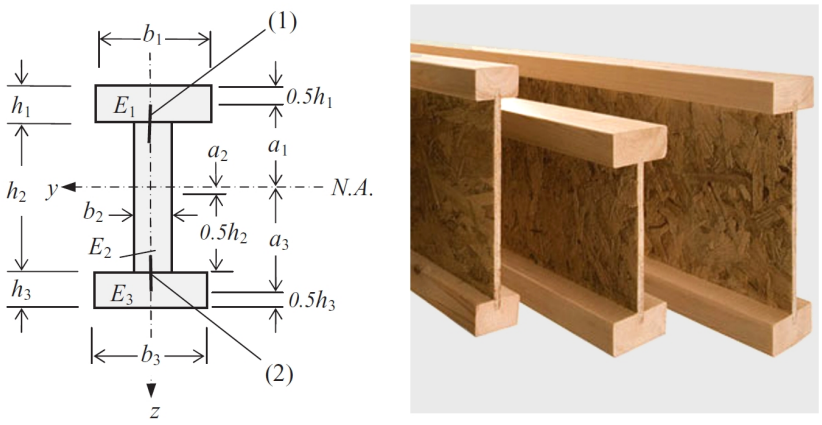


**Figure 2.8:** Timber I-beam.

Interesting to note that Equation B.1 in Annex B of Eurocode5 [2008] (EC5):

$$(EI)_{ef} = \sum_{i=1}^{3}(E_i I_i + \gamma_i E_i A_i a_i^2) \tag{2.61}$$

provides a way to calculate the *effective* (equivalent) bending stiffness $(EI)_{ef}$ of built-up sections, such as the timber I-beam shown in Figure 2.8. By setting $E_i$, $I_i$ and $A_i$ in such Equation according to our cross-section geometry (see Figure 2.7), but ignoring the $E_i I_i$ contribution of the web[4], it yields to the same result as from Eq. (2.59) which was obtained in here by manipulation of Eq. (2.57). It must be noted that the Greek letter gamma ($\gamma$) instead of $c_s$, it is used in the EC5 Eq. (2.61) to indicate the *connection efficiency factor*. This is obviously the reason why the method adopted in the EC5 it is called 'gamma' method [Möhler, 1956].

Since Eq. (2.59) corresponds to the gamma-method's Equation applied to the particular case of an I-beam having equal flanges and a web with null bending stiffness: then, the following Eq. B.5 in Annex B of EC5, may be used for the

[4]In fact, in our case the 'web' is made up of disconnected blocks, which transfer only shear forces to the flanges, no bending at all.

*connection efficiency factor*:

$$c_s = \gamma = \left[1 + \pi^2 EAs/(KL^2)\right]^{-1} \tag{2.62}$$

Noting that EC5 Eq. (2.62) is based on the assumption that the member is pin jointed at its ends.

### 2.7.2 Modified co-rotational beam-element

Setting up the numerical model by assuming an equivalent $EI$, it can be stated that, for preliminary numerical simulations of the forming process, a value $c_s = 0$ is applied, while for successive load analyses, a $c_s > 0$ is applied (obtained e.g. by Eq. (2.62)) in order to take into account the increase in bending stiffness due to the presence of shear blocks.

Nevertheless, when setting the updated second moment of area to perform the successive (load) analysis, the change in stiffness generates unbalance forces. In other words, the system searches for the equilibrium configuration that would have resulted by forming the double-layer mat with shear blocks in place at the flat configuration. In order to maintain the equilibrium of the stress field obtained when the forming process is complete (with $I_x^{c_s=0}$) the corresponding element end reactions $M_{x,1}$, $M_{x,2}$ as from Eqs. (2.26 and 2.27), must maintain the equilibrium values ($M_{x,1}^{eq.}$, $M_{x,2}^{eq.}$) regardless of the new $I_x^{c_s>0}$ value. Therefore, the displacement's angles $\theta_{x,1}^{eq.}$ and $\theta_{x,2}^{eq.}$ need to be multiplied by a reduction factor corresponding to the ratio ($I_x^{c_s=0}/I_x^{c_s>0}$).

The difference between the local angular displacements at form finding equilibrium $\theta_x^{eq.}$ and the reduced values are:

$$\theta_{x,1}^{eq.}\left(1 - \frac{I_x^{c_s=0}}{I_x^{c_s>0}}\right) \quad ; \quad \theta_{x,2}^{eq.}\left(1 - \frac{I_x^{c_s=0}}{I_x^{c_s>0}}\right) \tag{2.63}$$

From a physical point of view, such differences can be conceived as the element's *unstressed angular displacements* that would result if the bent rods were re straightened leaving the shear blocks inserted. It is easy to imagine that, in doing such an operation, the double layer mat would not recover the flat configuration any more. In addition, the reduction of pre-stress forces — e.g. due to material (e.g. wood) relaxation — can be modelled by introducing a reducing factor $c_R \in [0,1]$ such that the unstressed local displacements become:

$$\begin{aligned} \theta_{x,1}^{eq.}\left(1-\frac{I_x^{c_s=0}}{I_x^{c_s>0}}c_R\right) \quad ; \quad (1-c_R)\theta_{y,1}^{eq.} \\ \theta_{x,2}^{eq.}\left(1-\frac{I_x^{c_s=0}}{I_x^{c_s>0}}c_R\right) \quad ; \quad (1-c_R)\theta_{y,2}^{eq.} \end{aligned} \tag{2.64}$$

Accordingly, by subtracting at each time increment the unstressed local displacements (Eqs. (2.64)) from the current element's local displacements, the force-displacements Eqs. (2.26 to 2.29) become:

$$\begin{aligned} M_{x,1} = \frac{NL_0}{30}(4\theta_{x,1}-\theta_{x,2})+ \\ +\frac{2EI_x^{c_s>0}}{L_0}\left\{2\left[\theta_{x,1}-\theta_{x,1}^{eq.}\left(1-\frac{I_x^{c_s=0}}{I_x^{c_s>0}}c_R\right)\right]+\left[\theta_{x,2}-\theta_{x,2}^{eq.}\left(1-\frac{I_x^{c_s=0}}{I_x^{c_s>0}}c_R\right)\right]\right\} \end{aligned} \tag{2.65}$$

$$\begin{aligned} M_{x,2} = \frac{NL_0}{30}(4\theta_{x,2}-\theta_{x,1})+ \\ +\frac{2EI_x^{c_s>0}}{L_0}\left\{2\left[\theta_{x,2}-\theta_{x,2}^{eq.}\left(1-\frac{I_x^{c_s=0}}{I_x^{c_s>0}}c_R\right)\right]+\left[\theta_{x,1}-\theta_{x,1}^{eq.}\left(1-\frac{I_x^{c_s=0}}{I_x^{c_s>0}}c_R\right)\right]\right\} \end{aligned} \tag{2.66}$$

$$\begin{aligned} M_{y,1} = \frac{NL_0}{30}(4\theta_{y,1}-\theta_{y,2})+ \\ +\frac{2EI_y}{L_0}\left\{2\left[\theta_{y,1}-\theta_{y,1}^{eq.}(1-c_R)\right]+\left[\theta_{y,2}-\theta_{y,2}^{eq.}(1-c_R)\right]\right\} \end{aligned} \tag{2.67}$$

$$M_{y,2} = \frac{NL_0}{30}(4\theta_{y,2} - \theta_{y,1}) + \\ + \frac{2EI_y}{L_0}\left\{2\left[\theta_{y,2} - \theta_{y,2}^{eq.}(1 - c_R)\right] + \left[\theta_{y,1} - \theta_{y,1}^{eq.}(1 - c_R)\right]\right\} \tag{2.68}$$

Eqs. (2.65 to 2.68) will be used for load analyses performed continuously with the form-finding analysis (and/or simulation of the forming process). From these, can be seen that:

- For $c_R = 0 \Rightarrow$ the local angular displacements at form finding equilibrium $\theta^{eq.}$ correspond to the *unstressed angular displacements*, or in simpler words, the geometry at completion of the forming process is stress-free (material fully relaxed).

- For $c_R = 1 \Rightarrow$ the terms $\theta_{y,1}^{eq.}$ and $\theta_{y,2}^{eq.}$ in Eqs. (2.67 and 2.68) disappear, meaning that the bending pre-stress due to the forming process is fully present. Nevertheless, a 'non-null' component of the *unstressed angular displacements* (as from Eqs. (2.63)) around the local $\bar{x}$ axis, it is still present in Eqs. (2.65 and 2.66) as a result of the shear blocks insertion.

It is important to bear in mind that: the material's relaxation factor $c_R$ is only a parameter to 'tune' the amount of pre-stress to be taken into account when performing load analyses on the form-founded geometry. In fact, relaxation/creep of wood are complex phenomena, leading to a reduction in stiffness (and strength) over time, as a result of accumulation of 'damages' at a cellular level (see Figure 2.9) and they require rheological (e.g. viscoelastic) models in order to be numerically simulated. Nonetheless, according for instance to Section 6.4.3 of Eurocode 5, a simplified (but effective) approach is allowed for the stress verification of curved laminated beams. According to this, the pre-stress induced by the forming process

can be 'neglected', provided a 'reduced' value for the design bending strength. As already explained, from a numerical modelling point of view, neglecting the pre-stress force corresponds to set $c_R = 0$.

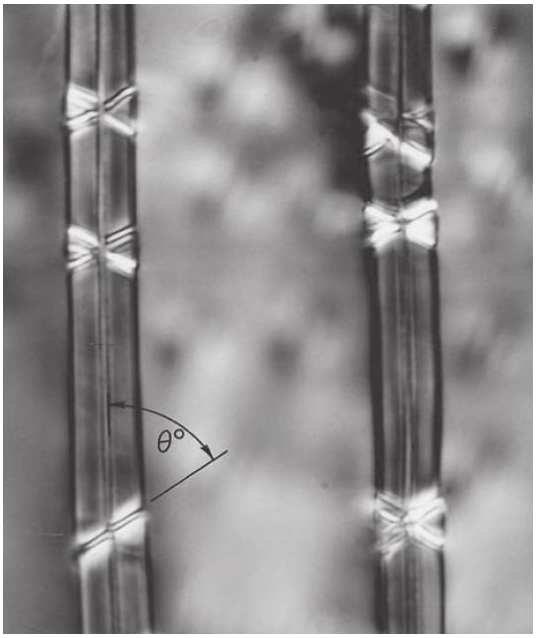


**Figure 2.9:** Formation of kinks in the cell walls of spruce timber (Picea abies) during longitudinal compression stressing (magnification x 1600, polarised light). Image©: Building Research Establishment [Domone and Illston, 2010].

### 2.7.3 Orthotropic nature of timber

As it can be seen from the element stiffness matrix in Eqs. (2.30 to 2.33), the material's behaviour is assumed to be modelled by only considering two stiffness parameters, namely: the Young modulus $E$ and the shear modulus $G$. Such an assumption is certainly valid for isotropic materials (e.g. steel). Timber, on the other hand, exhibits an highly orthotropic behaviour, which requires six independent stiffness parameters in order to be modelled. Indicating with $L$, $R$ and $T$ the lon-

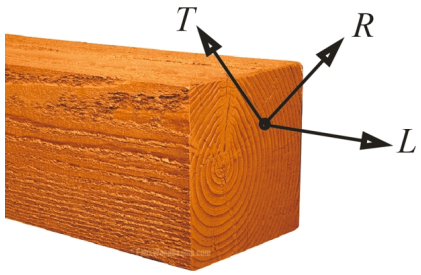


**Figure 2.10:** Orthotropic representation of Lumber: $L$ = longitudinal direction; $T$ = transversal direction; $R$ = radial direction.

gitudinal, transversal and radial (growth) directions respectively (see Figure 2.10), the constitutive stress-strain relationships of the material point are related by the following compliance matrix:

$$\begin{bmatrix} \varepsilon_L \\ \varepsilon_R \\ \varepsilon_T \\ \gamma_{RT} \\ \gamma_{LT} \\ \gamma_{LR} \end{bmatrix} = \begin{bmatrix} \frac{1}{E_L} & -\frac{\upsilon_{RL}}{E_R} & -\frac{\upsilon_{TL}}{E_T} & 0 & 0 & 0 \\ -\frac{\upsilon_{LR}}{E_L} & \frac{1}{E_R} & -\frac{\upsilon_{TR}}{E_T} & 0 & 0 & 0 \\ -\frac{\upsilon_{LT}}{E_L} & -\frac{\upsilon_{RT}}{E_R} & \frac{1}{E_T} & 0 & 0 & 0 \\ 0 & 0 & 0 & \frac{1}{G_{RT}} & 0 & 0 \\ 0 & 0 & 0 & 0 & \frac{1}{G_{LT}} & 0 \\ 0 & 0 & 0 & 0 & 0 & \frac{1}{G_{LR}} \end{bmatrix} \cdot \begin{bmatrix} \sigma_L \\ \sigma_R \\ \sigma_T \\ \tau_{RT} \\ \tau_{LT} \\ \tau_{LR} \end{bmatrix} \tag{2.69}$$

The ratios between the three Young moduli ($E_L$; $E_R$ and $E_T$) and the three shear moduli ($G_{LR}$; $G_{LT}$ and $G_{RT}$) vary with species, moisture content, temperature, rate of loading and several other variables. According to Bodig and Jayne [1981]: *"In spite of the many sources of variation, in general, the moduli are related according*

*to the following ratios:"*

$$\begin{aligned} E_L/E_R/E_T &\approx 20/1.6/1 \\ G_{LR}/G_{LT}/G_{RT} &\approx 10/9.4/1 \\ E_L/G_{LR} &\approx 14.1 \end{aligned} \tag{2.70}$$

As it can be seen, the transversal and radial Young moduli ($E_T$ and $E_R$) are approximately one order of magnitude smaller than the longitudinal Young modulus ($E_L$). Also, the shear modulus $G_{RT}$ is approximately one order of magnitude smaller than the shear moduli $G_{LR}$ and $G_{LT}$. On this basis, a further approximation can be made: the number of independent stiffness parameters can be further reduced to only four. More precisely: an elastic modulus parallel to the grain ($E_0$) and orthogonal to the grain ($E_{90}$):

$$\begin{aligned} E_0 &= E_L \\ E_{90} &\approx E_R \approx E_T \end{aligned} \tag{2.71}$$

as well as a transverse shear modulus ($G_{transverse}$) and a rolling shear modulus ($G_{rolling}$):

$$\begin{aligned} G_{transverse} &\approx G_{LR} \approx G_{LT} \\ G_{rolling} &= G_{RT} \end{aligned} \tag{2.72}$$

Such a particular case of anisotropy, with only four independent parameters, it is known as *transverse isotropy*[5] and it is adopted in Timber Engineering practice and standards (e.g in the Eurocode 5) in order to describe and modelling the behaviour of structural members. Therefore, the Young and shear moduli to consider for our beam-element formulation Eqs. (2.30 to 2.33) will be: $E_0$ and $G_{rolling}$ respectively. $E_0$ will dictate the material's contribution to the beam's axial and bending stiffnesses, whilst $G_{rolling}$ will define the material's contribution in terms of torsional rigidity for the beam.

[5] A transversely isotropic material exhibits properties which are symmetric about an axis (the grain direction in our case) that is normal to a plane of isotropy.

### 2.7.4 Stress field

On the basis of the described modified co-rotational beam-element (Section 2.7.2), the distribution of normal stress $\sigma$ at the external fibres of the beam cross-section along the element, can be obtained from the curvature values $\kappa_x$ and $\kappa_y$. By deriving the *Hermite* cubic shape function $\bar{r}(t)$ with respect to the parameter $t \in [0, 1]$ representing the relative position along the element, (see Eq. 2.50) the curvature functions $\kappa_x(t)$ and $\kappa_y(t)$ around the element local axes, are[6] [Adriaenssens, 2000]:

$$\begin{aligned} \kappa_x(t) &= \frac{(6t-2)\theta_{x,1} + (6t-4)\theta_{x,2}}{|\bar{p}|} \\ \kappa_y(t) &= -\frac{[(6t-2)\theta_{y,1} + (6t-4)\theta_{y,2}]}{|\bar{p}|} \end{aligned} \tag{2.73}$$

where $|\bar{p}|$ is modulus of the vector connecting the element's end nodes (see Figure 2.2). As previously done for the load-displacement functions, by subtracting at each time increment the *unstressed angular displacements* from the current element's angular displacements, the curvature functions (Eqs. (2.73)) become:

$$\begin{aligned} \kappa_x(t) &= \frac{1}{|\bar{p}|}\left\{(6\mathbf{t}-\mathbf{c})\cdot[\mathbf{\Theta}_x - (1-c_R)\mathbf{\Theta}_x^{eq.}]\right\} \\ \kappa_y(t) &= -\frac{1}{|\bar{p}|}\left\{(6\mathbf{t}-\mathbf{c})\cdot\left[\mathbf{\Theta}_y - (1-c_R)\mathbf{\Theta}_y^{eq.}\right]\right\} \end{aligned} \tag{2.74}$$

where:

$$\mathbf{t} = \begin{bmatrix} t \\ t \end{bmatrix} \quad ; \quad \mathbf{c} = \begin{bmatrix} 2 \\ 4 \end{bmatrix} \quad ; \quad \mathbf{\Theta}_x = \begin{bmatrix} \theta_{x,1} \\ \theta_{x,2} \end{bmatrix} \quad ; \quad \mathbf{\Theta}_y = \begin{bmatrix} \theta_{y,1} \\ \theta_{y,2} \end{bmatrix} \tag{2.75}$$

Noting that:

- For $c_R = 0 \Rightarrow$ the curvatures generated by the forming process correspond to the *unstressed curvature values* (stress-free geometry).

[6] In [Adriaenssens, 2000] $\kappa_x(t)$ and $\kappa_y(t)$ are parametrised assuming $t \in [-0.5, +0.5]$.

- For $c_R = 1 \Rightarrow$ Eqs. (2.73) and (2.74) give the same result (geometry fully pre-stressed).

Accordingly, assuming the bending stress as:

$$\sigma(t) = \sigma_x(t) + \sigma_y(t) \tag{2.76}$$

the bending stress $\sigma_y$ can be obtained from the second of Eqs. (2.74) as:

$$\sigma_y(t) = \frac{bE\kappa_y(t)}{2} \tag{2.77}$$

while $\sigma_x$ will be a function of $\kappa_x(t)$ plus some other term due to the presence of shear blocks. With reference to Figure 2.11:

$$\sigma_x(t) = \sigma_{x,a} + \sigma_{x,b} = \frac{hE\kappa_x(t)}{2} + \frac{N_s(t)}{bh} \tag{2.78}$$

where $N_s(t)$ is obtained from the following lever-arm relation:

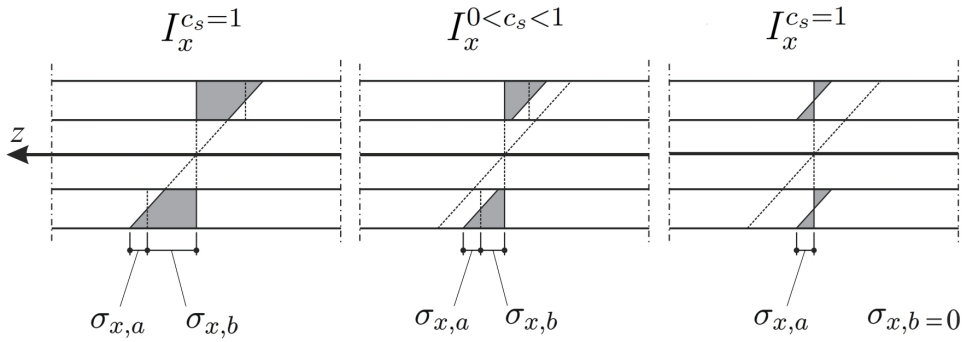


**Figure 2.11:** Built-up cross-section: Normal stress distribution ($\sigma_x$) for different values of the connection efficiency factor ($c_s$).

$$N_s(t) = \frac{M_{x,b}(t)}{(h + h_s)} \tag{2.79}$$

and $M_{x,b}(t)$ computed considering only the contribution to $EI_x$ due to shear blocks (only the first term of Eq. (2.59)):

$$M_{x,b}(t) = EI_{x,b}\kappa_x(t) \quad ; \quad I_{x,b} = c_s \frac{(h + h_s)^2}{2} bh \tag{2.80}$$

Since the moment contribution $M_{x,b}(t)$ and stress contribution $\sigma_{x,b}$ (both) due to shear blocks only occur after the grid-shell is formed (bent); for $\theta_{x,1} = \theta_{x,1}^{eq.}$ and $\theta_{x,2} = \theta_{x,2}^{eq.} \Rightarrow M_{x,b}(t)$ and $\sigma_{x,b}$ must be null. Therefore $\kappa_x(t)$ in Eq. (2.80) is calculated by setting $c_R = 0$ in Eq. (2.74) regardless of the $c_R$ value used to compute the element reaction forces (Eqs. (2.65 to 2.68)) and the bending stress $\sigma_{x,a}$. Accordingly:

$$M_{x,b}(t) = Ec_s bh \frac{(h+h_s)^2}{2|\bar{p}|} \left[(6\mathbf{t} - \mathbf{c}) \cdot (\mathbf{\Theta}_x - \mathbf{\Theta}_x^{eq.})\right] \tag{2.81}$$

with $\mathbf{t}$, $\mathbf{c}$ and $\mathbf{\Theta}_x$ as given in Eqs. (2.75). Substituting then Eq. (2.81) into Eq. (2.79) and (2.78):

$$\sigma_{x,b}(t) = Ec_s \frac{(h+h_s)}{2|\bar{p}|} \left[(6\mathbf{t} - \mathbf{c}) \cdot (\mathbf{\Theta}_x - \mathbf{\Theta}_x^{eq.})\right] \tag{2.82}$$

Hence, Eq. (2.78) becomes:

$$\begin{aligned}\sigma_x(t) = \frac{E}{2|\bar{p}|} \Big\{ &(hc_s + h_s c_s + h) \left[(\theta_{x,1} - \theta_{x,1}^{eq.})(6t-2) + (\theta_{x,2} - \theta_{x,2}^{eq.})(6t-4)\right] + \\ &+ hc_R \left[\theta_{x,1}^{eq.}(6t-2) + \theta_{x,2}^{eq.}(6t-4)\right] \Big\}\end{aligned} \tag{2.83}$$

### 2.7.5 Shear blocks reactions

In order to verify the shear block connections strength, the shear reaction force $T_s$ generated by the blocks needs to be known. From beam's theory we know that the distribution of internal shear along the beam's centreline (in our case from $t = 0$ to $t = 1$) corresponds to the derivative of the internal moment function $M(t)$. Formally:

$$T_s(t) = \frac{\partial M}{\partial t} \tag{2.84}$$

Since we are only interested in the component of internal shear due to the effect of shear blocks, the moment to consider in Eq. (2.84) to derive $T_s$ is that given in

Eq. (2.81). By doing so, the following expression for the shear block's reaction is obtained:

$$T_s = Ec_s bh \frac{3(h+h_s)}{|\bar{p}|}(\theta_{x,1} - \theta_{x,1}^{eq.} + \theta_{x,2} - \theta_{x,2}^{eq.}) \tag{2.85}$$

Nothing that: by computing $T_s$ as the finite-difference of the variation of axial force $N_s(t)$ along the beam centreline:

$$T_s = N_s(t=1) - N_s(t=0) \tag{2.86}$$

would have led to the same expression as in Eq. (2.85). With $T_s$ so found, the shear block strength along the beam-element is verified by making sure that:

$$\frac{|T_s|}{T_m S} \leq 1 \tag{2.87}$$

where $S$ is the number of blocks per element and $T_m$ the shear block connection strength. Accordingly, the strength verification for the shear block connections is performed at an element level rather than at single shear block connection level.

### 2.7.6 Model limitations

As mentioned in Section 2.7.1, the described model for layered beams assumes compatibility of displacements (interlayer slips) and curvatures. In other therms, the model neglects the contribution to deformation due to the presence of the horizontal shear forces. Such an (Euler-Bernoulli) assumption leads to higher bending stiffness values, for the numerically modelled members, compared to a more realistic Timoshenko beam model. On this basis, the use of the co-rotational beam-element in here described should be limited to the modelling of 'relatively' thin members.

## 2.8 Summary

A two-step analysis for the Form-finding of actively bent timber grid-shells was defined in the present Chapter. An explicit resolution method (DR) in conjunction with a co-rotational beam-element with six DoF, are adopted for the described analysis. Procedures to assign local and global constraints, both needed to simulate the connection joints as well as to 'force' the grid-shell shape to assume a shape close to a reference surface, were introduced in here. An algorithm to find the grid cutting pattern was also described, and a modified version of the co-rotational beam-element, originally proposed by Williams (see [Adriaenssens, 2000]) was introduced in here to simulate the change in bending stiffness of the members occurring during construction. Formulae to calculate the stress distribution of the composite (double-layer) timber members have been provided as well.

# Chapter 3

# Form-finding and analysis: validation and results

The theory described in the previous Chapter has been tested and validated against a series of analytical, numerical and experimental benchmark tests, hence reported in the present Chapter.

## 3.1 Co-rotational beam element: validation

### 3.1.1 Elastica

The co-rotational beam-element formulation, and its resolution by DR method (as described in Sections 2.3-2.4) is firstly tested, in the bi-dimensional case, against the analytical solution of an initially straight elastic rod pinned at its ends. Figure 3.1 details the corresponding *Elastica* shapes for the effect of four increasing values of the axial load $P$ over the critical Euler buckling value $P_{cr}$, identifying each shape with the corresponding inclination angle of the end's tangential direction.

The load values of $P$ corresponding to the four shapes, are obtained according

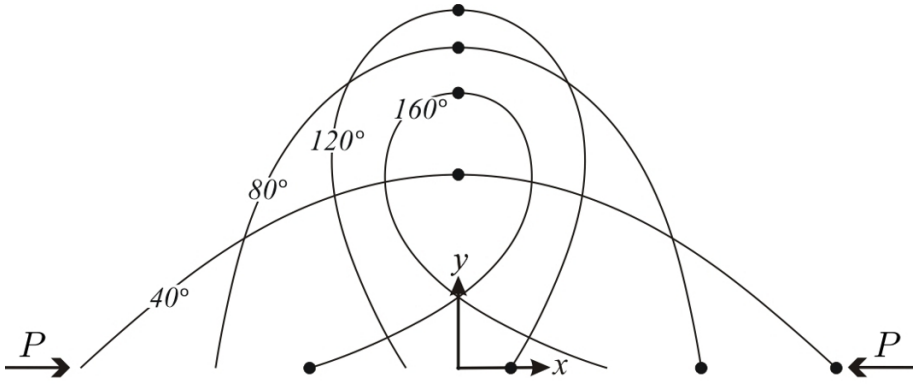


**Figure 3.1:** *Elastica* shapes under four buckled states. The numerical $x$ displacement and $y$ displacement errors of the right-end and midspan nodes, are reported in Fig. 3.2.

to Timoshenko and Gere [1961][1] as: $P = (K^2 \cdot EI)L^{-2}$. A bending stiffness $EI = 100$ kNm$^2$ and an axial stiffness $EA = 100$ MN were set. The rod's length is 10.0 m. For each of the four buckled states, five DR analyses with increasing number of elements (20, 24, 28, 32 and 36) were performed. The analyses were stopped when the following inequality limit was reached: $max|\bar{R}_i| \leq$ 9.5e-6$P$. The numerical $x$ displacement of the rod's right-end node and $y$ displacement of the mid-span node are compared to the corresponding analytical values in terms of error percentage, and are summarized in Figure 3.2.

$$x[\%] = \frac{100|x^A - x^{DR}|}{x^A} \quad ; \quad y[\%] = \frac{100|y^A - y^{DR}|}{y^A} \tag{3.1}$$

As expected, the numerical error is inversely proportional to the number of elements used to modelling the discrete rod. Higher error percentages are registered for the $40°$ buckled state, with a maximum error of 1.5% most probably due to axial deformation (not taken into account in the analytical solution) of the numerical

[1]The length $L$ in [Timoshenko and Gere, 1961] corresponds to $L/2$ of the present study; The *complete elliptic integral of the first kind* ($K$) has been calculated up to the 10$^{\text{th}}$ decimal place in order to maintain high accuracy of the analytic solution of $P$.

model. Remarkably, the error of the 36 elements model, falls below the 0.5% for all of the four buckled configurations.

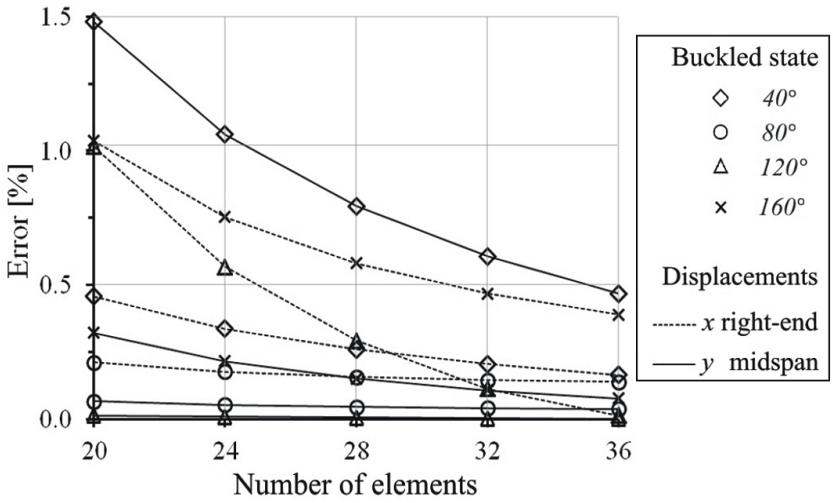


**Figure 3.2:** Numerical error of displacements at different discretization values for a buckled elastic rod (shown in Fig. 3.1).

### 3.1.2 Combined bending and torsion

A further numerical test, on the single rod case, is performed to assess the reliability of the formulation in the three-dimensional case, involving combined bending moment and torsion effects: Firstly, a 10 m long rod is bent as in the previous test (dashed line in Figure 3.3) until a distance between ends of 6.2 m is reached. Secondly, the rod is prevented from rotating around the global $x$ axis at its end nodes and combinations of increasing forces $\bar{P}$ and constant torque $\bar{Q}$ are applied at the midspan node. The analyses described were then replicated with the commercial Finite Element software Abaqus, with Newton-Raphson solver (NR), to handle *large displacements.* A 36-element geometry was set up for both NR and DR models, while the axial and bending stiffnesses were set in accordance to the

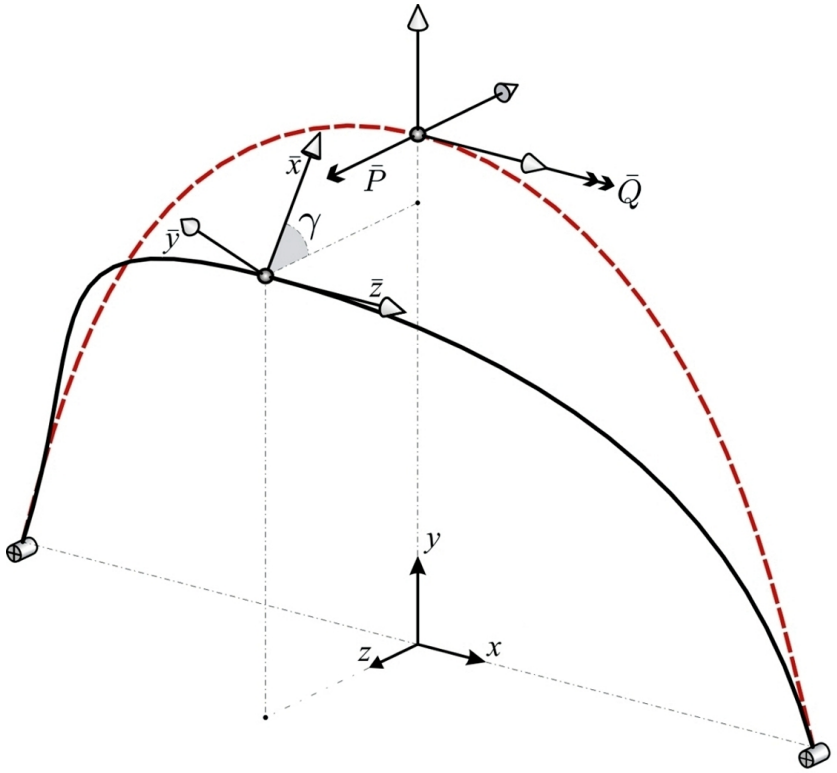


**Figure 3.3:** Combined bending and torsion numerical tests set up: Displacements $y$, $z$ and rot. angle $\gamma$ of the midspan node for different $\bar{P}$-$\bar{Q}$ values are reported in Tab. 3.1.

previous test ($I_x = I_y = I$) as well as the convergence criteria. In addition, a torsional stiffness value $GJ = 50$ kNm$^2$ was assumed.

The resulting $y$ and $z$ displacements and rotation angle $\gamma$ at the mid-span node, for five $\bar{P}$-$\bar{Q}$ load combinations, obtained with both NR and DR methods, are reported in Table 3.1. As can be seen, both methods gave very close results, especially if we consider the magnitude of displacements involved. At load case **5** the midspan node achieved a lateral ($z$) displacement of more than 1.6 m, with an occurring discrepancy between NR and DR analyses output of 0.9 cm ($\approx 0.5\%$) and a difference between vertical ($y$) components of 0.5 cm on a total value of almost 3 m ($\approx 0.16\%$). Not least, the rod's cross section at the midspan node undergone a

**Table 3.1:** NR and DR methods: Comparison of displacement values at the midspan node of a pre-stressed rod under five load combinations (see Fig. 3.3).

| Load case | **1** | | **2** | | **3** | | **4** | | **5** | |
|---|---|---|---|---|---|---|---|---|---|---|
| $P$ [kN] | 0.0 | | 5.0 | | 10.0 | | 15.0 | | 20.0 | |
| $Q$ [kNm] | 10.0 | | 10.0 | | 10.0 | | 10.0 | | 10.0 | |
| | NR | DR | NR | DR | NR | DR | NR | DR | NR | DR |
| $y/L^a$ | 0.3421 | 0.3420 | 0.3357 | 0.3359 | 0.3251 | 0.3255 | 0.3119 | 0.3124 | 0.2975 | 0.2980 |
| $z/L$ | 0.0239 | 0.0235 | 0.0656 | 0.0645 | 0.1032 | 0.1018 | 0.1358 | 0.1344 | 0.1633 | 0.1621 |
| $\gamma$ [rad] | 0.5646 | 0.5664 | 0.6807 | 0.6789 | 0.7856 | 0.7814 | 0.8754 | 0.8701 | 0.9498 | 0.9442 |

[a] $L$ =10.0m

rotation $\gamma$ of 0.942 rad (circa $54°$) corresponding to a gap of only 0.0052 rad ($0.3°$) between NR and DR outputs ($\approx 0.5\%$). For completeness of results, the bending reactions $M_x$, $M_y$ at the elements midpoint and torsion $M_\varphi$ (second of Eqs. 2.25) outputs of the DR analyses under load case **2**, are compared to the corresponding NR outputs and summarized in table 3.2.

**Table 3.2:** NR and DR methods: Comparison of internal reactions, measured at the elements midpoint, under the ($\bar{P}$-$\bar{Q}$) load case **2**.

| Elem. internal reaction [kNm] | $M_x$ | | $M_y$ | | $M_\varphi$ | |
|---|---|---|---|---|---|---|
| Elem. index | NR | DR | NR | DR | NR | DR |
| 1 | 1.12 | 1.14 | -33.65 | -33.38 | 5.03 | 5.00 |
| 6 | 13.81 | 13.84 | -20.75 | -20.63 | 5.03 | 5.00 |
| 11 | 28.88 | 28.89 | -10.67 | -10.65 | 5.03 | 5.00 |
| 16 | 44.56 | 44.50 | -3.61 | -3.58 | 5.03 | 5.00 |
| 21 | 44.56 | 44.50 | -3.61 | -3.58 | -5.03 | -5.00 |
| 26 | 28.88 | 28.89 | -10.67 | -10.65 | -5.03 | -5.00 |
| 31 | 13.81 | 13.84 | -20.75 | -20.63 | -5.03 | -5.00 |
| 36 | 1.12 | 1.14 | -33.65 | -33.38 | -5.03 | -5.00 |

## 3.2 Spherical dome

This example provides a description of the developed method, with a practical application to the form-finding and load analysis of a grid-shell dome.

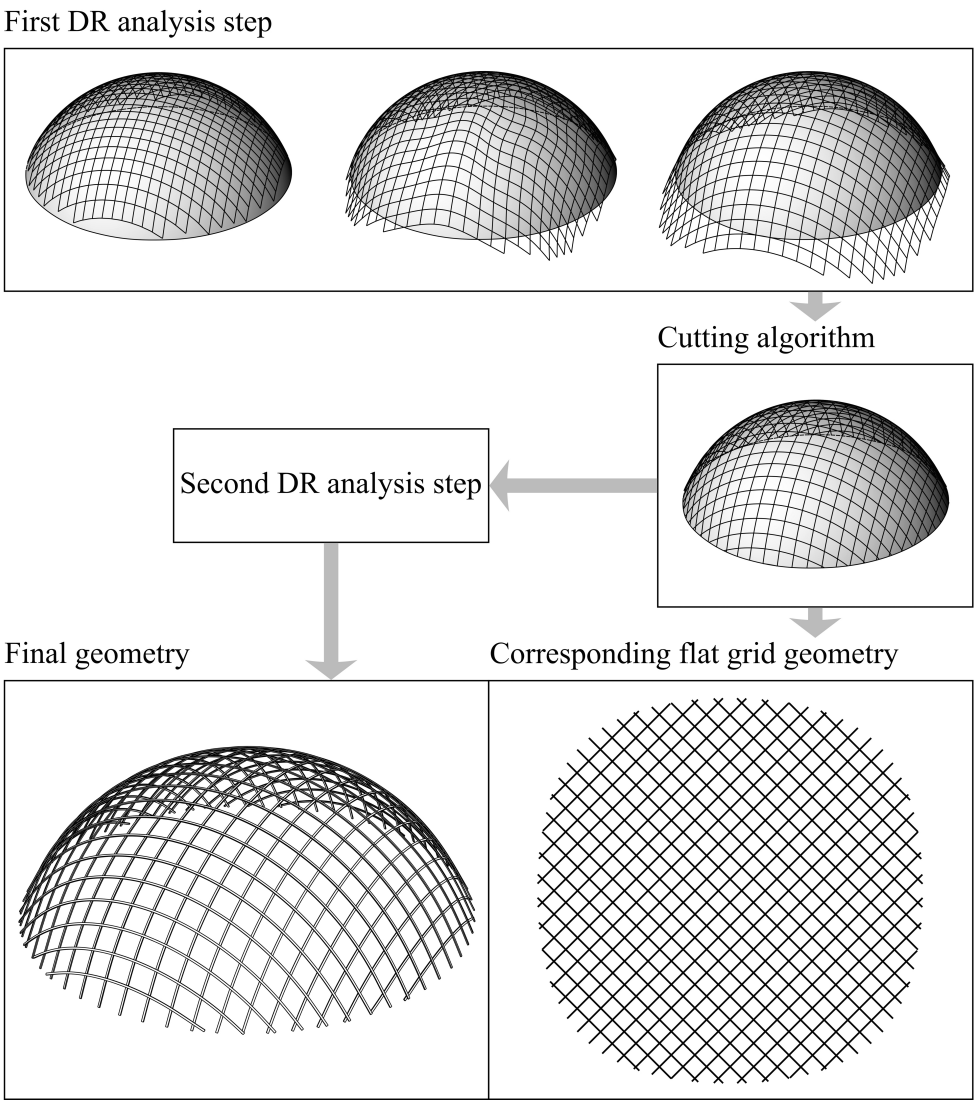


**Figure 3.4:** Form finding of a grid-shell dome by two-step procedure: Flowchart.

### 3.2.1 Form-finding

The reference surface is described by the equation $f(\bar{r})$ of a sphere having radius of 11 m and its centre coinciding with the global axes origin. The subspace of interest **B** is defined by $z \geq 4.582$ m such that, each grid node whose $z$ coordinate (at each time increment) is lower than such value: the node will not be constrained to the surface. Accordingly, the part of reference surface contained in **B** configures a spherical cap with a span of 20 m and circa 6.4 m high. The unstressed length $L_0$ of the members of the two-way grid is set to 1 m. A flowchart of the form finding procedure is illustrated in Figure 3.4: At completion of the first analysis step, the resulting mesh outside the subspace of interest it is cut with the method previously described (Section 2.6). The grid geometry so obtained is then used to find the corresponding flat mat by 'relaxing' it on a flat surface. In fact, although geometrically different, the two meshes have the same topology. Unlike for the single rod case, no analytical solution, for a complete grid-shell system, is readily available to compare with the numerical solution. However, restricting the investigation to the assessment of the (global) grid node's displacements only for effect of the geometric constraints (constant elements length; reference surface) a comparison of outputs can be made with other discrete models. In the particular case of a spherical surface, the expression to calculate a corresponding discrete mesh with constant edge-length (Chebyshev net) thus constant arch-length[2], is given by Bobenko and Pinkall [1996]: Assuming the nodes of the Chebyshev net defined by a $(n \times m)$ matrix, the unit vector $\bar{\omega}$ normal to the spherical surface at node $\bar{r}_{n+1,m+1}$ can be found from the unit vectors at nodes $\bar{r}_{n,m}$; $\bar{r}_{n+1,m}$ and $\bar{r}_{n,m+1}$ by:

$$\bar{\omega}_{n+1,m+1} = -\bar{\omega}_{n,m} + \frac{\bar{\omega}_{n,m} \cdot (\bar{\omega}_{n+1,m} + \bar{\omega}_{n,m+1})}{1 + (\bar{\omega}_{n+1,m} \cdot \bar{\omega}_{n,m+1})}(\bar{\omega}_{n+1,m} + \bar{\omega}_{n,m+1}) \tag{3.2}$$

[2]To the case of spherical surface: for an arbitrary set of chords with constant length the corresponding geodesic arch-length is always constant.

Consequently, for a sphere with its centre coinciding to the origin of the global coordinate system, the nodal coordinates are given by:

$$\bar{r}_{n+1,m+1} = (sphere\ radius)\bar{\omega}_{n+1,m+1} \tag{3.3}$$

On this basis, a Chebyshev net has been generated on a quarter of the spherical cap previously described, as shown in Figure 3.5a. The nodes $\bar{r}_{n,0}$ and $\bar{r}_{0,m}$ of the first raw and column of the matrix, are those obtained at completion of the first DR analysis step (grid still constrained to the surface) thus, the remaining entries of the matrix are obtained by applying Eqs. (3.2, 3.3). The error percentage is calculated as:

$$Error[\%] = \frac{100|\bar{r}^{DR} - \bar{r}^{Cheb.}|}{sphere\ radius} \tag{3.4}$$

As can be seen from Figure 3.5b, the error increases with the distance from the axes of the matrix. Despite the arch-length of the Chebyshev net edges coinciding with the arch-length of the DR cubic splines at the $\bar{r}_{n,0}$ and $\bar{r}_{0,m}$ nodes, the discontinuity of tangents between consecutive Chebyshev net (geodesic) arches increases as we move away from the matrix axes. In any case, the discrepancy of outputs between the two geometries remains below the 0.01 %.

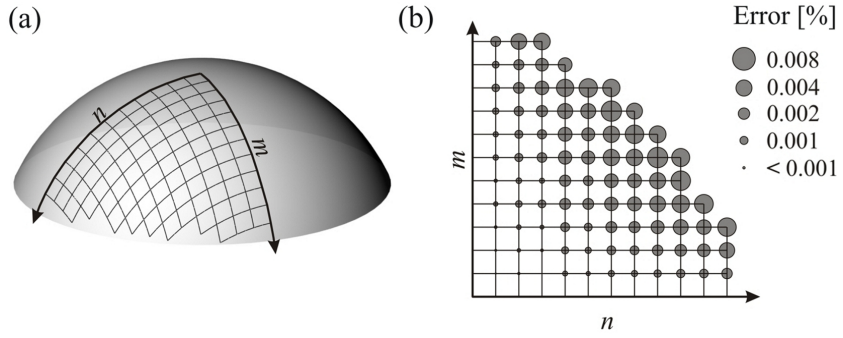


**Figure 3.5:** Spherical cap: (a) Chebyshev net found by Eqs. (3.2 - 3.3) ; (b) Comparison of DR output with the Chebyshev net geometry.

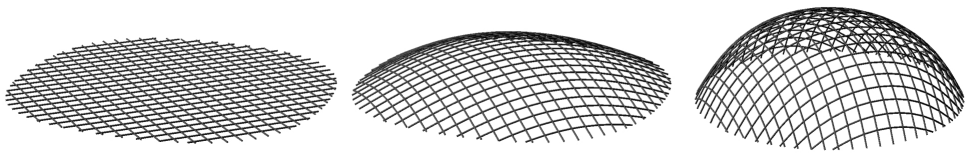

**Figure 3.6:** Spherical cap: Preliminary form finding analysis by NR (implicit) method. Grid cutting pattern and final position of the boundary nodes are those obtained at DR completion of the first form finding step.

### 3.2.2 Load-analysis

The single-layer grid-shell dome, obtained in the previous example, is submitted for a load analysis performed with both DR and NR methods, thus a comparison of results is provided. Material and cross-sectional stiffnesses are those set for the previously described single-rod tests. In order to take into account the effect of pre-stress forces for the NR analysis, a preliminary (form finding) analysis step is performed by imposing a set of displacements to the boundary nodes of the flat mat geometry (as shown in Figure 3.6) where: both flat mat geometry and final position of the boundary nodes are those obtained by the DR procedure previously illustrated. Further, for the NR analysis, the cylindrical joint connections are simulated by means of link elements, with a fictitious size of only 0.1 mm, in order to replicate the behaviour of the single-node model adopted for the DR analysis.

For both DR and NR analyses, a gravitational load $P$ is applied at each node of the structure by increments of 0.2 kN per node (up to 2 kN). For each load increment (load step) the equilibrium geometry is computed and the (average) vertical displacement, of the four nodes at the summit of the grid dome, is recorded. The equilibrium convergence criteria for the DR load steps was set to: $max|\bar{R}_i| \leq 5$ N. The resulting load-displacement curves are reported in Figure 3.7, according to which, the two analyses gave very close results, with a maximum discrepancy

$< 1\%$. The deformed geometry for $P = 2$ kN per node obtained by DR method, is shown in Figure 3.8 with a magnification factor of 30.

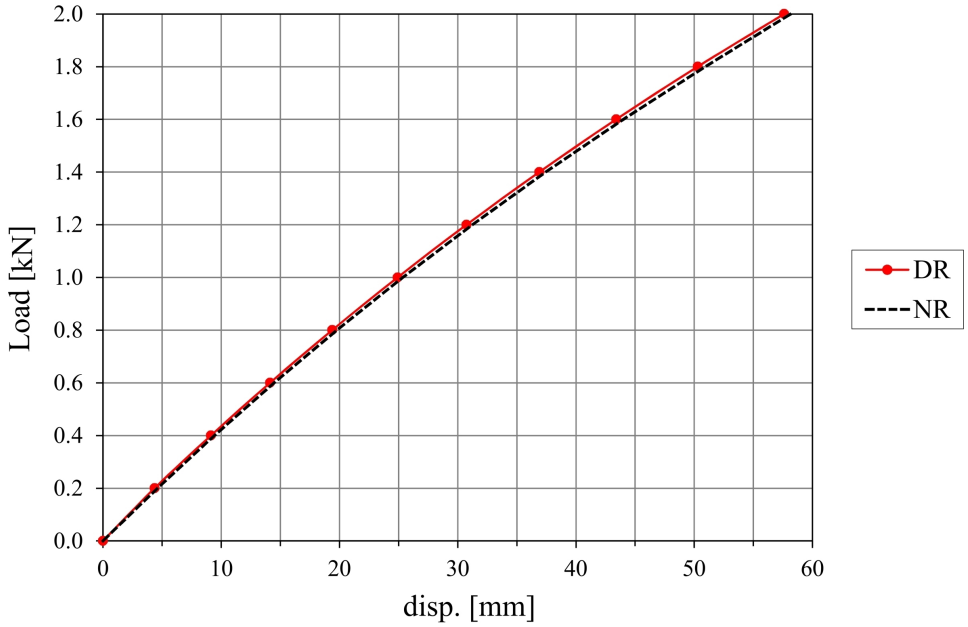


**Figure 3.7:** Grid shell dome: Load-displacement curves by DR and NR methods.

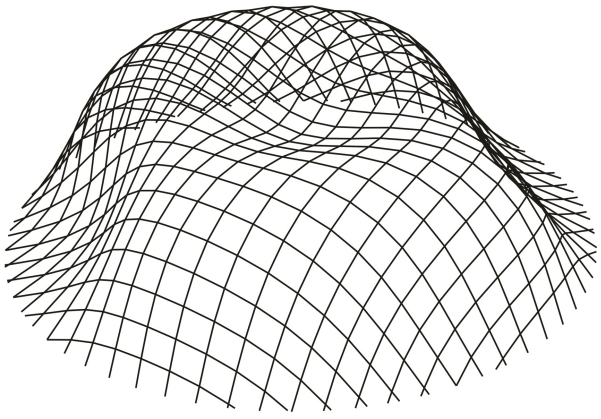

**Figure 3.8:** Load analysis of the grid-shell dome: Deformed geometry (magnified 30 times) obtained by DR method for $P = 2$ kN per node.

## 3.3 Corrugated barrel vault

In the present example, a reference surface is defined in such a way to replicate the overall shape of the Downland grid shell: The resulting corrugated barrel vault is 50 m long, with a varying width of 12.5 m to 16 m, while the height varies from 9.5 m at the central hump to circa 7.4 m at the saddles [Kelly et al., 2001]. According to the adopted surface function (see Appendix A.2: Corrugated barrel vault shape function), the global $(x, y)$ plane coincides with the ground floor level of the real structure, whose longitudinal axis is directed along the $y$ global direction. Hence, **B** is defined by: $(z \geq 0.0$ m) and $(-25.0$ m $\leq y \leq 25.0$ m).

According to Harris et al. [2003] the timber specimens were graded as D30 of the BS-EN-338 [2008] strength classification, for which a mean modulus of elasticity parallel to the grain ($E_{0,mean}$) of 11 kN/mm$^2$ is given. Such value is estimated from tests on timber population at a temperature of 20°C and relative humidity of 65 %. In these environmental conditions, the *moisture content* (MC) of wood in general does not exceed 12 % (dry timber) while the green oak used for the Downland grid shell construction had a corresponding MC up to 65 % [Harris et al., 2003]. For values of MC over the *fibre saturation point* (around 27 %) a reduction in stiffness and strength occurs. In order to take this into account, a $E_{dry}/E_{green}$ ratio of 1.3 [ASTM, 2006] is used to derive a 'reasonable' value of elastic modulus ($E = E_{0,mean}/1.3 = 8.46$ kN/mm$^2$) for input in Eqs. (2.25 to 2.29). A mean value of 0.69 kNmm$^2$ [BS-EN-338, 2008] is set for the transverse shear modulus $G$. The initial rectangular mat's overall shape [Harris et al., 2003] is preserved during the form finding analysis by restraining the vertical displacements of the boundary nodes of the mat's longer side. The grid shell geometry at form finding completion is shown in Figure 3.9. It has to be noted that: due to the inhomogeneity of the material, the strength values variate greatly within timber specimens. This is

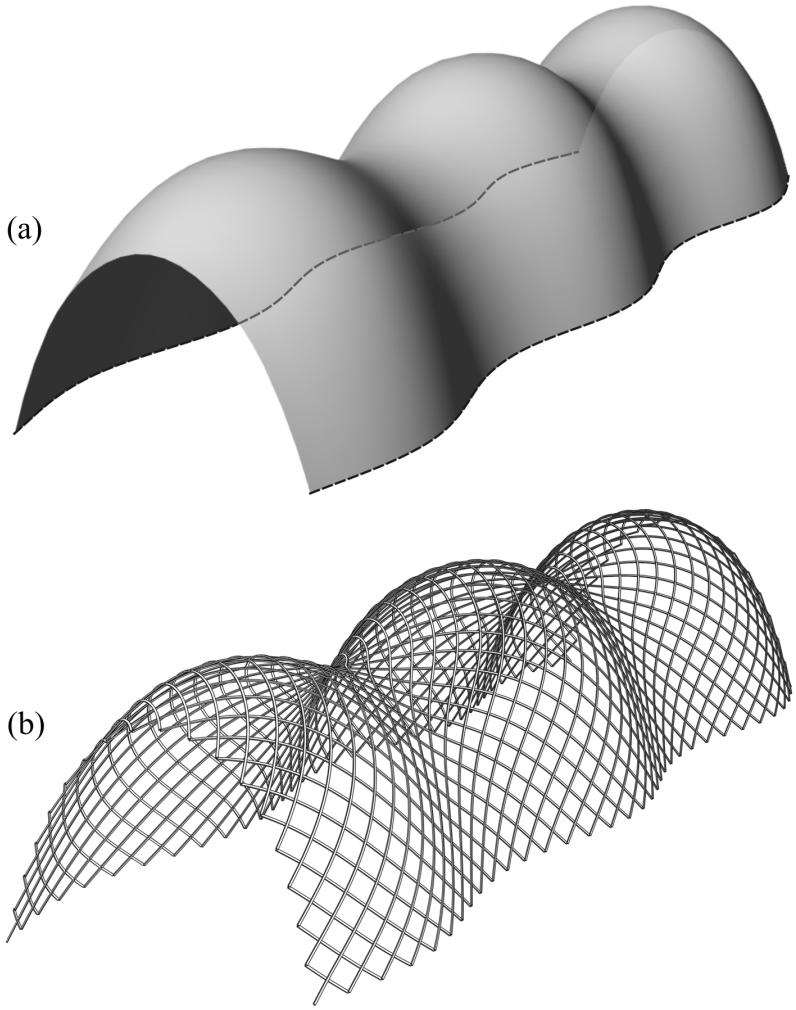


**Figure 3.9:** Corrugated barrel vault: (a) Reference surface; (b) Final geometry.

due to the presence of 'defects' such as short grain, knots, and other kind of material discontinuities typical of timber. For instance, in the case of the Downland grid-shell, the timber laths used for the construction were 'optimised' by inspecting each specimen and cutting away the piece of timber in correspondence of defects[3], hence, gluing the cut lath back together by finger joints (see Figure 3.10),

[3]The automated process was carried out using the GreCon Dimter OPTICUT 101 mechanised saw [Harris et al., 2003].

eventually obtaining six-metre-long ‘defect-free’ timber laths, to be scarf jointed (on-site) end-to-end into continuous members. [Harris et al., 2003].

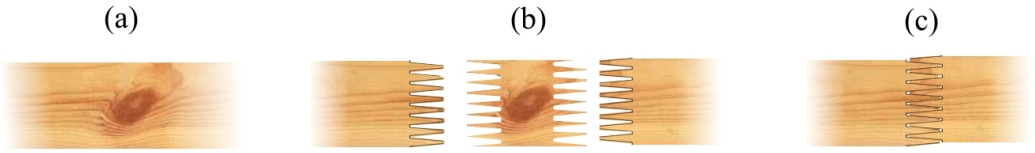


**Figure 3.10:** Optimisation of raw timber laths by automated machinery: (a) Individuation of defect by optical sensor; (b) cutting of the defected piece; (c) joining of the lath into a single continuous member by means of finger joint.

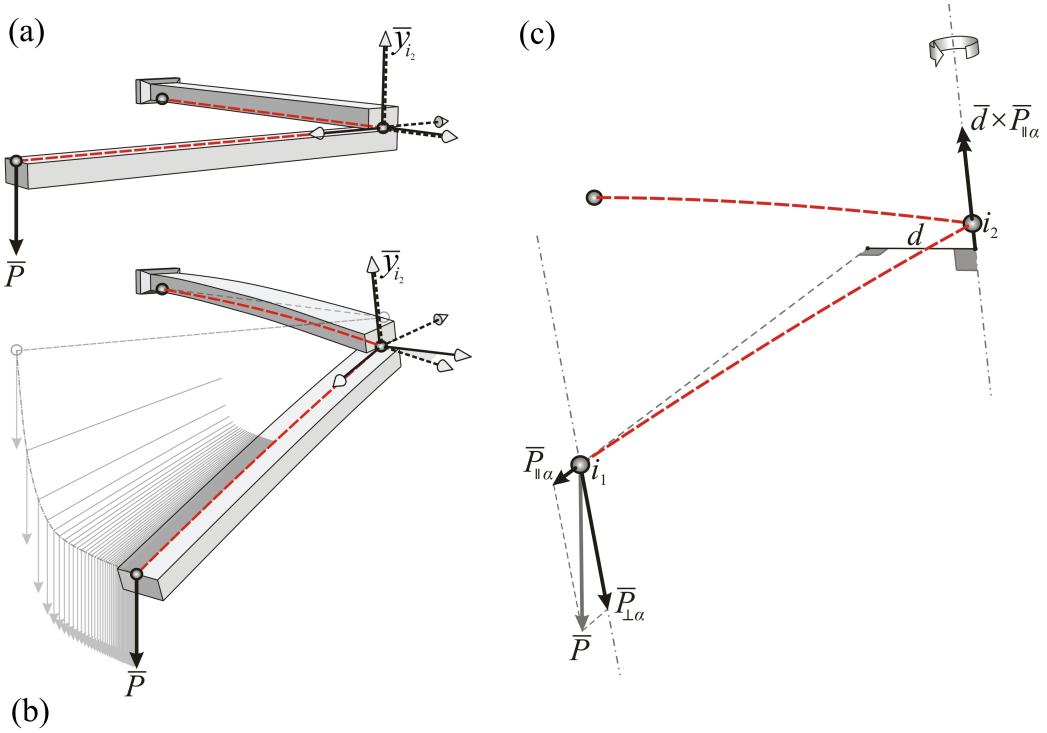


**Figure 3.11:** Single-node cylindrical joint: (a) Unloaded configuration; (b) Deformed configuration; (c) Decomposition of the applied load $\bar{P}$ in a parallel and an orthogonal component relative to the joint rotational axis.

## 3.4 Cylindrical hinge-joint: validation

The aim of the following numerical test is to demonstrate the validity of the single-node cylindrical joint model introduced in Section *2.5.1*. Two rods (with length of 1 m each) are joined together at their 'common' node by means of cylindrical joint, thus defining an overall 'L' shape with internal angle of $90°$.

Then, the first rod is clamped at its start node, while, a vertical load $\bar{P}$ of 15 kN is applied at the end-node of the second rod (see Figure 3.11). Material and cross-sectional stiffnesses ($E$, $G$, $A$, $I_x$, $I_y$ and $J$) are set in accordance to the previously described tests in Section 3.1, as well as the convergence criteria.

Only two elements per rod are considered. Sufficient condition, for validation of the joint's functioning is making sure that: no torque occurs around the joint's rotational axis at equilibrium convergence. Indicating with $\bar{y}_{i_2}$ the joint's rotational axis at time $t$, and $\alpha$ the corresponding normal plane, the applied load $\bar{P}$ can be decomposed in two vectors:

$$\bar{P} = \bar{P}^t_{\perp\alpha} + \bar{P}^t_{\parallel\alpha} \tag{3.5}$$

Although magnitude and direction of load remain unchanged throughout the analysis, the joint's rotational axis does not. In fact, at initial configuration (Figure 3.11a) we have that $\bar{y}_{i_2}$ is aligned to $\bar{P}$, meaning that $\bar{P}^{t=0}_{\parallel\alpha} = \bar{0}$ thus no rotation occurs. However, as soon as the clamped rod starts bending and bowing (Figure 3.11b) the alignment between the vector load $\bar{P}$ and the joint rotational axis is lost, thus $\bar{P}^t_{\parallel\alpha} > \bar{0}$ and a rotation is triggered. In order for the system to reach a static equilibrium, sufficient condition is the nullification of the out-of-balance torque around the joint rotational axis:

$$d|\bar{P}_{\parallel\alpha}| \approx 0 \tag{3.6}$$

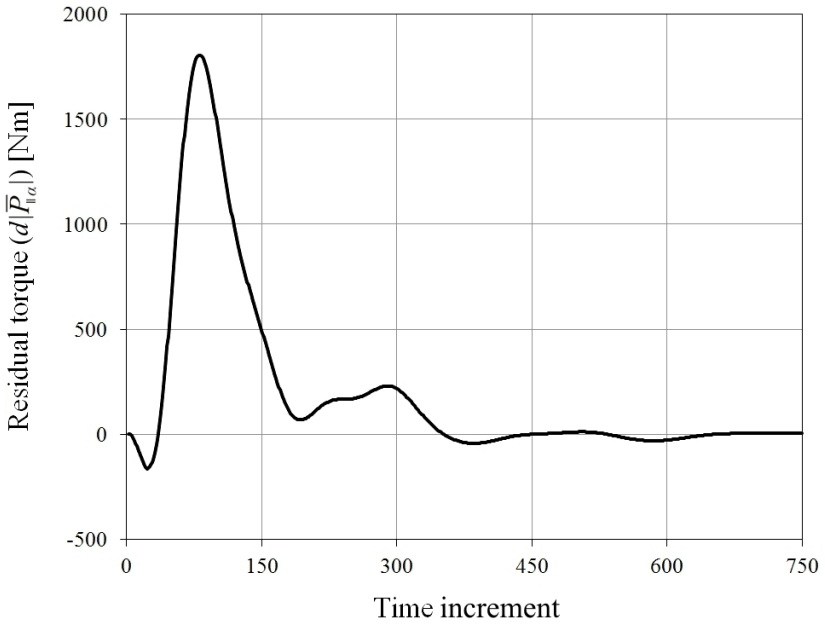


**Figure 3.12:** Time history of the out-of-balance torque $d|\bar{P}_{\|\alpha}|$ around the joint rotational axis

where, $\bar{P}_{\|\alpha}$ can be computed at each time-step as:

$$\bar{P}^t_{\|\alpha} = \bar{P} - \bar{P}^t_{\perp\alpha} \quad ; \quad \bar{P}^t_{\perp\alpha} = \left(\bar{P} \cdot \bar{y}^t_{i_2}\right) \bar{y}^t_{i_2} \tag{3.7}$$

while the arm $d$ at time $t$ can be computed as the shortest distance between two skew lines [Hill, 1994]:

$$d^t = \frac{\left(\bar{p}^t_{i_2} - \bar{p}^t_{i_1}\right) \cdot \left(\bar{P}^t_{\|\alpha} \times \bar{y}^t_{i_2}\right)}{\left|\bar{P}^t_{\|\alpha} \times \bar{y}^t_{i_2}\right|} \tag{3.8}$$

Noting that Eq. (3.8) may provide negative values for $d^t$, depending on the orientation of the $\bar{P}_{\|\alpha}$ vector at time $t$.

According to the described set up, the time history of the out-of-balance torque $d|\bar{P}_{\|\alpha}|$ has been shown in Figure 3.12 as function of the time increment: As it can be seen, Eq. (3.6) is eventually fulfilled at the completion of the analysis.

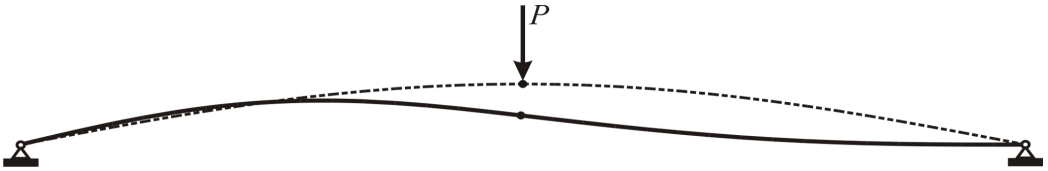


**Figure 3.13:** Shallow arch subjected to a nodal load $P$ applied at the mid-span: The bold line represents the asymmetric buckled shape.

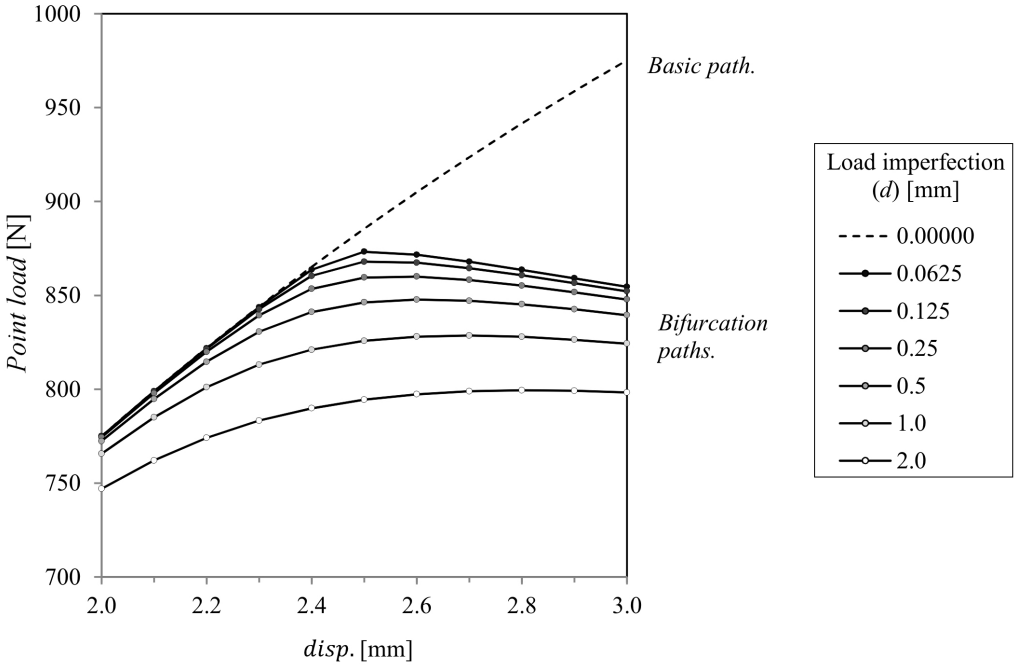


**Figure 3.14:** Bifurcation paths for different imperfection's amplitudes of the pre stressed arch ($c_R = 1$).

## 3.5 Modified co-rotational beam element: validation

### 3.5.1 Elastic buckling of shallow arch

The described modified co-rotational formulation is firstly tested by computing the elastic buckling loads of a shallow arch subjected to an applied nodal load $P$ at the mid-span (see Figure 3.13). The arch geometry is obtained by pre-bending a straight elastic rod. The rod's length ($L$) is 320 mm, with an axial stiffness $EA = 5$ MN and bending stiffness $EI = 10$ Nm$^2$.

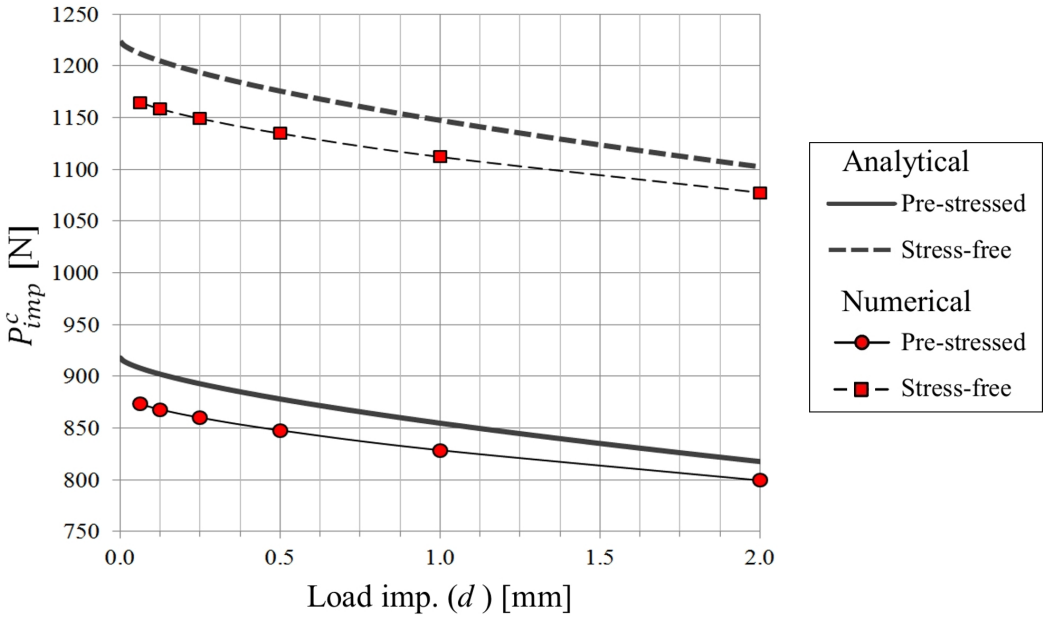


**Figure 3.15:** Comparisons of analytical and numerical buckling loads for different imperfection's amplitudes of the pre stressed and stress free arch.

A preliminary DR analysis was performed to generate the pre-bent configuration, thus obtaining an arch with rise $H = 20.6$ mm and a span of circa 316.5 mm. Two sets of analyses are carried out:

- Pre-stressed configuration: ($c_R = 1$).
- Stress-free configuration: ($c_R = 0$).

For each set of analyses, a *displacement controlled* technique is adopted, by imposing a vertical displacement increment of 0.1 mm to the mid-span node, and allowing the DR routine to reach the corresponding equilibrium configuration, after which, the corresponding vertical reaction force at the midspan node ($R = -P$) is recorded and a further displacement increment is applied.

For each set of analyses, a load imperfection is introduced by offsetting the point load a certain distance ($d$) towards the right of the arch centreline. Such load imperfection is numerically simulated by applying the imposed vertical displacement at the centreline node but adding an applied torque to it as well. The torque's magnitude is set according to the length of the lever arm ($d$) and updated at each DR increment of time ($t + \Delta t$) as a function of the reaction force ($R = -P$) recorded at time $t$. The bifurcation paths, for different amplitudes of imperfection, of the configuration with pre-stress ($c_R = 1$), are reported in Figure 3.14. Accordingly, for each analysis, the maximum recorded $P$ value is assumed to be the elastic buckling load value as reported in Figure 3.15, where a comparison with the corresponding analytical solution is made. The analytical elastic buckling load of pre-stressed and stress-free shallow arches is given by Thompson and Hunt [1983]:

$$\text{Pre-stressed arch} \qquad P^c_{imp.} = \left(\frac{3}{2}\frac{\pi^4 EIH}{L^3}\right)\left[1 - 3.22\left(\frac{d}{L}\right)^{\frac{2}{3}}\right] \tag{3.9}$$

Stress-free arch

$$P^{c}_{imp.} = \left(2\frac{\pi^4 EIH}{L^3}\right)\left[1 - 2.92\left(\frac{d}{L}\right)^{\frac{2}{3}}\right] \tag{3.10}$$

As expected, the numerical buckling load decreases, together with the analytical load, as the imperfection $d$ is increased (see Figure 3.15). The numerical values are consistently lower than the analytical values, with a maximum deviation, for $d = 0.0625$ mm, of circa -3.8% (-47.5 N) for the stress-free arch (and an absolute vertical displacement of 3.1 mm at the buckling point). A max. deviation of -3.8% (-34.9 N) is found for the pre-stressed arch as well, with a vertical displacement of 2.5 mm at the buckling point. Such discrepancy is probably due to the inextentional theory adopted for the derivation of the analytical formulae, leading to buckling load values of shallow arches with infinite axial stiffness. At the buckling point (for $d = 0.0625$ mm) both pre-stressed and stress-free arches were around 0.076% shorter (-0.24 mm). Such (apparently negligible) shortening is consistent with the discrepancy between numerical and analytical buckling loads. In fact, according to Timoshenko and Gere [1961], the influence of axial deformation greatly reduces the buckling load, as the rise/span ratio of the arch is reduced as well.

### 3.5.2 Double layer simply supported beam

In the following example, a double-layer simply supported beam is loaded with a uniformly distributed load $W$ of 50 N/m.

The beam's length ($L$) is 10 m and an elastic modulus $E$ of 10 kN/mm$^2$ is chosen, while a cross-section with $b = h = h_s = 50$ mm is set. Further, a spring (fastener) spacing $s = 100$ mm is considered (see Eq. (2.60)). On this basis, the beam's deflection at the midspan ($\delta$) is analytically computed according to the fol-

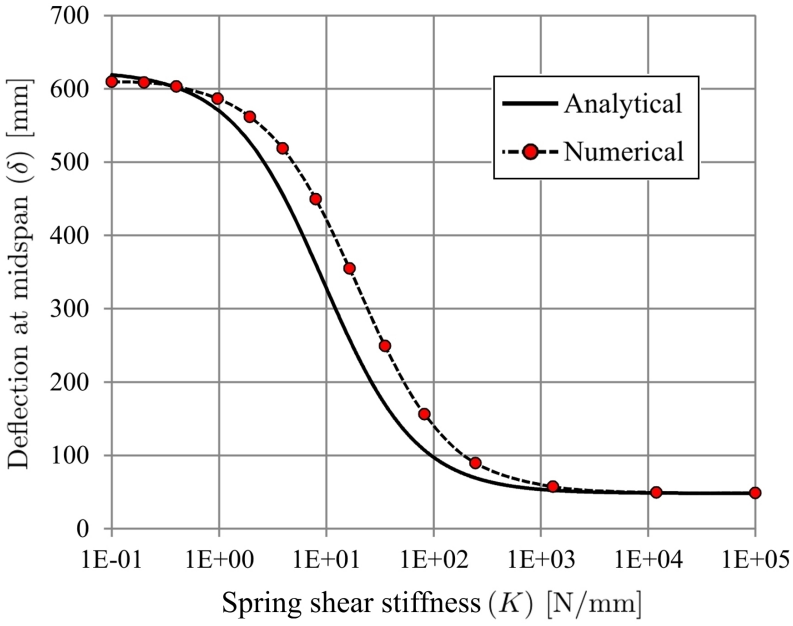


**Figure 3.16:** Simply supported beam: comparison of numerical and analytical outputs of deflection at the midspan as a function of the spring (fastener) stiffness ($K$).

lowing equation provided by Happold and Liddell [1975]:

$$\delta = \frac{WL^4}{\frac{26}{12}b^4E}\left\{\frac{5}{384}+\frac{3}{8\theta}\left[1+\frac{2}{\theta}\left(\frac{1}{cosh\sqrt{\theta}}-1\right)\right]\right\} \quad ; \quad \theta = \frac{26KL^2}{4sb^2E} \tag{3.11}$$

for different values of the shear stiffness of the springs ($K$) varying from $0.1$ to $10^5$ N/mm. In order to numerically compute the beam's deflection, the connection efficiency factor is derived by applying the EC5 Eq. (2.62) according to which: for $K = 0.1 \Rightarrow c_s = 0.0004$ whilst for $K = 10^5 \Rightarrow c_s = 0.997$.

The analytical and numerical outputs of the midspan deflection are compared in Figure 3.16 as a function of the spring stiffness (reported on a logarithmic scale with base 10): As it can be seen, for $1 < K < 1000$, (equivalent to: $0.0039 < c_s < 0.8$) the numerical model shows a much lower bending stiffness compared to the analytical one. This is likely due to the EC5 function in Eq. (2.62), which provides

conservative values for the connection efficiency factor $c_s$.

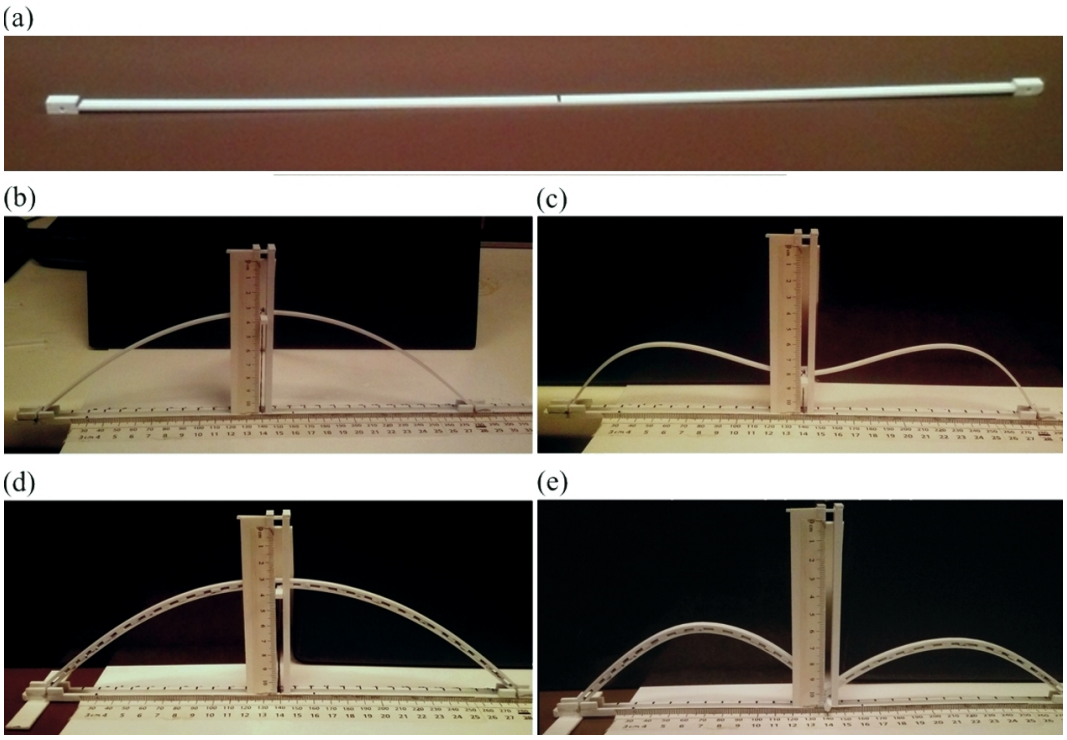


**Figure 3.17:** Experimental test assessing the elastic buckling of a pre-stressed arch made from an initially straight elastic Styrene lath (a); (b) Pre-stressed single-layer arch; (c) Symmetric buckling of the pre-stressed single-layer arch; (d) Pre-stressed double-layer arch; (e) Failure of pre-stressed double-layer arch.

### 3.5.3 Double layer pre-stressed arch

To further assess the effectiveness of the the modified co-rotational formulation for double-layer members (assuming an equivalent $EI$), the load-deflection curves of a single and double-layer pre-stressed arch, subjected to point load $P$ at the midspan, are evaluated by experimental physical test and compared to the corresponding numerical values. The initially straight lath (see Figure 3.17a) is made from Styrene


**Figure 3.18:** Set-up for the experimental test: the load is applied by increments of 2.18 g, by placing nails into a basket hanging underneath the structure and tied to the arch midspan by wire.

(polymer) with a length $L = 320$ mm, cross-section $b \times h$ = 3.97 mm $\times$ 1.48 mm and Young's modulus $E = 2140$ N/mm$^2$, which was assessed by a preliminary tension test carried out according to EN ISO 527-1 guidelines. The resulting arches have a span of 280 mm. Pinned restrains are provided at ends of the arches (see Figure 3.18), thus allowing only rotational degrees of freedom.

It has to be clarified that: the present test is 'only' aimed to assess the geometrically non-linear response but considering a linear-elastic behaviour for the material (Styrene). Furthermore, the output obtained through the small scale test does not aim to 'replicate' or predict the structural behaviour of a full-scale timber arch. Nonetheless, *Dimensional Analysis* [Buckingham, 1914] can be used to

determine the behaviour of a full-scale arch from the small-scale experimental test under description. In particular, considering that the deformation of the arch is 'mainly' function of its bending stiffness, the following relation (derived from [Happold and Liddell, 1975]) can be used for the estimation of the applied load at full scale $P^{full-scale}$:

$$\frac{P^{full-scale}}{P^{scale-model}} = \frac{\left(\frac{EI}{span^3}\right)^{full-scale}}{\left(\frac{EI}{span^3}\right)^{scale-model}} \tag{3.12}$$

whilst, the corresponding displacement at full scale can derived by simple linear scaling:

$$\frac{disp.^{full-scale}}{disp.^{scale-model}} = \frac{span^{full-scale}}{span^{scale-model}} \tag{3.13}$$

A first physical test was carried out on the single *Elastica* arch (Figures 3.17b and 3.17c) thus, assuming the recorded experimental load $P$ as halved the load that would result from a double-layer pre-stressed arch without shear blocks. A second test was then conducted on the double-layer arch (Figures 3.17d; 3.17e) in which, the built-up cross-section was obtained by welding (with Dichloromethane) 32 evenly spaced shear blocks ($h_s = h = 1.48$ mm) on the pre-bent single arch, then, with the lower (pre-bent) lath in place, the upper lath is bent and welded on the shear blocks as well.

Since the end restraints are aligned with the cross-section of the lower lath, the resulting experimental set-up did not perfectly match with the numerical model (where the end restraints are aligned with the barycentre of the double-layer cross-section). Nevertheless, the described set-up faithfully resembled the construction method of a real (actively bent) arch. Lateral and asymmetric buckling were prevented by positioning vertical supports sideways, along the arch centreline, therefore, the displacements were recorded on a metric scale positioned perpendicular

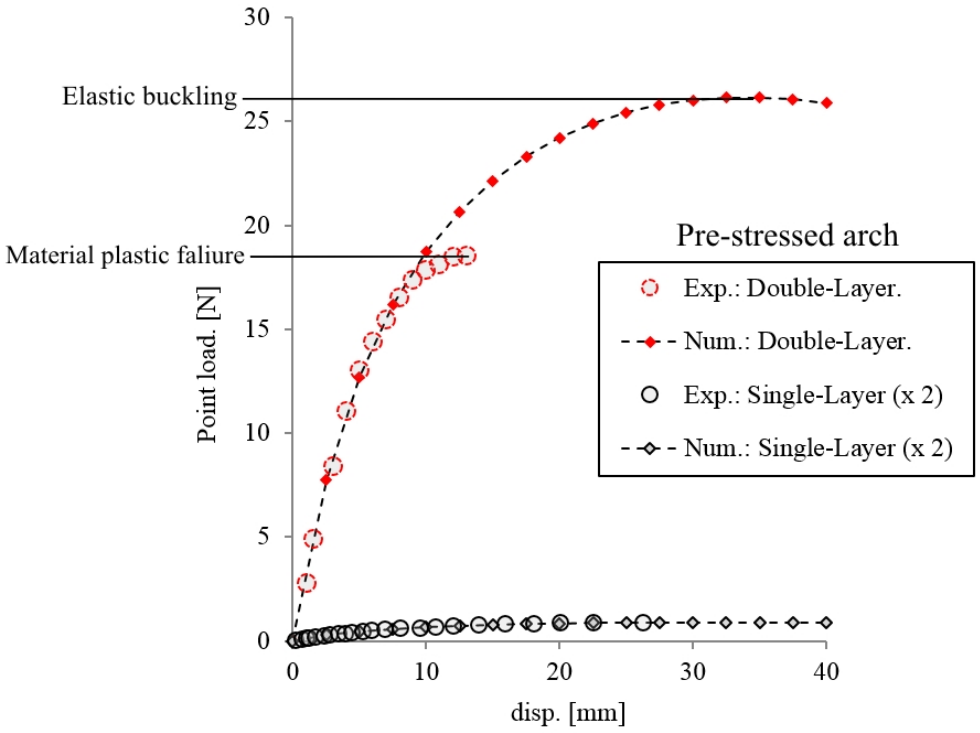


**Figure 3.19:** Comparison of experimental and numerical load-displacement curves.

to the arch. The load was incrementally applied by placing nails (weighing 2.18 g each) into a basket (see Figure 3.18) hanging underneath the structure and tied to the arch midspan by means of wire.

Unlike physical tests, a displacement controlled technique (displacement increment = 2.5 mm) was adopted to numerically trace the load-displacement curves of the double-layer arches over the buckling point. In order to assess the effect of pre-stress forces, two analyses were performed for each shear block configuration, a total of four numerical analyses:

- $K = 0$ ($c_s = 0$) ; Stress-free arch ($c_R = 0$).
- $K = 0$ ($c_s = 0$) ; Pre-stressed arch ($c_R = 1$).
- $K = \infty$ ($c_s = 1$) ; Stress-free arch ($c_R = 0$).

- $K = \infty$ ($c_s = 1$) ; Pre-stressed arch ($c_R = 1$).

As reported in Figure 3.19, the numerical curves are in good agreement with those obtained experimentally, with the exception of the last piece of experimental curve for the double layer arch, where, due to plastic failure of styrene (Figure 3.17e) the experimental load did not reach the elastic buckling value.

As expected, the effect of shear blocks massively increased the buckling load from 2.057 N to 26.440 N (over 1100%). For a better comparison of results, both experimental and numerical curves have been normalized according to the corresponding (numerical) elastic buckling loads $P^c(c_R = 0)$ and reported in Figure 3.20: as it can be seen (Figure 3.20a) the negative effect of residual pre-stress on the buckling load is shown, which reduced of circa $14\%$, thus in agreement with previous investigations [Chini and Wolde-Tinsae, 1988]. Nevertheless, as already pointed out by Mirmiran and Amde [1995], Figure 3.20b shows that the lowering effect of pre-stress forces on the buckling load of double-layer arches, reduced with the increase of the shear blocks stiffness $K$, up to $K = \infty$ ($c_s = 1$) at which point, pre-stress forces have a negligible effect (the buckling load reduction is only 1.12%).

## 3.6 Summary

The work presented in Chapters 2 and 3 aimed to facilitate the design of timber grid-shells, with particular focus on actively bent systems. A numerical framework has been developed to address a range of issues at various design stages, including a viable form-finding procedure involving the use of a reference surface, structural analysis and assembly definitions (of the flat mat geometry) by combining Finite Element procedures with numerical methods typical of computational geometry (mesh manipulation and geometry intersection). The investigations resulted in

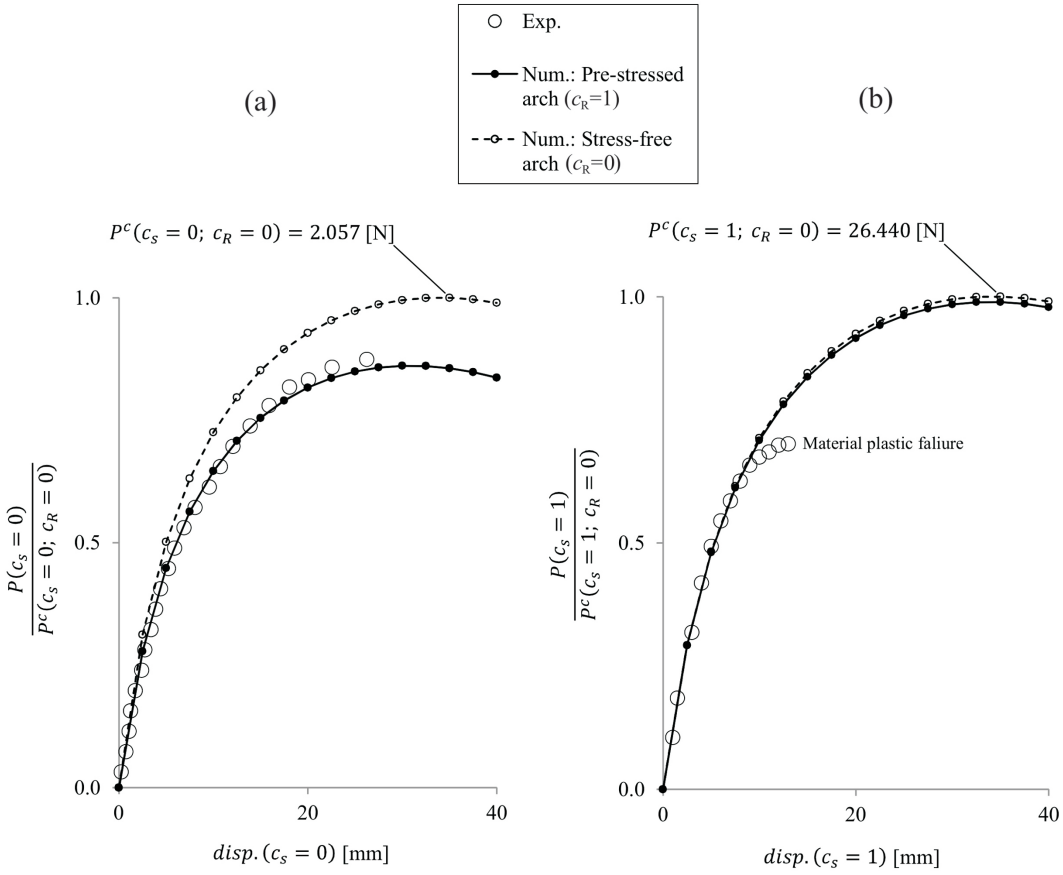


**Figure 3.20:** Comparison of experimental and numerical load-displacement curves: (a) Shear block connection stiffness $K = 0$ ($c_s = 0$); (b) Shear block connection stiffness $K = \infty$ ($c_s = 1$).

the development of a novel single-node model for *large rotations* simulation of cylindrical hinge joints. In addition, a modified version of co-rotational beam-element, allowed for changes of the members' stiffness to be taken into account. The proposed beam-element, and its resolution by Dynamic Relaxation, permitted load analyses in which the increase in stiffness of the built-up timber ribs (for effect of shear block insertion) was taken into account, and at the same time, maintaining the distribution of internal pre-stress and geometry (previously) obtained without

shear blocks.

After preliminary validation tests on simple structural systems, the procedures have been applied to the form-finding, structural analysis and search of the mat's cutting pattern of a grid-shell dome and a corrugated barrel vault. The accompanying numerical tests demonstrated the reliability of the proposed methods, shown by comparing the numerical output against the analytical results of the mid-span deflection of a simply-supported beam, as well as the elastic buckling of a (small scale) pre-stressed arch. The method can be used for geometrically non-linear buckling analyses at completion of the form-finding routine, hence allowing to take into account the effect of pre-stress (and material relaxation) on the final load bearing capacity of the structure.

# Part II

# Cross-sectional Design and Optimisation

# Chapter 4

# Optimisation: theory

As already mentioned in the Introduction, the 'coupled' design problem of sizing of the members' cross-section, of actively bent timber grid-shells, can be addressed in two separate stages, namely: the sizing of the lath's thickness and the sizing of the shear block's thickness. Two optimisation methods have been developed for these, and the present (and next) Chapters have been structured accordingly. In the first Section (4.1) the theoretical aspects, to develop a method to assess the allowable lath's thickness, are illustrated, whilst Section 4.2 addresses the problem of sizing the shear block's thickness, by taking strength and geometric compatibility constraints into account, for the optimisation problem.

## 4.1 Allowable thickness

Clearly, the combined bending, arising from effect of the forming process of double-layer timber grid-shells, generates normal stress which imposes the cross-sectional size, of the single upper/lower laths, to be designed according to a certain domain's limit. In order to design the *allowable* cross-sectional height $h$ of a member subject

to bending moment $M$, the following linear relation can be applied:

$$h_{allowable} = \frac{2I}{M} f_m \tag{4.1}$$

with $f_m$ the material's bending strength. By expressing the bending moment in terms of curvature, Eq. (4.1) becomes:

$$h_{allowable} = \frac{2}{E\kappa} f_m \tag{4.2}$$

with the curvature $\kappa$ measured on the deformed geometry, obtained by assuming an initial guessing value for $h$. Accordingly, Eq. (4.2) states that, the curvature is only function of the assigned boundary displacements. While such an assumption remains valid for small displacements, in case of large displacements, the curvature is function of $h$ as well. In other words, when updating the value of $h$ as from Eq. (4.2), a change of $\kappa$ will occur as well, as a result of the updated bending stiffness of the member. Of course, Eq. (4.2) can be applied iteratively, by considering the updated curvature values at each iteration, up to a point for which the residual error becomes small enough to be neglected. A more detailed description for the suggested iterative approach, is given as follow.

Firstly, the ratios of combined bending stress need to be calculated at completion of the form finding analysis, for the entire element set. According to the Eurocode5 [2008] the following (EC5 6.11 and 6.12) relations apply for combined bending:

$$\frac{\sigma_x}{f_m} + k_m \frac{\sigma_y}{f_m} \leq 1 \quad ; \quad k_m \frac{\sigma_x}{f_m} + \frac{\sigma_y}{f_m} \leq 1 \tag{4.3}$$

therefore by assuming a limit stress ratio $= 1$ and introducing a modification factor ($k_m = 0.7$ for rectangular cross sections [Porteous and Kermani, 2013]) to take into account the effects of variations in material properties and stress redistribution.[1] The bending stress $\sigma_x$ and $\sigma_y$ are computed according to the local system

[1] In fact, timber shows a ductile behaviour under compression, while a brittle failure mode occurs under tension [Bodig and Jayne, 1981].

orientation shown in Figure 2.7:

$$\sigma_x = \frac{h|M_x|}{2I_x} \quad ; \quad \sigma_y = \frac{b|M_y|}{2I_y} \tag{4.4}$$

Noting that, for now we are only interested in assessing the thickness of the single lath, to avoid breakages during the forming process, since, sliding between upper/lower laths is allowed at this stage of the construction. Accordingly, $I_x$ and $I_y$ in Eq. (4.4) relate to the cross-section of the single lath. As already pointed out, the required bending strength/stiffness of the built-up cross-section, in terms of load carrying capacity of the structure, can be provided in a second design stage, by sizing the thickness of the shear blocks (distance between upper/lower laths) which is directly proportional to the moment of area of the built-up cross-section.

Indicating with $\sigma_j^{6.11}$ and $\sigma_j^{6.12}$ the bending stress ratios of the $j$th element as from Eqs. (4.3), we assume that, for a given post-formed geometry, as obtained from the form-finding analysis, the maximum stress ratios $\sigma_{max}^{6.11}$ and $\sigma_{max}^{6.12}$ of the whole element set:

$$\sigma_{max} = max\left\{\sigma_0 \dots \sigma_j \dots \sigma_{n^\circ}\right\} \tag{4.5}$$

can be represented by the values of two functions, whose argument $h$ was set to a certain value $h^{\mathrm{n}}$:

$$g(h^{\mathrm{n}}) = \sigma_{max}^{6.11} \quad ; \quad q(h^{\mathrm{n}}) = \sigma_{max}^{6.12} \tag{4.6}$$

Therefore, our aim is computing the value $h_{allowable}$ of the variable $h$ such that one of the two $g(h^{\mathrm{n}})$ and $q(h^{\mathrm{n}})$ is $\approx 1$ while the other one is less than the unity. Substituting Eqs. (4.4) into Eqs. (4.3) and rearranging, Eqs. (4.6) become:

$$\begin{aligned} g(h) &= max\left(\frac{h|M_x|_j}{2I_x f_m} + k_m \frac{b|M_y|_j}{2I_y f_m} - 1\right) \\ q(h) &= max\left(k_m \frac{h|M_x|_j}{2I_x f_m} + \frac{b|M_y|_j}{2I_y f_m} - 1\right) \end{aligned} \tag{4.7}$$

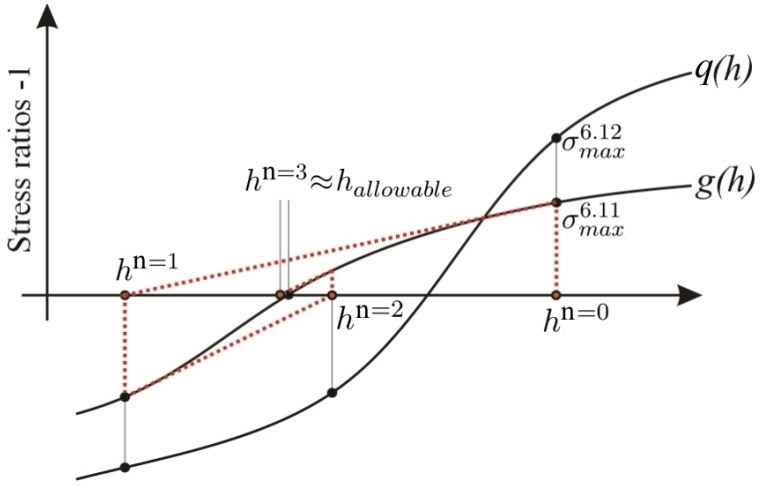


**Figure 4.1:** Newton-Raphson method for computing the allowable lath's thickness.

with $f_m$ a bending strength limit value. Accordingly, the problem is reduced to find the roots of the following system:

$$h_{allowable} = min \begin{cases} h \rightarrow g(h) = 0 \\ h \rightarrow q(h) = 0 \end{cases} \tag{4.8}$$

which can be numerically solved by Newton-Raphson method: expressing the second moments of area in Eqs. (4.7) in terms of $h$ and $b$, the following recurrence equation is obtained:

$$h^{n+1} = min \begin{cases} h^n - \dfrac{g(h^n)}{\left(\dfrac{\partial g}{\partial h^n}\right)} \\ h^n - \dfrac{q(h^n)}{\left(\dfrac{\partial q}{\partial h^n}\right)} \end{cases} =$$

$$= min \begin{cases} max\left[\dfrac{1}{|M_x^n|_j}\left(\dfrac{(h^n)^3 f_m b}{6} - \dfrac{(h^n)^2 k_m |M_y^n|_j}{b}\right)\right] \\ max\left[\dfrac{1}{k_m |M_x^n|_j}\left(\dfrac{(h^n)^3 f_m b}{6} - \dfrac{(h^n)^2 |M_y^n|_j}{b}\right)\right] \end{cases} \tag{4.9}$$

Noting that, the subscript $j$ refers to the generic element's index (see Eq. (2.6)) while the superscript 'n' refers to the nth analysis step (not to be confused with the size $n^{\circ}$ of the element set). A graphical representation of the iterative method is shown in Figure 4.1.

## 4.2 Double-Layer cross-section

Designing the out-of-plane bending stiffness of a grid-shell structure by 'adjusting' the thickness of its members, it can be expected that for a given dominant load combination (e.g. dead load), the stiffness demand will vary among the members. Accordingly, a variable cross-sectional thickness can be sought for the entire system in order to meet the required load-carrying capacity while minimizing the amount of material. On this basis, a *local search* optimisation method for actively bent (double-layer) grid shells is introduced here. The method computes the optimal variable shear block's height $h_s$ such that the bending stress $\sigma$ at the external fibre of the cross-section is 'normalized' to a given $f_m$ value for the entire structure. More precisely, the cross-sectional thickness is proportionally scaled (at each step) according to the linearised field of bending stress ratios $\sigma / f_m$ resulting from a non-linear analysis (DR) with initially constant cross-section. The linearisation error decreases as the number of DR steps increases, up to a point for which, no substantial improvement is appreciated, thus the procedure is stopped.

Clearly, the lower the $f_m$ limit stress is assumed to be, the higher the bending stiffness will result from the optimisation process. As a consequence, for structural systems working mainly in bending action (the simply supported beam as 'extreme' case), an $f_m$ value close to the material limit strength will be chosen. Conversely, for shape-resistant systems working mainly in compression, the choice of the 'uniforming' value ($f_m$) will be mainly dictated by buckling.

### 4.2.1 Single built-up beams

The method for cross-section optimisation introduced here is suitable for the resolution of single-rod systems. Then, an updated procedure for grid shell frameworks, that takes into account additional geometric compatibility constrains, is illustrated in Subsection 4.2.2.

Indicating the vector of design space **h** as:

$$\mathbf{h} = \{h_{s,0} \dots h_{s,j} \dots h_{s,n^\circ}\} \tag{4.10}$$

with $h_{s,j}$ the shear block's thickness of the *j*th beam-element (see Figure 2.7) and $n^\circ + 1$ is the total number of elements of the system, the objective is to find the components of **h** that minimize the deviation of combined bending stresses (at the beam's external fibre) from the uniforming value ($f_m$) and, at the same time, no stress ratio $\sigma / f_m$ is higher than unity. Indicating with $\Sigma$ the resultant of bending stress along the element's domain (from $t = 0$ to $t = 1$):

$$\Sigma = |\Sigma_{x,a}| + |\Sigma_{x,b}| + |\Sigma_y| \tag{4.11}$$

The constrained optimisation problem can be formally stated as:

$$minimize: \quad f(\mathbf{h}) = \sum_{j=0}^{n^\circ} \frac{1}{(n^\circ + 1)} \left| \frac{\Sigma_j}{f_m} - 1 \right| \tag{4.12}$$

$$subject\ to: \begin{cases} \Sigma_j \leq f_m \\ T_{s,j} \leq T_m S \\ h_{s,j} \geq 0 \end{cases} \tag{4.13}$$

The stress terms in Eq. (4.11) are so defined:

$$\Sigma_{x,a} = \int_0^1 \sigma_{x,a}(t)dt = \frac{hE}{2|\bar{p}|}\left[\theta_{x,1} - \theta_{x,2} - (\theta_{x,1}^{eq.} - \theta_{x,2}^{eq.})(1 - c_R)\right] \tag{4.14}$$

$$\Sigma_{x,b} = \int_0^1 \sigma_{x,b}(t)dt = \frac{Ec_s(h + h_s)}{2|\bar{p}|}\left(\theta_{x,1} - \theta_{x,1}^{eq.} - \theta_{x,2} + \theta_{x,2}^{eq.}\right) \tag{4.15}$$

$$\Sigma_{y} = \int_0^1 \sigma_{y}(t)dt = -\frac{bE}{2|\bar{p}|}\left[\theta_{y,1} - \theta_{y,2} - (\theta_{y,1}^{eq.} - \theta_{y,2}^{eq.})(1 - c_R)\right] \tag{4.16}$$

Noting that: since $t$ is a dimensionless parameter, $\Sigma_{x,a}$, $\Sigma_{x,b}$ and $\Sigma_y$ in Eqs. (4.14 to 4.16) are still stress quantities[2] (e.g. N/mm$^2$).

The shear strength constraint in the second of Eqs. (4.13) is introduced to avoid concentrations of horizontal shear $T_s$ exceeding the strength limit value $T_m S$ (see Eq. 2.87 in regard). The minimization of Eq. (4.12) is performed by iteratively running a series of DR steps with updated $\mathbf{h}$ list, until the chosen stopping criteria is satisfied.

Assuming a $h_{s,j}^{\mathrm{n}}$ value for the $j$th element at the DR$^{\mathrm{th}}$ step, the updated $h_{s,j}^{\mathrm{n+1}}$ value to consider for the DR$^{\mathrm{th+1}}$ step is obtained by imposing the following equality:

$$|\Sigma_{x,b}^{\mathrm{n}}|\,(h + h_s^{\mathrm{n}}) = \left(f_m - |\Sigma_{x,a}^{\mathrm{n}}| - |\Sigma_y^{\mathrm{n}}|\right)\left(h + h_s^{\mathrm{n+1}}\right) \tag{4.17}$$

Hence, by taking into account the optimisation constraints in Eqs. (4.13), an $\mathbf{h}^{\mathrm{n+1}}$ list is computed for the entire element set as:

$$\mathbf{h}^{\mathrm{n+1}} = \left\{d_0^{\mathrm{n}} \ldots d_j^{\mathrm{n}} \ldots d_{n^\circ}^{\mathrm{n}}\right\} \tag{4.18}$$

[2] In fact: $\int_0^1 \sigma(t)dt = \sigma(t = 0.5)$.

where:

$$d_j = max \begin{cases} \left[ \dfrac{|\Sigma_{x,b}|\,(h + h_s)}{f_m - |\Sigma_{x,a}| - |\Sigma_y|} - h \right]_j \\ \left( h_s \dfrac{|T_s|}{T_m S} \right)_j \\ 0 \end{cases} \tag{4.19}$$

A flowchart of the described method is shown in Figure 4.2.

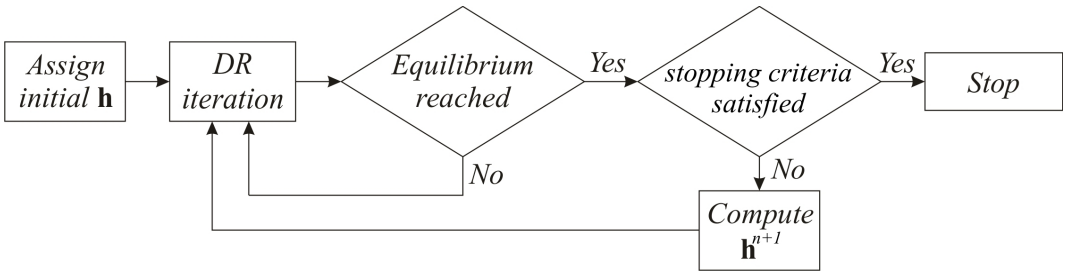


**Figure 4.2:** Flowchart of the method for cross-section optimisation.

### 4.2.2 Two-way grid-shells

For three-dimensional systems, such as two-way grid shells (see Figure 1.11), constructional considerations mean that the thickness of the shear blocks needs to be at least as thick as the single lath's thickness (see Figure 4.3a). Accordingly, the third of Eqs. (4.13) becomes:

$$h_{s,j} \geq h \tag{4.20}$$

consequently, the zero in the third of Eq. (4.19) is replaced with $h$. Additionally, the thickness of the built-up cross-section of ribs in the two different directions need to be equal at the nodal intersection (see Figure 4.3b). Such geometric compatibility results in a further geometric constraint: Indicating with $i$ the generic node index and $u$ and $v$ the two-way grid directions, then the following equality constraint is added to Eqs. (4.13):

$$h^u_{s,i} = h^v_{s,i} \tag{4.21}$$

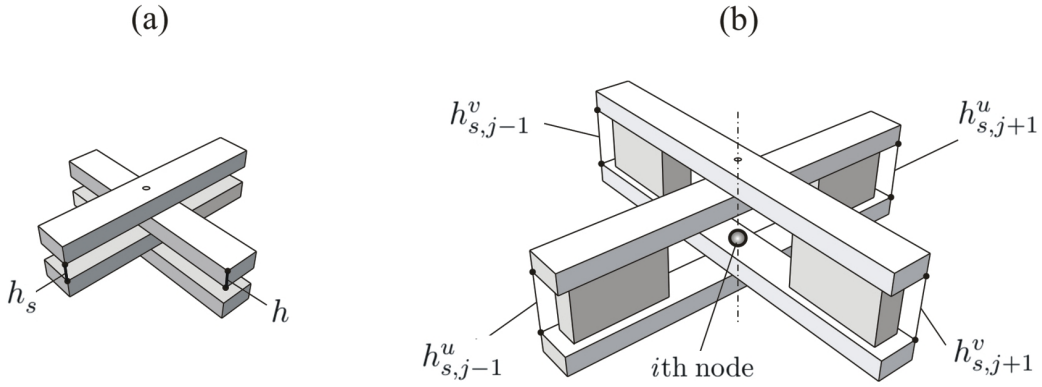


**Figure 4.3:** Geometric compatibility of thickness: (a) $h_s \geq h$; (b) Shear block thickness at the *i*th node as average of the surrounding elements (see Eqs. (4.22)).

Noting that the superscripts $u$ and $v$ refer to the grid's directions (Figure 4.3b) while the superscript $\mathrm{n}$ (e.g in Eqs. (4.17 - 4.18)) refers to the thickness value at the $\mathrm{n}$th DR step. In order to solve the updated optimisation problem in an explicit way, the computing of $\mathbf{h}^{\mathrm{n}+1}$ for a two-way grid shell system is performed (as before) according to Eqs. (4.18 - 4.19) but, in order to assure geometric compatibility imposed by Eq. (4.21), an additional operation is performed (at each DR step) on the $\mathbf{h}^{\mathrm{n}+1}$ list resulting from Eq. (4.18).

The additional operation to perform on the $\mathbf{h}^{\mathrm{n}+1}$ list (as from Eq. (4.18)) to assure geometric compatibility, is described as follows: Firstly, an average $h_{s,i}$ value, for the *i*th node, is computed as a function of the shear blocks thickness of the surrounding elements belonging to the $u$ and $v$ directions. With reference to Figure 4.3b:

$$h^u_{s,i} = \frac{h^u_{s,j-1} + h^u_{s,j+1}}{2} \quad ; \quad h^v_{s,i} = \frac{h^v_{s,j-1} + h^v_{s,j+1}}{2} \tag{4.22}$$

Noting that the subscript $i$ refers to the thickness $h_s$ interpolated at the $i$th node while the subscript $j$ refers to the (constant) thickness value $h_s$ of the $j$th element. In other words, $h_s$ is assumed to vary 'linearly' along the element. Accordingly,

for each $i$ node there will be two thickness values, each one interpolated according to the grid direction ($u$, $v$). By taking, for the $i$th node, the maximum value:

$$h_{s,i}^{max} = max\left\{h_{s,i}^{u}; h_{s,i}^{v}\right\} \tag{4.23}$$

and writing the linear (thickness) variation law along the *j*th element:

$$\begin{aligned} h_s^u(t) &= (h_{s,i_2}^u - h_{s,i_1}^u)t + h_{s,i_1}^u \\ h_s^v(t) &= (h_{s,i_2}^v - h_{s,i_1}^v)t + h_{s,i_1}^v \end{aligned} \quad ; \quad t \in [0,1] \tag{4.24}$$

the difference in values between $h_s$ as from the Eq. (4.18) and $h_s(t = 0.5)$ as from Eqs. (4.24) is measured:

$$\begin{aligned} h_s^u - \left[(h_{s,i_2}^u - h_{s,i_1}^u)0.5 + h_{s,i_1}^u\right] \\ h_s^v - \left[(h_{s,i_2}^v - h_{s,i_1}^v)0.5 + h_{s,i_1}^v\right] \end{aligned} \tag{4.25}$$

thus: the linear thickness variation law is updated this time by considering, for each element's end, the maximum value $h_{s,i}^{max}$ as from Eq. (4.23). Accordingly, Eqs. (4.24) become:

$$\begin{aligned} h_s^u(t) &= (h_{s,i_2}^{max} - h_{s,i_1}^{max})t + h_{s,i_1}^{max} \\ h_s^v(t) &= (h_{s,i_2}^{max} - h_{s,i_1}^{max})t + h_{s,i_1}^{max} \end{aligned} \tag{4.26}$$

The new 'constant' $h_s^*$ value for the *j*th element is obtained by setting $t = 0.5$ in Eqs. (4.26) and adding them up to the quantities in (4.25) hence, obtaining the following general equation:

$$h_s^* = h_s + \frac{1}{2}\left(h_{s,i_2}^{max} - h_{s,i_1}^{max} - h_{s,i_2} + h_{s,i_1}\right) + h_{s,i_1}^{max} - h_{s,i_1} \tag{4.27}$$

in which $h_s$ is that obtained by Eq. (4.18). As it can be seen: for $h_{s,i_1} = h_{s,i_1}^{max}$ and $h_{s,i_2} = h_{s,i_2}^{max} \Rightarrow h_s^*$ and $h_s$ are equal, therefore, the consistency between 'constant' and 'linear' models, of thickness along the element, is held.

It is important here to note that: an average value between $h^u_{s,i}$ and $h^v_{s,i}$ in replacement of $h^{max}_{s,i}$ in Eq. (4.23), would allow for a greater minimization of the objective function as stated in Eq. (4.12). Nevertheless, by considering $h^{max}_{s,i}$ makes it possible to fulfil the strength (optimisation) constraint stated in the first of Eqs. (4.13) according to which, no bending stress ratios higher than unity must occur. For single-rod systems, such strength constraint is 'implicitly' fulfilled by Eqs. (4.19).

## 4.3 Summary

A method for optimisation of the cross-section of actively bent grid-shells was described in the present Chapter. Thanks to the adopted double-layer technique, it was possible to 'decompose' the optimisation problem in two sub-problems: Sizing of the thickness of single upper/lower laths, according to a desired curved shape, and sizing of the thickness of the shear blocks, according to a given (dominant) load distribution. The described methods have been tested by experimental and numerical tests, hence introduced in the following Chapter.

# Chapter 5

# Optimisation: validation and results

## 5.1 Allowable thickness: validation

The theory for sizing of the laths, has been applied to a practical application, regarding the construction of a full-scale prototype: the Toledo 2.0 (see Figure 5.1), a post-formed, two-way, timber grid-shell, the most recent of a series of 13 similar structures, built and designed by *gridshell.it*, a research group led by Sergio Pone, professor of architectural technology at the University of Naples Federico II. A description of the construction phases and their simulation by the six DoF DR method (see Chapter 2) is described in here, together with a report on the application of the method for cross-sectional sizing detailed in Section 4.1.

A further investigation was carried out in regard to the corrugated barrel vault described in Section 3.3 by finding a geometry for the two-way grid-shell, but this time, with variable edge-length, in order to minimize the bending stresses induced by the forming process, hence allowing for a 'thicker' lath's cross-section.

**Figure 5.1:** Toledo timber gridshell 2.0. Completed structure (Photos courtesy - Daniele Lancia).

### 5.1.1 Full scale prototype

The construction process of the Toledo 2.0 is based on the'up-ward' method. As for the Multihall in Mannheim, [Happold and Liddell, 1975] the flat mat was first assembled on ground and then forced to reach its final shape by means of ad-hoc machineries: As shown in Figures 5.2 and 5.3, eight central nodes of the grid-shell were pulled up through a system made of pulleys placed on top of a scaffolding tower (placed at the centre of the flat grid) together with four cables for nautical use and four hand hoists. The grid was pulled up to a point for which the bracing system of the scaffolding tower, interfering with the grid, could not be avoided any further. At this stage, the interfering braces were temporary removed and reassembled in a new position underneath the grid. Once the final height of the grid-shell was reached, two extra cross cables and hoists were added at the external nodes to provide horizontal trust, thus allowing to reach the desired shape (see Figures 5.2f and 5.3d). It is to be noted that the scaffolding tower assured safe working conditions during the whole erection process, by preventing sudden collapse of the grid — for example due to unexpected breakage of a cable — and also allowing to conduct most of the operations from outside the grid footprint.

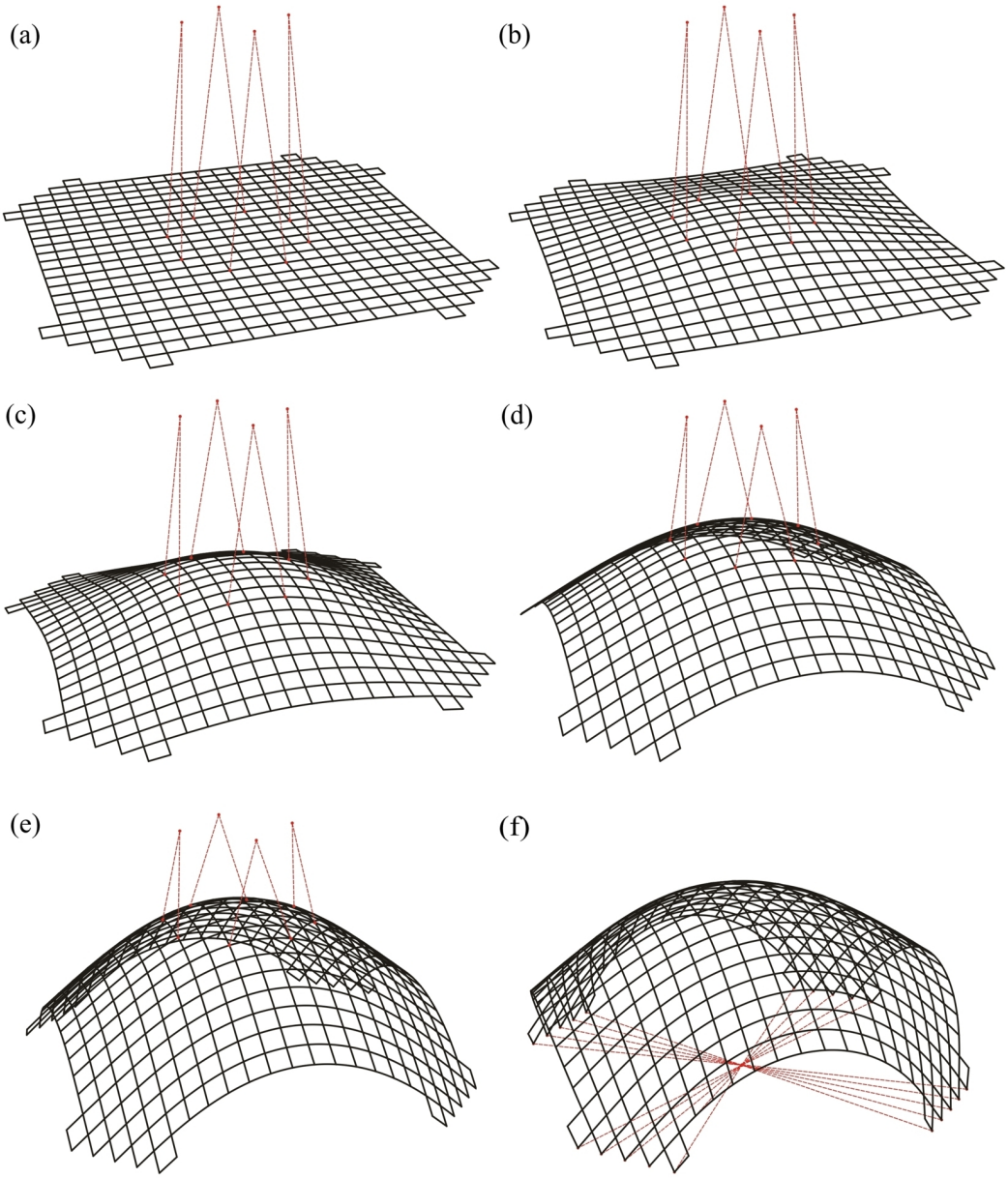


**Figure 5.2:** Toledo gridshell 2.0 in Naples, Italy 2014. Simulation of the forming process by DR: (a - e) The corner nodes are restrained on rollers while the central nodes are pulled up by pre-stressed cable-elements; (f) The cable-elements are 'disabled' from the analysis and additional horizontal trust is added to the corner nodes by means of pre-stressed cables.

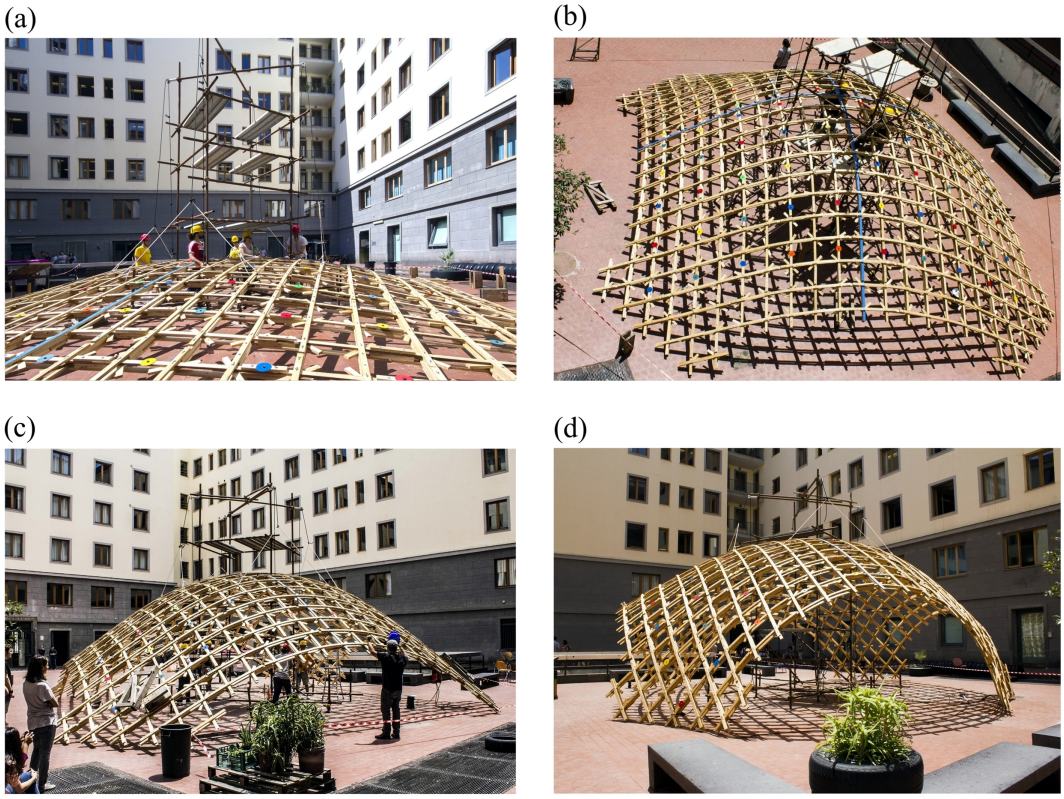


**Figure 5.3:** Toledo gridshell 2.0. Construction process: (a - c) The central nodes are pulled up by means of cables; (d) Additional horizontal trust is added to the corner nodes in order to reach the final shape.

With the Toledo 2.0 there also been the opportunity to experiment a new bracing system. A series of 'sticks' and 'diagonals' were prefabricated and assembled at each second quadrangles of the grid. Short timber sticks were assembled at the nodal connections as a further layer (in addition to the 'usual' four) between the second and third layer (see Figure 5.4). The diagonals were then lined-up to the second and fourth layer, hence resembling a cross in-between some of the quadrangles (Figure 5.4b) eventually obtaining a chessboard-like pattern. If one brace had been fitted on the total amount of quadrangles, it would have presumably required the same (total) amount of material. Nevertheless, by having two braces

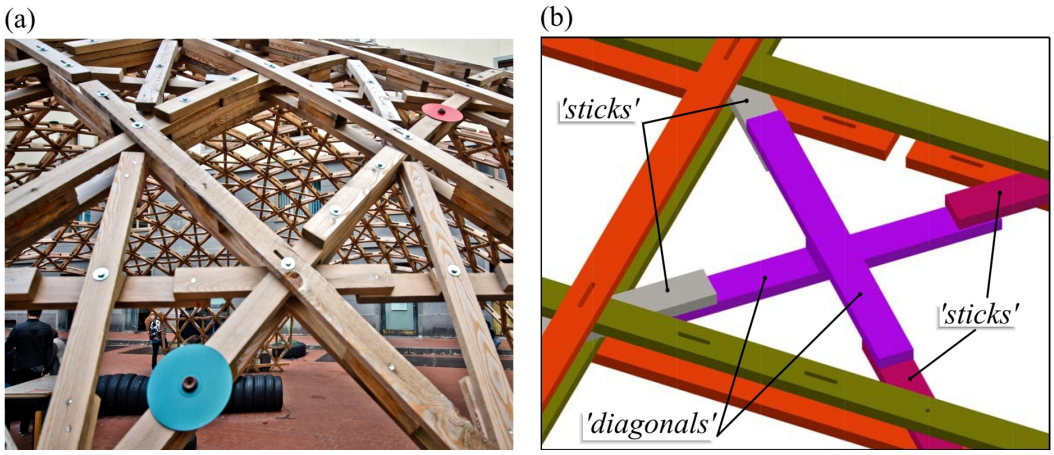


**Figure 5.4:** Toledo gridshell 2.0. Bracing system: (a) Construction detail; (b) Detail of the joint between sticks and diagonals.

crossing each other, with a fastener at their intersection, allowed to reduce the *effective length* of elastic bucking, thus obtaining a theoretical buckling load (of the brace under compression force) four time higher than the one obtainable with a single brace of equal cross-section. Unlike for the flat geometry, each brace has different length in the formed grid-shell. The numerical model was used to post-rationalise the geometry of the bracing system by grouping the diagonals into (only) five length-types. This assured an overlapping distance (between sticks and diagonals) ranging from 70 to 120 mm.

The method described in Section 4.1 was applied in relation to the design of the Toledo 2.0 grid-shell. Bending strength ($f_m$) and elastic modulus ($E$) were set in accordance to preliminary experimental investigations on the same white spruce timber, supplied for the realization of the Toledo gridshell 1.0 (see [Pone et al., 2013]). The value of $f_m$ to consider in Eq. (4.9) was obtained by preliminary tests on small, clear specimens, carried out in accordance to BS-EN-408 [2012] guidelines (see Figure 5.5). A brief report of the experimental campaign is provided by Pone

et al. [2013] and reported as follows.

### 5.1.2 Characterization of the bending strength

A total number of:

- 20 monotonic compression tests parallel to the grain
- 20 monotonic compression tests orthogonal to the grain
- 10 four-point bending

were performed. The nominal geometry of the coupon specimens for the compression tests was: 20 mm x 20 mm x 50 mm, while a nominal geometry of 20 mm x 20 mm x 360 mm was considered for the bending test specimens (see Figure 5.5). The compression test results are summarised in in Table 5.1 in terms of mean compression strength, both parallel and orthogonal to the grain ($f_{c,0,mean}$ and $f_{c,90,mean}$ respectively) as well as the mean specific weight ($\rho_{mean}$). In Table 5.2 instead, are reported the test results of peak bending moment ($M_u$), section modulus ($W = 2I_x/h$) and ultimate bending strength ($f_{m,u}$).

Although the mean density experimentally found ($\rho_{mean} = 380.2$ kg/m$^3$) is very close to the reference value of a C18 timber grade:[1] a larger scatter was recognised between the compression strength parallel-to-grain at 0.05 percentile experimentally found ($f_{c,0,05}$ = 23.83 N/mm$^2$) and the corresponding C18 characteristic value provided by BS-EN-338 ($f_{c,0,k}$ = 18 N/mm$^2$).

According to the following relation given in Annex A of BS-EN-338:

$$f_{c,0,k} = 5(f_{m,k})^{0.45} \tag{5.1}$$

[1] According to BS-EN-338 strength grading standard, for a C18 timber grade: $\rho_{mean} = 380$ kg/m$^3$.

**Table 5.1:** Compression tests & specific weight results [Pone et al., 2013].

| Number of specimens | $f_{c,0,mean}$ [N/mm$^2$] | $f_{c,90,mean}$ [N/mm$^2$] | $\rho_{mean}$ [kg/m$^3$] | $\rho_{st.dev.}$ [kg/m$^3$] | $\frac{\rho_{st.dev.}}{\rho_{mean}}$ |
|---|---|---|---|---|---|
| 20 | 26.274 | — | 380.2 | 34.26 | 8.97% |
| 20 | — | 3.488 | | | |

**Table 5.2:** Four-point bending test results [Pone et al., 2013].

| Specimen [ID] | $M_u$ [Nmm] | $W$ [mm$^3$] | $f_{m,u}$ [N/mm$^2$] |
|---|---|---|---|
| 1 | 53100.0 | 1334.538 | 39.789 |
| 2 | 55302.0 | 1323.277 | 41.791 |
| 3 | 58548.0 | 1316.708 | 44.465 |
| 4 | 61830.0 | 1299.523 | 47.579 |
| 5 | 62010.0 | 1238.828 | 50.055 |
| 6 | 77322.0 | 1355.418 | 57.046 |
| 7 | 50760.0 | 1363.490 | 37.228 |
| 8 | 59448.0 | 1280.050 | 46.441 |
| 9 | 63252.0 | 1367.683 | 46.247 |
| 10 | 75288.0 | 1342.621 | 56.075 |
| Mean value | 61686.0 | 1322.213 | 46.671 |
| St. Dev. | 8697.2 | 40.441 | 6.444 |
| St. Dev. / Mean value | 14.09% | 3.06% | 13.81% |

the characteristic bending strength can be obtained as function of the characteristic compression strength parallel to the grain. Therefore: for $f_{c,0,k} = f_{c,0,05} = 23.83$

N/mm$^2$ in the *inverse* of Eq. (5.1):

$$f_{m,k} = 0.028(f_{c,0,k})^{2.2...} \tag{5.2}$$

then a $f_{m,k}$ = 32.13 N/mm$^2$ is obtained. As a further check, it can be seen from Table 5.2 that the minimum $f_{m,u}$ experimentally found is in any case higher than the $f_{m,k}$ provided by Eq. (5.2). A rounded value of $f_m$ = 32 N/mm$^2$ to be set in Eq. (4.9) was considered.

Since the bending strength so obtained was referring to clear (defect-free) specimens, a visual inspection of the whole laths supply was carried out, in order make sure that 'defect-free' lath specimens were paced in correspondence of those regions of the flat mat where higher curvatures were expected to occur.

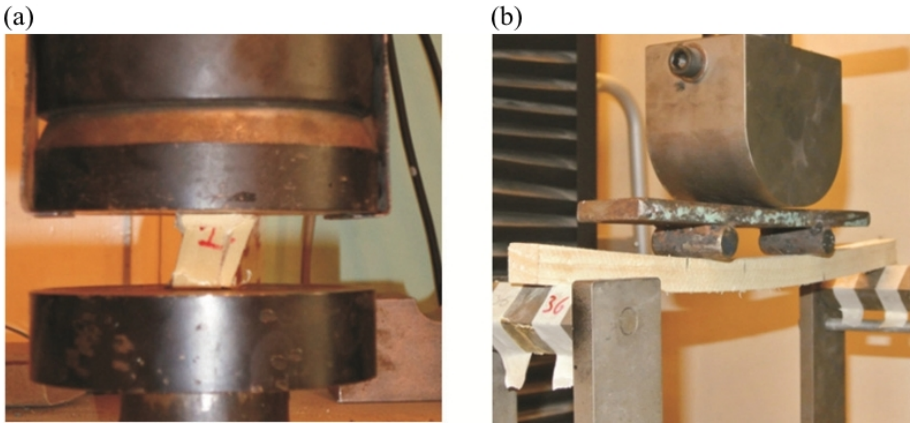


**Figure 5.5:** Experimental campaign [Pone et al., 2013]: (a) compression tests; (b) four-point bending test.

### 5.1.3 Numerical results

At completion of the forming process simulation, as shown in Figure 5.2, pinned restrains were added to the corner nodes and the iterative procedure for finding of the allowable thickness was performed. The moment reactions $M_x$ and $M_y$ needed

for the calculation of the stress ratios (Eqs. (4.3)) were derived at the centroid of each element by applying the moment-curvature relations:

$$M_x = \kappa_x E I_x \quad ; \quad M_y = \kappa_y E I_y \tag{5.3}$$

with the curvature values $\kappa_x$ and $\kappa_y$ obtained from the element's shape function (Eqs. (2.74)).

A report of the iterative process is given in Table 5.3: as it can be seen, despite an 'exaggerated' initial guessing value of 100 mm, chosen for the lath's thickness, after only three iterations, the method provided an allowable value for $h = 25.76$ mm, corresponding to a maximum stress ratio of 1.0 with an order of accuracy up to the second decimal place. This suggests that the residual forces, arising for effect of the change in thickness (when passing from the analysis step n to the analysis step n+1) are so small that a single step may be enough to computing a 'reasonable' accurate value for the allowable thickness $h$: Inserting Eqs. (5.3) into Eqs. (4.3 -4.4): Eq. (4.9) can be rewritten in terms of curvature values as:

$$h_{allowable} = min \begin{cases} max \left[ \dfrac{1}{|\kappa_x|_j} \left( \dfrac{2 f_m}{E} - k_m b |\kappa_y|_j \right) \right] \\ max \left[ \dfrac{1}{k_m |\kappa_x|_j} \left( \dfrac{2 f_m}{E} - b |\kappa_y|_j \right) \right] \end{cases} \tag{5.4}$$

### 5.1.4 Stress minimization

A further numerical investigation has been carried out to evaluate, for a given reference surface, such as the corrugated barrel vault used in Section 3.3, an alternative grid geometry in order to reduce the bending stress induced by the forming process, hence allowing for higher values of the allowable lath's thickness.

In order to reduce the normal stress ($\sigma_y$) due to lateral bending, a fictitious axial stiffness value in the first step of the form-finding, analysis may be used: The

**Table 5.3:** Summary of the iterative method for computing of the allowable lath's thickness.

| Analysis Step | Lath's thickness ($h$) [mm] | Max. bending stress ratios[a] | |
|---|---|---|---|
| | | $\sigma_{max}^{6.11}$ | $\sigma_{max}^{6.12}$ |
| 1st | 100.00 | 3.03 | 2.32 |
| 2nd | 26.34 | 1.01 | 0.94 |
| 3rd | 25.76 | 1.00 | 0.94 |
| 4th | 25.68 | 1.00 | 0.94 |

[a]based on Eqs. (4.7)

real stiffness term $EA$ is multiplied by a reducing factor $\in [0, 1]$ at the first DR analysis step, thus the resulting length of the deformed elements is then assumed as *unstressed length value* in the second analysis step, together with the real axial stiffness, eventually coming up to a mesh with all the edges having different length.[2] For instance, assuming a reducing factor $\approx 0.0$ would lead to geodesic paths, with null bending around the laths stronger axis ($\kappa_y \approx 0.0$) nonetheless the assembling of the corresponding flat mat could not be feasible (the curvature reduction at formed geometry is recovered with opposite sign in the flat geometry). A compromise therefore is to calibrate the scaling factor such that the corresponding bending stress ratios $\sigma_{max}^{6.11}$; $\sigma_{max}^{6.12}$ are below the unity for both (flat/bent) configurations.

With reference to the barrel vault previously described: Starting with a mesh of uniform edge length = 1 mm, a variable length ranging from 580 mm to 1130 mm is found, with a mean value of 980 mm. The corresponding reduction of the stress ratios is: $\sigma_{max}^{6.11} = -22.9\%$ and $\sigma_{max}^{6.12} = -27.6\%$. In figure 5.6 the two geometries

[2]The resulting variable distance between connection's holes in the timber specimens may be handled via (CNC) drilling machinery.

for both flat and formed configuration are reported. The resulting stress ratios at flat configuration for the effect of the variable length, resulted in: $\sigma_{max}^{6.11} = 53.3\%$; $\sigma_{max}^{6.12} = 76.2\%$ thus below the limit ratio. Lastly, as a consequence of the reduction of bending stress ratios, an increase of the allowable cross sectional height of up to 50 mm is found. Further investigations are certainly required to assess the feasibility of bending timber laths 'meanwhile' assembling the flat mat.

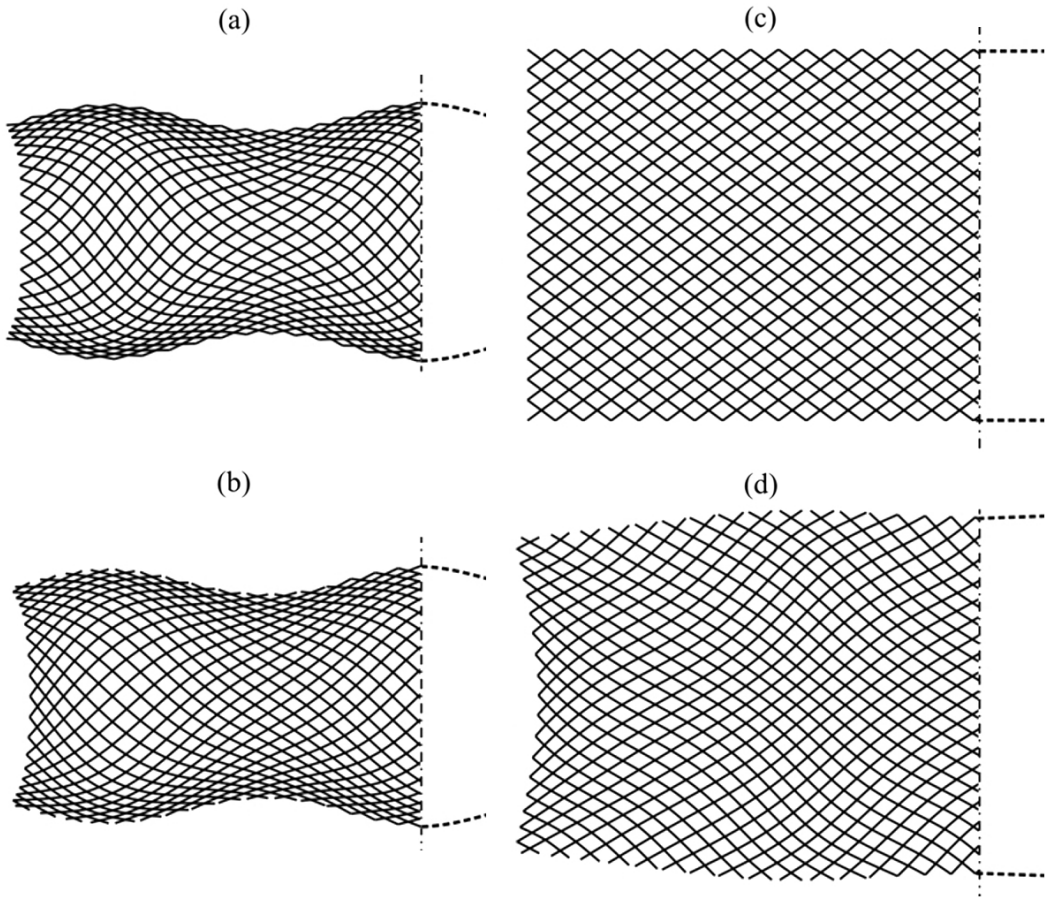


**Figure 5.6:** Corrugated barrel vault: (a) Constant length, formed configuration; (b) Variable length, formed configuration; (c) Constant length, flat configuration; (d) Variable length, flat configuration.

## 5.2 Double-Layer cross-section: Results

The theory described in Section 4.2, for the cross-section optimisation of the built-up members, has been implemented and tested for the simple case of a simply-supported beam and a grid-shell framework. The set-up and results of the numerical tests are reported in the following Subsections.

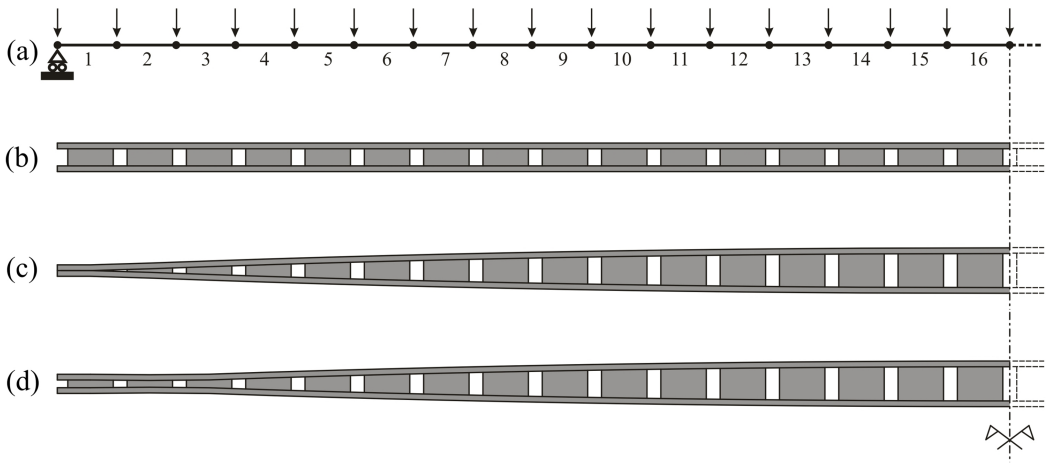


**Figure 5.7:** Simply supported beam: (a) Static scheme; (b) Initial cross-section; (c) Optimized cross-section for $T_m S = 40$ kN; (d) Optimized cross-section for $T_m S = 20$ kN.

### 5.2.1 Simply supported beam

A $10$ m long beam, subjected to a uniformly distributed load of $1$ kN/m, is selected for the first analysis test. The static scheme of the system is shown in Figure 5.7a. The rectangular cross-section of the single lath is $b = 80$ mm and $h = 30$ mm, while a constant shear blocks thickness $h_s = 90$ mm is initially assumed.

The elastic modulus $E$ is set to 10 kN/mm$^2$. Since the numerical investigation is conducted on a straight beam, the value of $c_R$ does not affect the solution and is

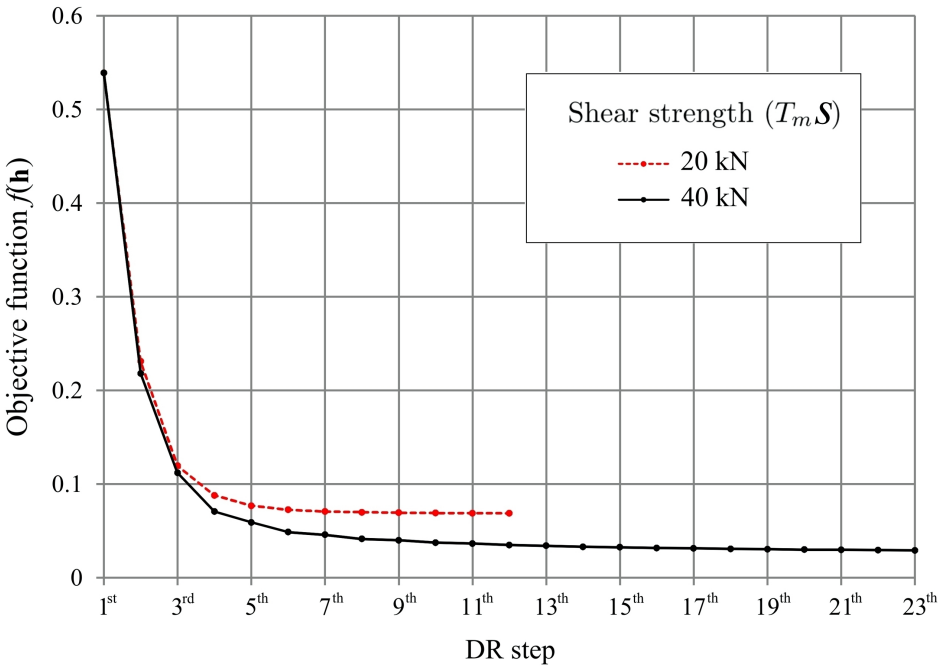


**Figure 5.8:** Simply supported beam: Optimisation's history for two different values of the strength constrain $T_m S$. The objective function $f(\mathbf{h})$ is computed according to Eq. (4.12).

thus neglected, while, a connection efficiency factor $c_s = 1$ and a stress limit value $f_m = 28$ N/mm$^2$ are assumed. The beam is discretised into 32 elements of uniform length.

The optimisation method was run twice, assuming shear strength limits $T_m S =$ 40 kN and 20 kN respectively (see Figure 5.8). Both analyses were stopped when: $max\{|h_{s,j}^{n+1} - h_{s,j}^{n}|\} \leq 2$ mm. The initial and optimized beam profiles obtained with $T_m S = 40$ kN and $T_m S = 20$ kN are shown in Figures 5.7c and 5.7d respectively, while in Table 5.4 the stress ratio $\Sigma / f_m$ and the shear reaction $T_s$ are reported according to the element index (as reported in Figure 5.7a).

As can be seen in the third and fourth columns of Table 5.4, the bending stress ratios of the optimised beam are all unitary, with the exception of those in prox-

imity of the beam supports as a consequence of the geometric and shear strength constraints (second and third of Eq. (4.13) respectively). As one would expect, in the fifth column of the same table, it can be seen that the beam with constant cross-sectional height experiences a maximum horizontal shear reaction at the supports (left node of element 1) which decreases linearly up to zero at the beam midspan (right node of element 16).

It is worth noting also that the reduced shear strength parameter $T_m S = 20$ kN, used to generate the values in the seventh column of Table 5.4, resulted in a beam with thicker cross-section at its end supports, as shown in Figure 5.7d in comparison to the one obtained by $T_m S = 40$ kN (Figure 5.7c).

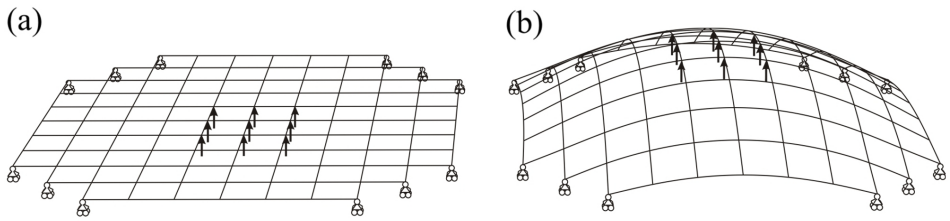


**Figure 5.9:** Grid shell System: (a) Initial flat mat; (b) post formed shape.

### 5.2.2 Grid-shell system

The optimisation method is further tested on a simple grid shell system obtained by the preliminary bending of a flat mat geometry as shown in Figure 5.9. The initial two-way mat is made out of straight elastic rods evenly spaced at a distance of 2 m.

Then, an anti-gravitational load is applied at the central nodes, while the boundary nodes at the mat's corners are constrained to translate in the horizontal plane. Then, in a second preliminary step, the rollers at the supports are substituted by pinned restraints and the anti-gravitational load is removed, thus allowing the post

**Table 5.4:** Simply supported beam: Comparisons, between the initial and optimized cross-section, in terms of bending stress ratios and shear reactions.

| Cross-section: | Constant | Optimized | | Constant | Optimized | |
|---|---|---|---|---|---|---|
| $f_m$ [N/mm$^2$] | 28 | 28 | 28 | | 28 | 28 |
| $T_m S$ [kN] | | 40 | 20 | | 40 | 20 |
| Elem. index[a] | Bending stress ratio ($\Sigma / f_m$) | | | Shear reaction ($T_s$ [kN]) | | |
| 1 | 0.120 | 0.562 | 0.218 | 12.0 | 37.4 | 20.0 |
| 2 | 0.336 | 0.991 | 0.685 | 11.3 | 25.1 | 20.0 |
| 3 | 0.538 | 0.999 | 0.998 | 10.5 | 16.9 | 17.3 |
| 4 | 0.725 | 0.999 | 1.001 | 9.7 | 12.7 | 12.7 |
| 5 | 0.898 | 0.999 | 1.000 | 9.0 | 9.9 | 9.9 |
| 6 | 1.058 | 0.999 | 1.000 | 8.2 | 7.9 | 7.9 |
| 7 | 1.202 | 0.999 | 1.000 | 7.4 | 6.4 | 6.4 |
| 8 | 1.333 | 1.000 | 1.000 | 6.7 | 5.2 | 5.2 |
| 9 | 1.450 | 1.000 | 1.000 | 5.9 | 4.3 | 4.3 |
| 10 | 1.552 | 1.000 | 1.000 | 5.1 | 3.5 | 3.5 |
| 11 | 1.640 | 1.000 | 1.000 | 4.4 | 2.8 | 2.8 |
| 12 | 1.713 | 1.000 | 1.000 | 3.6 | 2.2 | 2.2 |
| 13 | 1.771 | 1.000 | 1.000 | 2.8 | 1.7 | 1.7 |
| 14 | 1.816 | 1.000 | 1.000 | 2.0 | 1.2 | 1.2 |
| 15 | 1.845 | 1.000 | 1.000 | 1.2 | 0.7 | 0.7 |
| 16 | 1.860 | 1.000 | 1.000 | 0.4 | 0.2 | 0.2 |

[a]as shown in Figure 5.7.

formed grid shell to settle in its final configuration. The resulting geometry has a size of 18.7 m $\times$ 18.7 m in plan and an elevation of 4.25 m (see Figure 5.9b). On the equilibrium geometry so found, a connection efficiency factor $c_s = 1$ and a $c_R$ factor $= 0$ (Stress-free geometry) are set.

A gravitational load of 2 kN per node is considered for the optimisation process. The initial cross-sectional geometry (with constant $h_s$) is set in accordance with

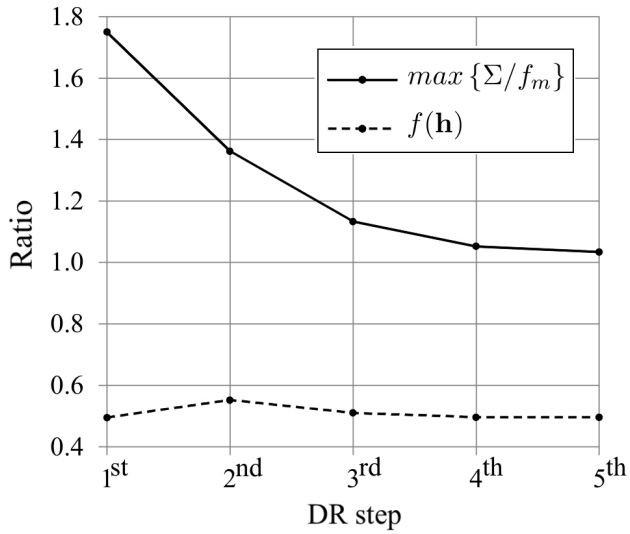


**Figure 5.10:** Grid shell System: Optimisation history in terms of maximum bending stress ratio $\Sigma/f_m$ and average stress ratio $f(\mathbf{h})$ as expressed in Eq. (4.12).

the previously described test on the simply-supported beam (see Figure 5.11a) as well as the Young's modulus. In addition, a shear modulus $G = 700$ N/mm$^2$ and a $f_m$ value of 8 N/mm$^2$ are considered. As for the simply-supported beam, the convergence criterion was set according to: $max\{|h_{s,j}^{n+1} - h_{s,j}^{n}|\} \leq 2$ mm.

As can be seen from Figure 5.10, after five DR steps, the average stress ratio $f(\mathbf{h})$ of Eq. (4.12) does not experience any minimization but maintains a steady value of circa 0.5. Nonetheless, the maximum bending stress ratio $\Sigma/f_m$ converges to unity, dropping from 1.8 (at completion of the first DR step) to 1.03 (at completion of the fifth DR step) therefore fulfilling the optimisation constraint stated in the first of Eqs. (4.13). The optimized geometry is shown in Figure 5.11b.

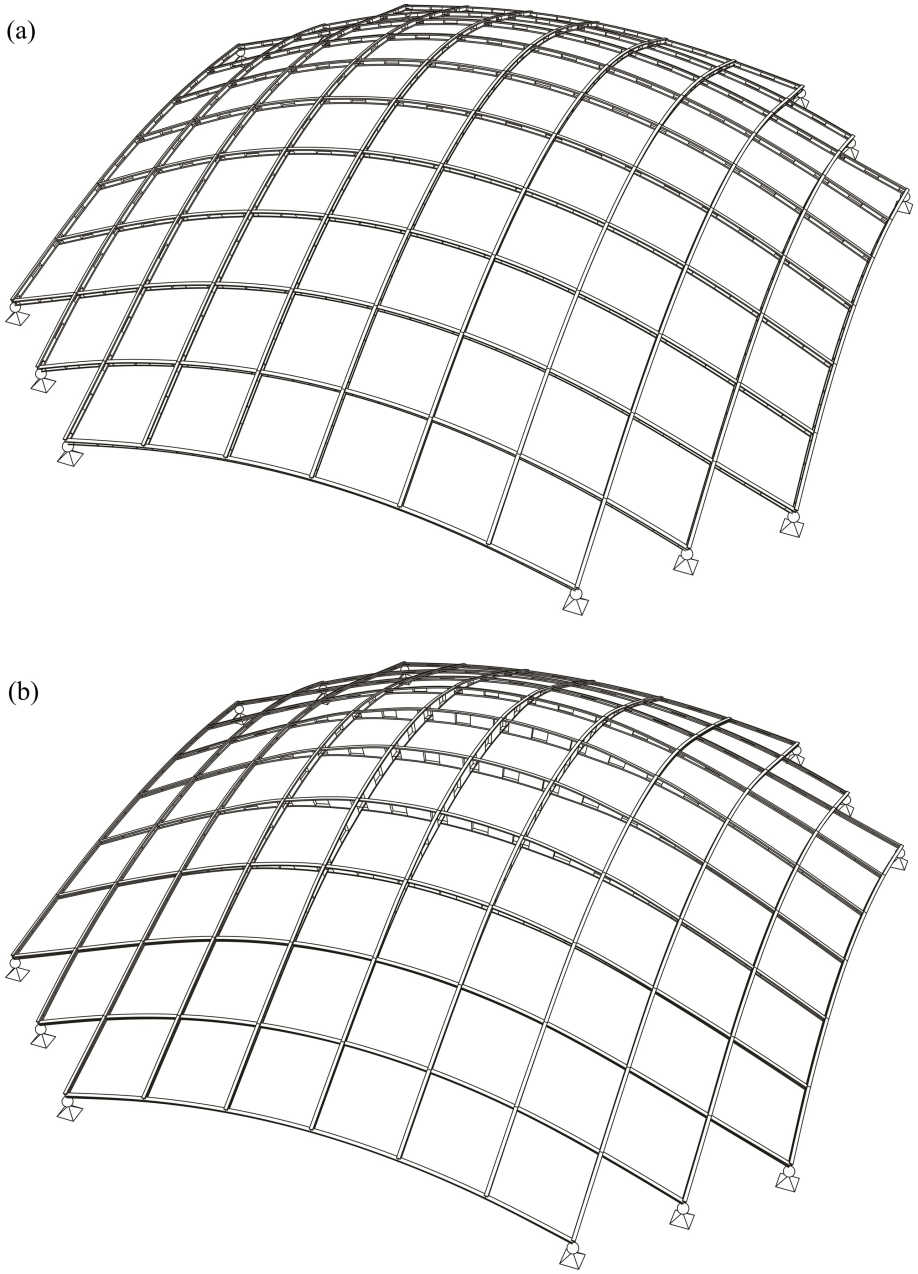


**Figure 5.11:** Grid shell System: (a) Constant cross-section ($h_s = 90$ mm); (b) Optimized cross-section. The variation in thickness and shape for the shear blocks can be handled by Computerised Numerical Control (CNC) milling machinery techniques.

## 5.3 Summary

An opportunity to test the iterative method described in Section 4.1 came out with the construction of a full scale prototype (the Toledo 2.0) in which, the non-linear nature of the thickness/curvature relation was shown to be negligible. In facts, as reported in Table 5.3, the thickness value converged to an 'optimum' (allowable) value so rapidly to suggest the use of a linear expression for the determination of the allowable thickness.

Once the allowable thickness of the single lath is defined, a search for the (overall) thickness of the built-up members can be pursued. For a given load distribution, an optimal thickness variation of the shear blocks (represented by the vector of design space **h**) is sought in order to homogenize the bending stress to a given value $f_m$, thus allowing for optimal material distribution. Strength limit constraints were taken into account in the optimisation problem, as well as 'constructional' constraints, which are expressed in terms of geometric compatibility.

The method's efficiency in finding an optimal distribution of the member's thickness was demonstrated on a single-rod structural system as well as a grid shell framework, for which, a linear variation law $h_s(t)$ was adopted (see Eqs. (4.24 - 4.26)) to allow the inclusion of constructional (geometric) constrains into the optimisation problem. Such linear functions, describing the thickness variation along the elements, can be used to inform the fabrication process by providing a 'trapezoidal' profile ($\pm h_s(t)/2$) for the shear blocks, to be fabricated e.g by CNC cutting machinery, thus allowing minimization of 'gaps' at the connection interface between shear block and upper/lower lath. The gap's reduction at the interfaces, rises the potentials for realization of glued connections for the shear blocks, therefore providing a 'massive' increment of the bending stiffness (as shown by experimental and numerical tests in Section 3.5.3) as well as the vanishing of the

lowering effect (due to pre-stress forces) on the elastic buckling load.

# Part III

# Conclusions

# Chapter 6

# Conclusions

## 6.1 Summary of Contributions

Free-form timber grid-shell structures have many potentials, from many points of view: structural, architectural, constructional, etc. The main drawbacks associated with them are however represented by the challenging and difficult design, and construction. In an effort to overcome such drawbacks, a set of design tools, under the form of numerical models and methods, have been developed within this research work. The issues typically involved within the design process, have been individuated and structured in three main topics, namely: Form-finding; Structural Analysis; Optimisation.

The adoption of a co-rotational beam-element, and its resolution by Dynamic Relaxation scheme, represented the starting point from which building up of an 'organic' framework, to fulfil the Form-finding and Analysis issues, was made. This raised various methodological and practical questions to be clarified and solved. In doing so, the following outcomes were obtained:

- A two-step form-finding procedure that 'actually' takes into account the in-

fluence of internal bending reactions on the formed shape, whilst permitting to decide a-priori (by aid of a reference surface) to what shape the grid-shell must be close to.

- A novel single-node numerical model for the mechanical simulation in large displacements of cylindrical joint connection systems.
- A modified co-rotational beam-element, for the simulation of built-up members, allowing to take into account the change in stiffness occurring when passing from the simulation of the construction (forming) stage to the analysis of the structure under working loads. By only varying two dimensionless parameters, namely: the *connection efficiency factor* $c_s$ and the *relaxation* factor $c_R$, it is possible to:
  - Perform stress verifications of the built-up members.
  - Perform strength verifications of the shear block connections.
  - Assess the lowering effect of pre-stress reaction on the structure's overall stiffness and (elastic) buckling load.

Despite the complex rheology of timber and its variability for effect of several parameters (e.g. specie, moisture content, load duration etc.): the adoption of an orthotropic (transversely isotropic) model allowed to fully represent the elastic stiffness of the structural members only in terms of elastic modulus parallel to the grain and rolling shear modulus.

This work also provided the opportunity to investigate and develop a novel design solution, of double-layer grid-shells with variable cross-section, hence allowing for optimal material distribution. Further investigation are certainly required to assess the practicality of producing and assembling shear blocks with a variable cross-section.

## 6.2 Suggestions for further work

All the numerical examples described in this thesis have been implemented using Python programming language, while the two/three-dimensional graphical outputs, used to produce most of the Figures of this thesis, were obtained by inputting the numerical outputs into commercial CAD software.

In order for the described numerical framework to be used as a design tool, let's say, in a professional design practice situation: its development under the form of a computer software would certainly be required. In such a case, a convenient solution is probably that of developing an interactive environment, which allows for the user to 'virtually' model frameworks of elastic rods, whilst exploring different shapes, and at the same time 'assessing' the corresponding structural behaviour or simulating the construction (forming) process by interactively 'pushing' and 'pulling' some of the nodes, and/or applying forces and displacements hence observing in real-time the response of the structure. Interactive real-time physics has been widely implemented in the last decade by the Computer Graphics community, mostly for computer-game applications. Nevertheless, successful examples of real-time interactive software applications, for the teaching/design of Structures, and based on explicit resolution methods of the acceleration terms (Such as the DR method adopted in here) are for instance: the plug-in for visual scripting *Kangaroo*, developed by Piker [2013], or *PushMePullMe*, developed by Senatore and Piker [2015].

Another suggestion for further work regards the possibility to 'enrich' the described co-rotational formulation, for instance, in order to take into account more complex material's behaviour, such as non-linear elasticity and elastic-plastic behaviour.

# References

S. Adriaenssens and M. Barnes. Tensegrity spline beam and grid shell structures. *Engineering structures*, 23(1):29–36, 2001. Cited on page: 27.

S. Adriaenssens, P. Block, D. Veenendaal, and C. J. Williams, editors. *Shell Structures for Architecture, Form finding and Optimization.* Taylor and Francis, 2014. Cited on pages: 4 and 18.

S. M. L. Adriaenssens. *Stressed spline structures.* PhD thesis, University of Bath, 2000. Cited on pages: 27, 31, 34, 54, and 58.

Y. Aharonov, H. A. Farach, and C. P. Poole Jr. Nonlinear vector product to describe rotations. *American Journal of Physics*, 45(5):451–454, 1977. Cited on pages: 31 and 132.

ASTM. *ASTM D2555-06. Standard Practice for Establishing Clear Wood Strength Values.* American Society for Testing and Materials, 2006. Cited on page: 69.

D. Baraff and A. Witkin. Large steps in cloth simulation. In *Proceedings of the 25th annual conference on Computer graphics and interactive techniques*, pages 43–54. ACM, 1998. Cited on page: 24.

M. R. Barnes. Form finding and analysis of tension structures by dynamic re-

laxation. *International journal of space structures*, 14(2):89–104, 1999. Cited on page: 25.

M. R. Barnes, S. Adriaenssens, and M. Krupka. A novel torsion/bending element for dynamic relaxation modeling. *Computers & Structures*, 119:60–67, 2013. Cited on page: 27.

K.-J. Bathe. *Finite element procedures*. Klaus-Jurgen Bathe, 2006. Cited on page: 25.

K.-J. Bathe and S. Bolourchi. Large displacement analysis of three-dimensional beam structures. *International Journal for Numerical Methods in Engineering*, 14 (7):961–986, 1979. Cited on page: 27.

P. C. V. Block. *Thrust network analysis: exploring three-dimensional equilibrium*. PhD thesis, Massachusetts Institute of Technology, 2009. Cited on page: 14.

A. Bobenko and U. Pinkall. Discrete surfaces with constant negative gaussian curvature and the hirota equation. *Journal of Differential Geometry*, 43(3):527–621, 1996. Cited on page: 65.

J. Bodig and B. A. Jayne. *Mechanics of wood and wood composites*. Van Nostrand Reinhold, 1981. Cited on pages: 52 and 88.

L. Bouhaya, O. Baverel, and J.-F. Caron. Mapping two-way continuous elastic grid on an imposed surface: Application to grid shells. In *Proc. 50th International IASS Symposium, Valencia*. Editorial de la Universitat Politécnica de Valencia., 2010. Cited on page: 22.

BS-EN-338. *BS EN 338:2009. Structural timber - Strength classes*. British Standards Institution, 2008. Cited on page: 69.

BS-EN-408. *BS EN 408:2010+A1:2012. Timber structures. Structural timber and glued laminated timber. Determination of some physical and mechanical properties.* British Standards Institution, 2012. Cited on page: 102.

E. Buckingham. On physically similar systems; illustrations of the use of dimensional equations. *Physical Review*, 4(4):345–376, 1914. Cited on page: 80.

T. Bulenda and J. Knippers. Stability of grid shells. *Computers & Structures*, 79(12): 1161–1174, 2001. Cited on page: 18.

C. R. Calladine. *Theory of shell structures.* Cambridge university press, 1989. Cited on page: 4.

J. C. Chilton and H. Isler. *Heinz isler.* Thomas Telford, 2000. Cited on page: 14.

S. A. Chini and A. M. Wolde-Tinsae. Effect of prestressing on elastica arches. *Journal of engineering mechanics*, 114(10):1791–1800, 1988. Cited on page: 83.

M. A. Crisfield. A consistent co-rotational formulation for non-linear, three-dimensional, beam-elements. *Computer methods in applied mechanics and engineering*, 81(2):131–150, 1990. Cited on page: 27.

P. Cundall. Explicit finite-difference method in geomechanics. *Numerical Methods in Geomechanics*, 1976. Cited on page: 26.

B. D'Amico. Design and building of a post-formed timber gridshell. Master's thesis, University of Naples Federico II, Italy, 2010. Cited on pages: VIII and 15.

M. Dickson and R. Harris. The downland gridshell: Innovative design in timber. *Ingenia*, pages 31–36, 2004. Cited on pages: VII and 10.

P. Domone and J. Illston. *Construction materials: their nature and behaviour.* CRC Press, 2010. Cited on pages: IX and 51.

Eurocode5. *BS EN 1995-1-1:2004+A1:2008: Design of timber structures - Part 1-1: General - Common rules and rules for buildings*. British Standards Institution, 2008. Cited on pages: 47 and 88.

M. Fleischmann and A. Menges. Icd/itke research pavilion: A case study of multi-disciplinary collaborative computational design. In *Computational Design Modelling*, pages 239–248. Springer, 2012. Cited on pages: VII and 6.

P. Frieze, R. Hobbs, and P. Dowling. Application of dynamic relaxation to the large deflection elasto-plastic analysis of plates. *Computers & Structures*, 8(2):301–310, 1978. (Not cited.)

C. Gengnagel, E. L. Hernández, and R. Bäumer. Natural-fibre-reinforced plastics in actively bent structures. *Proceedings of the ICE-Construction Materials*, 166(6): 365–377, 2013. Cited on pages: VIII, 6, and 12.

E. Happold and I. Liddell. Timber lattice roof for the mannheim bundesgartenschau. *The structural engineer*, 53(3):99–135, 1975. Cited on pages: VIII, 8, 10, 18, 25, 78, 81, and 99.

J. Harding, W. Pearson, H. Lewis, and S. Melville. The ongreening pavilion. In *Advances in Architectural Geometry 2014*, pages 295–308. Springer, 2015. Cited on pages: VII and 6.

R. Harris. Design of timber gridded shell structures. *Proceedings of the ICE-Structures and Buildings*, 164(2):105–116, 2011. Cited on page: 7.

R. Harris, S. Johnson, A. Holloway, and C. Zeuner. A coupling and a method of constructing grid shell buildings using such a coupling. Patent GB2361504 (A), 10 2001. Cited on page: 12.

R. Harris, J. Romer, O. Kelly, and S. Johnson. Design and construction of the downland gridshell. *Building Research & Information*, 31(6):427–454, 2003. Cited on pages: 16, 69, 70, and 71.

R. Harris, B. Gusinde, and J. Roynon. Design and construction of the pods sports academy, scunthorpe, england. In *proceedings of the World Conference of Timber Engineering*, pages 510–517, 2012. Cited on pages: VII, 7, and 16.

F. S. Hill. *The Pleasures of Perp. Dot. Products. Ch. II.5 in Graphics Gems IV*. Academic Press, 1994. Cited on page: 73.

P. Hoogenboom. Handouts of the course: Shell Analysis, Theory and Application, Delft University of Technology. 2014. URL http://homepage.tudelft.nl/p3r3s/CT4143_handout_7b.pdf. Cited on pages: VII, 4, and 5.

O. Kelly, R. Harris, M. Dickson, and J. Rowe. The construction of the downland gridshell. *The Structural Engineer*, 79(17):25–33, 2001. Cited on pages: 14 and 69.

A. Kilian and J. Ochsendorf. Particle-spring systems for structural form finding. *Journal of the International Assossation for Shell and Spatial Structures*, 148:77, 2005. Cited on pages: VIII and 14.

J. Koenderink and A. van Doom. Shape from chebyshev nets. In *Computer Vision ECCV 98*, pages 215–225. Springer, 1998. Cited on pages: VIII and 17.

M. Kuijvenhoven and P. Hoogenboom. Particle-spring method for form finding grid shell structures consisting of flexible members. *Journal of the International Association for Shell and Spatial Structures*, 53(1):31–38, 2012. Cited on page: 22.

B. Lewis. Centre pompidou- metz: Enginering the roof. *Structural Engineer*, 89 (18):20–26, 2011. Cited on pages: VIII and 24.

W. J. Lewis. *Tension structures: form and behaviour*. Thomas Telford, 2003. Cited on page: 26.

J.-M. Li and J. Knippers. Form-finding of grid shells with continuous elastic rods. In *Proc. of the International Symposium of the IABSE-IASS Symposium, London, UK*, volume 35, 2011. Cited on page: 22.

J. Lienhard, H. Alpermann, C. Gengnagel, and J. Knippers. Active bending, a review on structures where bending is used as a self-formation process. *International Journal of Space Structures*, 28(3):187–196, 2013. Cited on page: 5.

S. Malek, J. Ochsendorf, and T. Wierzbicki. The effect of double curvature on the structural capacity of corrugated gridshells. In *proceedings of the IASS Symposium, Wroclaw, Poland*, 2013. Cited on page: 3.

A. Mirmiran and A. M. Amde. Effects of fabrication process on prestressed composite arches. *Journal of Structural Engineering*, 121(1):124–131, 1995. Cited on page: 83.

K. Möhler. On the load carrying behavior of beams and columns of compound sections with flexible connections, 1956. Cited on page: 47.

D. Naicu, R. Harris, and C. Williams. Timber gridshells: Design methods and their application to a temporary pavilion. In *World Conference on Timber Engineering*, 2014. Cited on page: 6.

J. Natterer, N. Burger, and A. Müller. Das expo-dach in hannover als pilotprojekt für den holzbau-entwicklung und einsatz nicht geregelter bauweisen. *Bautechnik*, 78(10):693–705, 2001. Cited on page: 8.

P. Nicholas, E. L. Hernández, and C. Gengnagel. The faraday pavilion: activating bending in the design and analysis of an elastic gridshell. In *Proceedings of the*

*Symposium on Simulation for Architecture & Urban Design*, page 21. Society for Computer Simulation International, 2013. Cited on page: 6.

E. Ochsenschlager. Life on the edge of the marshes. *Expedition*, 40(2):29–39, 1998. Cited on pages: VII and 5.

P. Oliver and P. Press. *Dwellings: the vernacular house world wide*. Phaidon London, 2003. Cited on pages: VII and 5.

C. F. Ong. *Computer Aided Design of Tension Structures*. PhD thesis, City University, London, 1992. Cited on page: 27.

F. Otto. IL 13 Multihalle Mannheim. *Institut für leichte Flächentragwerke (IL)*, 1978. Cited on pages: VII and 9.

F. Otto, J. Hennicke, and K. Matsushita. IL 10 Gitterschalen. *Institut für leichte Flächentragwerke (IL)*, 1974. Cited on pages: VIII and 17.

M. Papadrakakis. A method for the automatic evaluation of the dynamic relaxation parameters. *Computer methods in applied mechanics and engineering*, 25(1):35–48, 1981. Cited on page: 29.

D. Piker. Kangaroo: Form finding with computational physics. *Architectural Design*, pages 245–252., 2013. Cited on page: 120.

C. Pirazzi, Y. Weinand, et al. Geodesic lines on free-form surfaces: optimized grids for timber rib shells. In *Proc. World Conference on Timber Engineering*, volume 7, 2006. Cited on page: 7.

S. Pone, B. D'Amico, S. Colabella, B. Parenti, D. Lancia, and A. Fiore et al. Construction and form-finding of a post-formed timber grid-shell. In *Structures and*

*Architecture. Concepts, Applications and challenges*, pages 245–252. CRC Press, 2013. Cited on pages: XII, XIV, 102, 104, and 105.

J. Porteous and A. Kermani. *Structural timber design to Eurocode 5, 2nd edition*. John Wiley & Sons, 2013. Cited on pages: 45 and 88.

M. Rippmann, L. Lachauer, and P. Block. Interactive vault design. *International Journal of Space Structures*, 27(4):219–230, 2012. Cited on pages: VIII and 14.

O. Rodrigues. *De l'attraction des sphéroïdes*. PhD thesis, 1815. Cited on page: 31.

G. Senatore and D. Piker. Interactive real-time physics: An intuitive approach to form-finding and structural analysis for design and education. *Computer-Aided Design*, 61(0):32–41, 2015. Cited on pages: 27 and 120.

J. Thompson and G. W. Hunt. On the buckling and imperfection-sensitivity of arches with and without prestress. *International Journal of Solids and Structures*, 19(5):445–459, 1983. Cited on page: 76.

S. P. Timoshenko and J. M. Gere. *Theory of elastic stability*. McGraw-Hill, 1961. Cited on pages: 60 and 77.

M. Tuckerman, B. J. Berne, and G. J. Martyna. Reversible multiple time scale molecular dynamics. *The Journal of chemical physics*, 97(3):1990–2001, 1992. Cited on page: 29.

D. Wakefield. *Dynamic Relaxation Analysis of pre-tensioned networks supported by compression arches*. PhD thesis, City University, London, 1980. Cited on page: 27.

C. J. Williams. Patterns on a surface: The reconciliation of the circle and the square. *Nexus Network Journal*, 13(2):281–295, 2011. Cited on page: 41.

L. Zhang and T. Yu. Modified adaptive dynamic relaxation method and its application to elastic-plastic bending and wrinkling of circular plates. *Computers & structures*, 33(2):609–614, 1989. (Not cited.)

# Relevant publications of the author

## Refereed journals:

1. **B. D'Amico**, H. Zhang , A. Kermani, A Finite-difference formulation of elastic rod for the design of actively-bent grid-shell structures, *Engineering Structures – Elsevier*, 2015. (Under review).

2. **B. D'Amico**, A. Kermani, H. Zhang, A. Pugnale, S. Colabella, S. Pone, Timber gridshells: Numerical simulation, design and construction of a full scale structure, *Structures – Elsevier*, 3:227–235, 2015. DOI: http://dx.doi.org/10.1016/j.istruc.2015.05.002

3. **B. D'Amico**, A. Kermani, H. Zhang, P. Shepherd, C.J.K. Williams, Optimisation of cross-section of actively bent grid-shells with strength and geometric compatibility constraints, *Computers & Structures – Elsevier*, 154:163–176, 2015. DOI: http://dx.doi.org/10.1016/j.compstruc.2015.04.006

4. **B. D'Amico**, A. Kermani, H. Zhang, Form finding and structural analysis of actively bent timber grid-shells, *Engineering Structures – Elsevier*, 81:195–207, 2014. DOI: http://dx.doi.org/10.1016/j.engstruct.2014.09.043

## Conference proceedings:

5. **B. D'Amico**, A. Kermani, H. Zhang, A form finding method for post-formed timber grid-shells structures, In *proceedings of the World Conference on Timber Engineering (WCTE), Quebec City, Canada*, 2014. DOI: http://dx.doi.org/10.13140/2.1.3949.8888

6. S. Pone, S. Colabella, **B. D'Amico**, A. Fiore, D. Lancia, B. Parenti, Timber post-formed grid-shell: digital form-finding / drawing and building tool, In *proceedings of the International Association for Shell and Spatial Structures (IASS) Symposium, Wroclaw, Poland*, 2013. DOI: http://dx.doi.org/10.13140/2.1.1339.1686

7. S. Pone, **B. D'Amico**, S. Colabella, B. Parenti, D. Lancia, A. Fiore et al, Construction and form-finding of a post-formed timber grid-shell, In *Structures and Architecture. Concepts, Applications and challenges*, 245–252, 2013. DOI: http://dx.doi.org/10.1201/b15267-32

# Appendix A

## A.1: Non-linear vector product

According to Aharonov et al. [1977] the *non-linear vector product* between two vectors $\bar{a}$ and $\bar{b}$ is another vector $\bar{c}$ equal to:

$$\bar{c} = \bar{a} \otimes \bar{b} = \frac{1}{1 - \bar{a} \cdot \bar{b}} (\bar{a} + \bar{b} + \bar{b} \times \bar{a}) \tag{1}$$

## A.2: Corrugated barrel vault shape function

With reference to the shape function of the corrugated barrel vault in Section 3.3: the vertical $z$ component of the reference surface is obtained by superposition of multiple function values. Writing $f(\bar{r}) = f(x, y, z) = 0$ in the form $f(x, y) = z$, we have:

$$z = f = f_1 + f_2 + f_3 + c \tag{2}$$

where:

$$\begin{aligned} f_1 &= -\cosh\left(\frac{x}{2.55}\right) \quad ; \quad f_2 = \cosh\left(\frac{x}{4.1}\right)\cos\left(\frac{y}{3}\right) \\ f_3 &= -\left(\frac{x^2}{50} + \frac{y^2}{665}\right) \quad ; \quad c = 9.55 \end{aligned} \tag{3}$$

The main barrel vault is shaped with $f_1$ while $f_2$ provides the corrugated profile

and $f_3$ takes into account the occurring height difference between the central dome and the lateral ones (see Figure 1) the constant $c$ translates vertically the surface so that the global $(x, y)$ plane coincides to the structure's ground floor.

From Eqs. (3) the partial derivatives of $f(\bar{r})$ to insert in Eq. (2.48) to compute the vector normal to the surface, result to be:

$$\begin{aligned} \frac{\partial f}{\partial x} &= -\frac{1}{2.55}\sinh\left(\frac{x}{2.55}\right) + \frac{1}{4.1}\sinh\left(\frac{x}{4.1}\right)\cos\left(\frac{y}{3}\right) - \frac{x}{25} \\ \frac{\partial f}{\partial y} &= -\frac{1}{3}\cosh\left(\frac{x}{4.1}\right)\sin\left(\frac{y}{3}\right) - \frac{y}{332.5} \\ \frac{\partial f}{\partial z} &= -1 \end{aligned} \tag{4}$$

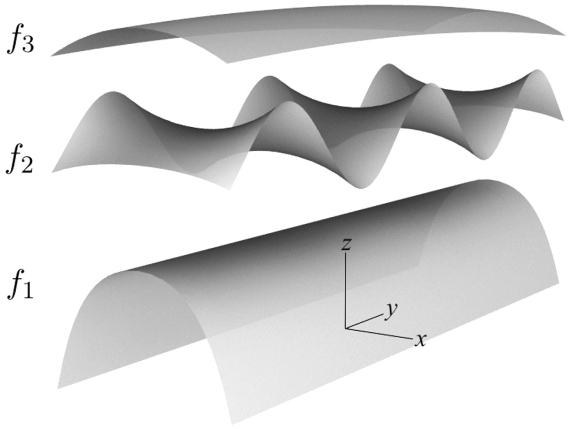


**Figure 1:** Corrugated barrel vault: $f(\bar{r}) = f_1 + f_2 + f_3 + c$.

# Appendix B: Rhino.Python code

As an 'example' of the implemented numerical methods, the Python code written for the numerical test described in Section 3.1.1 of this thesis, is reported as follows. Please, contact the author at: B.D'Amico@napier.ac.uk if looking for the code of (all) the remaining numerical examples reported in this thesis.

## B.1: Elastica

```
import rhinoscriptsyntax as rs
import math
import Rhino
import array
import System
import clr
import sys
import time
import scriptcontext
import os

rs.UnitAbsoluteTolerance(1e-50, True)
rs.UnitAngleTolerance(0.0001, True)
rs.UnitRelativeTolerance(0.01, True)
def draw_loc_sist(vertex_list, loc_axces):
    for i in range(0, len(vertex_list)):
        a = [vertex_list[i][0], vertex_list[i][1], vertex_list[i][2]]
        b = [vertex_list[i][0] + loc_axces[i][0][0]*200, vertex_list[i][1]
        + loc_axces[i][0][1]*200, vertex_list[i][2] + loc_axces[i][0][2]*200]
        rs.AddLine(a, b)

        a = [vertex_list[i][0], vertex_list[i][1], vertex_list[i][2]]
        b = [vertex_list[i][0] + loc_axces[i][1][0]*200, vertex_list[i][1]
        + loc_axces[i][1][1]*200, vertex_list[i][2] + loc_axces[i][1][2]*200]
        rs.AddLine(a, b)

        a = [vertex_list[i][0], vertex_list[i][1], vertex_list[i][2]]
        b = [vertex_list[i][0] + loc_axces[i][2][0]*200, vertex_list[i][1]
        + loc_axces[i][2][1]*200, vertex_list[i][2] + loc_axces[i][2][2]*200]
        rs.AddLine(a, b)
    return
def draw_spline(vertex_list, loc_axces, edge_list):
    tot_length = 0.0
    for i in range(0, len(edge_list)):
        P_min = [vertex_list[edge_list[i][0]][0], vertex_list[edge_list[i][0]][1],
        vertex_list[edge_list[i][0]][2]]
        P_plus = [vertex_list[edge_list[i][1]][0], vertex_list[edge_list[i][1]][1],
```

```
        vertex_list[edge_list[i][1]][2]]
        z_min = loc_axces[edge_list[i][0]][2]
        z_plus = loc_axces[edge_list[i][1]][2]
        pp = [P_min, P_plus]
        c = rs.AddInterpCurve(pp, 3, 0, z_min, z_plus)
        tot_length = tot_length + rs.CurveLength(c)
    c = rs.AddInterpCurve(pp, 3, 0, z_min, z_plus)
    return

def draw_kin_en(cicle, plus_Tot_kin_ene, scale, z0):
    x = cicle
    y = 0.0
    z = (plus_Tot_kin_ene / scale) + z0
    rs.AddPoint(x, y, z)
    return

def elem_loc_displacem(vertex_list, edge_list, loc_axces, L0):
    elem_local_disps = []
    for i in range(0, len(edge_list)):
        P_min = [vertex_list[edge_list[i][0]][0], vertex_list[edge_list[i][0]][1],
        vertex_list[edge_list[i][0]][2]]
        P_plus = [vertex_list[edge_list[i][1]][0], vertex_list[edge_list[i][1]][1],
        vertex_list[edge_list[i][1]][2]]
        vec_p = rs.VectorCreate(P_plus, P_min)

        vec_x_min = loc_axces[edge_list[i][0]][0]
        vec_y_min = loc_axces[edge_list[i][0]][1]
        vec_z_min = loc_axces[edge_list[i][0]][2]

        rho_x_min = -((rs.VectorDotProduct(vec_y_min, vec_p)) /
        rs.VectorLength(vec_p))
        rho_y_min = ((rs.VectorDotProduct(vec_x_min, vec_p)) /
        rs.VectorLength(vec_p))

        vec_x_plus = loc_axces[edge_list[i][1]][0]
        vec_y_plus = loc_axces[edge_list[i][1]][1]
        vec_z_plus = loc_axces[edge_list[i][1]][2]

        rho_x_plus = -((rs.VectorDotProduct(vec_y_plus, vec_p)) /
        rs.VectorLength(vec_p))
        rho_y_plus = ((rs.VectorDotProduct(vec_x_plus, vec_p)) /
        rs.VectorLength(vec_p))

        phi = -(((rs.VectorDotProduct(vec_x_min, vec_y_plus) -
        rs.VectorDotProduct(vec_x_plus, vec_y_min)) / 2.0))

        e = (math.pow(rs.VectorLength(vec_p), 2.0) - math.pow(L0, 2.0) +
        (math.pow(L0, 2.0) / 30.0) * ((4.0 * (math.pow(rho_x_min, 2.0)) +
        math.pow(rho_y_min, 2.0)) - 2.0 * ((rho_x_min * rho_x_plus) +
        (rho_y_min * rho_y_plus)) + (4.0 * (math.pow(rho_x_plus, 2.0)) +
        math.pow(rho_y_plus, 2.0)))) / (2.0 * L0)

        item = [rho_x_min, rho_y_min, rho_x_plus, rho_y_plus, phi, e, vec_p]
        elem_local_disps.append(item)

    return elem_local_disps

def measure_elem_length(L0, loc_disp):
    tot_length = 0.0
    for i in range(0, len(loc_disp)):
        e = loc_disp[i][5]
        current_length = L0 + e
        tot_length = tot_length + current_length
    print "average lenght elem =", tot_length / len(loc_disp),
    "tot lenght =", tot_length
    return

def elem_loc_forces(loc_disp, L0, E, Ix, Iy, G, tor_const, A):
    elem_forces = []
    for i in range(0, len(loc_disp)):
        rho_x_min = loc_disp[i][0]
        rho_y_min = loc_disp[i][1]
        rho_x_plus = loc_disp[i][2]
        rho_y_plus = loc_disp[i][3]
        phi = loc_disp[i][4]
        vec_p = loc_disp[i][6]
        e = loc_disp[i][5]

        N = E * A * (e / L0)
        M_x_min = (((N * L0) / 30.0) * ((4 * rho_x_min) - rho_x_plus) +
        ((E * Ix) / L0) * ((4 * rho_x_min) + (2 * rho_x_plus)))
        M_x_plus = (((N * L0) / 30.0) * ((4 * rho_x_plus) - rho_x_min) +
```

```
        ((E * Ix) / L0) * ((4 * rho_x_plus) + (2 * rho_x_min)))
        M_y_min = (((N * L0) / 30.0) * ((4 * rho_y_min) - rho_y_plus) +
        ((E * Iy) / L0) * ((4 * rho_y_min) + (2 * rho_y_plus)))
        M_y_plus = (((N * L0) / 30.0) * ((4 * rho_y_plus) - rho_y_min) +
        ((E * Iy) / L0) * ((4 * rho_y_plus) + (2 * rho_y_min)))
        M_phi = (G * tor_const * phi) / L0

        elem_forces.append([M_x_min, M_y_min, M_x_plus, M_y_plus, M_phi, N, vec_p])

    return elem_forces
def elem_Global_forces(loc_forces, loc_axces, L0):
    #Output: for the generic "j" element ID there are two lists which
    #corresponding items are:
    # {[F1x, F1y, F1z], [F2x, F2y, F2z]}  for the j element
    # {[M1x, M1y, M1z], [M2x, M2y, M2z]}  for the j element
    elem_gl_forces = []
    elem_gl_moments = []
    for i in range(0, len(loc_forces)):
        M_x_min = loc_forces[i][0]
        M_y_min = loc_forces[i][1]
        M_x_plus = loc_forces[i][2]
        M_y_plus = loc_forces[i][3]
        M_phi = loc_forces[i][4]
        N = loc_forces[i][5]
        vec_p = loc_forces[i][6]

        x_loc_min = loc_axces[edge_list[i][0]][0]
        y_loc_min = loc_axces[edge_list[i][0]][1]
        z_loc_min = loc_axces[edge_list[i][0]][2]

        x_loc_plus = loc_axces[edge_list[i][1]][0]
        y_loc_plus = loc_axces[edge_list[i][1]][1]
        z_loc_plus = loc_axces[edge_list[i][1]][2]

        Axial = rs.VectorScale(vec_p, N / rs.VectorLength(vec_p))
        #print "A", Axial
        M_Glob_min = (rs.VectorScale(x_loc_min, M_x_min) +
        rs.VectorScale(y_loc_min, M_y_min) + rs.VectorScale(z_loc_min, M_phi))
        M_Glob_plus = (rs.VectorScale(x_loc_plus, M_x_plus) +
        rs.VectorScale(y_loc_plus, M_y_plus) - rs.VectorScale(z_loc_plus, M_phi))

        M_Glob = rs.VectorAdd(M_Glob_min, M_Glob_plus)
        v = rs.VectorScale(rs.VectorCrossProduct(M_Glob, vec_p), 1 /
        (rs.VectorLength(rs.VectorCrossProduct(M_Glob, vec_p)) + 1e-300))
        Shear = rs.VectorScale(v, ((rs.VectorLength(M_Glob) * rs.VectorLength(M_Glob) *
        rs.VectorLength(rs.VectorCrossProduct(vec_p, v))) / (rs.VectorLength(vec_p) *
        (1e-300 + rs.VectorDotProduct(M_Glob, rs.VectorCrossProduct(vec_p, v))))))
        Shear = rs.VectorScale(Shear, 1.0)

        F_Glob_min = rs.VectorAdd(Axial, Shear)
        F_Glob_plus = rs.VectorReverse(F_Glob_min)

        Forces = [[F_Glob_min[0], F_Glob_min[1], F_Glob_min[2]], [F_Glob_plus[0],
        F_Glob_plus[1], F_Glob_plus[2]]]
        #print Forces
        elem_gl_forces.append(Forces)

        Moments = [[M_Glob_min[0], M_Glob_min[1], M_Glob_min[2]], [M_Glob_plus[0],
        M_Glob_plus[1], M_Glob_plus[2]]]
        #print Moments
        elem_gl_moments.append(Moments)

    elem_gl = [elem_gl_forces, elem_gl_moments]
    return elem_gl
def Out_of_bal_Forces(vertex_list, gl_forces, cic, iteraz):
    R = []
    magnitude = []
    for i in range(0, len(vertex_list)):
        edge_min = vertex_list[i][3]
        edge_plus = vertex_list[i][4]

        if edge_min is not False:
            F_min = gl_forces[edge_min][1]
        else:
            F_min = [0.0, 0.0, 0.0]
        if edge_plus is not False:
            F_plus = gl_forces[edge_plus][0]
        else:
            F_plus = [0.0, 0.0, 0.0]

        Res = rs.VectorAdd(F_min, F_plus)

        P1 = [18594.3346917, 0.0, 0.0]  #Load applied at rod-start
```

```
        P2 = [-18594.3346917, 0.0, 0.0] #Load applied at rod-end
        if i == 0:
            Res = rs.VectorAdd(Res, P1)
        if i == len(vertex_list) - 1:
            Res = rs.VectorAdd(Res, P2)
        R.append(Res)
        magnitude.append(rs.VectorLength(Res))

    #print "R res =", magnitude
    return R
def Out_of_bal_Moments(vertex_list, gl_moment, cic, iteraz):
    H = []
    magnitude = []
    for i in range(0, len(vertex_list)):
        edge_min = vertex_list[i][3]
        edge_plus = vertex_list[i][4]
        if edge_min is not False:
            M_min = gl_moment[edge_min][1]
        else:
            M_min = [0.0, 0.0, 0.0]
        if edge_plus is not False:
            M_plus = gl_moment[edge_plus][0]
        else:
            M_plus = [0.0, 0.0, 0.0]
        Res = rs.VectorAdd(M_min, M_plus)
        H.append(Res)
        magnitude.append(rs.VectorLength(Res))

    #print "M res =", magnitude
    return H
def reset_zero(node_List):
    listZeroVal = []
    for i in range(0, len(node_List)):
        if node_List[i] is False:
            listZeroVal.append(False)
        else:
            listZeroVal.append([0.0, 0.0, 0.0])
    return listZeroVal
def updat_vel(old_vel, trans_masses, trans_res, C_t, time_step):
    new_vel = []
    for i in range(0, len(old_vel)):
        if old_vel[i] is False:
            new_vel.append(False)
        else:
            vel_x = ((C_t * old_vel[i][0]) + ((trans_res[i][0] /
            (trans_masses[i][0])) * time_step))
            vel_y = ((C_t * old_vel[i][1]) + ((trans_res[i][1] /
            (trans_masses[i][1])) * time_step))
            vel_z = ((C_t * old_vel[i][2]) + ((trans_res[i][2] /
            (trans_masses[i][2])) * time_step))
            new_vel.append([vel_x, vel_y, vel_z])
    return new_vel
def updat_rot_vel(old_vel, masses, res, C_r, time_step):
    new_vel = []
    for i in range(0, len(old_vel)):
        if old_vel[i] is False:
            new_vel.append(False)
        else:
            vel_x = ((C_r * old_vel[i][0]) + ((res[i][0] /
            (masses[i][0])) * time_step))
            vel_y = ((C_r * old_vel[i][1]) + ((res[i][1] /
            (masses[i][1])) * time_step))
            vel_z = ((C_r * old_vel[i][2]) + ((res[i][2] /
            (masses[i][2])) * time_step))
            new_vel.append([vel_x, vel_y, vel_z])
    return new_vel
def updat_geometry(old_coords, vel):
    new_coords = []
    for i in range(0, len(old_coords)):
        new_coords_x = old_coords[i][0] + (time_step * vel[i][0])
        new_coords_y = old_coords[i][1] + (time_step * vel[i][1])
```

```
            new_coords_z = old_coords[i][2] + (time_step * vel[i][2])
            new_coords.append([new_coords_x, new_coords_y, new_coords_z,
            old_coords[i][3], old_coords[i][4]])
        return new_coords

    def updat_angleRot(old_rots, rot_vel):
        new_rots = []
        for i in range(0, len(old_rots)):
            if old_rots[i] is not False:
                new_rots_x = (time_step * rot_vel[i][0])
                new_rots_y = (time_step * rot_vel[i][1])
                new_rots_z = (time_step * rot_vel[i][2])
                new_rots.append([new_rots_x, new_rots_y, new_rots_z])
            else:
                new_rots.append(False)
        return new_rots

    def rotationMatrix_A(x, y, z, rox, roy, roz):

        #inputs: three unit vectors representing the node local coordinates
        #        three angles representing the nodal rotations of the new iteration
        #output: the update unit vectors coordinates

        try:
            vec_rox = [math.tan(rox/2.0), 0.0, 0.0]
        except:
            vec_rox = [math.tan(math.pi/2), 0.0, 0.0]
        try:
            vec_roy = [0.0, math.tan(roy/2.0), 0.0]
        except:
            vec_roy = [0.0, math.tan(math.pi/2), 0.0]
        try:
            vec_roz = [0.0, 0.0, math.tan(roz/2.0)]
        except:
            vec_roz = [0.0, 0.0, math.tan(math.pi/2)]

        a = vec_rox
        b = vec_roy

        c = ((rs.VectorAdd(a, b) + rs.VectorCrossProduct(b, a)) /
        (1.0 - rs.VectorDotProduct(a, b)))
        d = ((rs.VectorAdd(c, vec_roz) + rs.VectorCrossProduct(vec_roz, c)) /
        (1.0 - rs.VectorDotProduct(c, vec_roz)))
        alpha = math.atan(2.0 * rs.VectorLength(d))

        cos = math.cos(alpha)
        sin = math.sin(alpha)

        A1 = [cos, 0.0, 0.0]
        A2 = [0.0, cos, 0.0]
        A3 = [0.0, 0.0, cos]

        sec = (1.0 - cos) / (math.pow(rs.VectorLength(d), 2.0) + 1e-400)

        B1 = [sec * d[0] * d[0], sec * d[0] * d[1], sec * d[0] * d[2]]
        B2 = [sec * d[1] * d[0], sec * d[1] * d[1], sec * d[1] * d[2]]
        B3 = [sec * d[2] * d[0], sec * d[2] * d[1], sec * d[2] * d[2]]

        ter = sin / (rs.VectorLength(d) + 1e-400)

        C1 = [0.0, (-1.0 * d[2] * ter), (d[1] * ter)]
        C2 = [(d[2] * ter), 0.0, (-1.0 * d[0] * ter)]
        C3 = [(-1.0 * d[1] * ter), (d[0] * ter), 0.0]

        a11 = A1[0] + B1[0] + C1[0]
        a12 = A1[1] + B1[1] + C1[1]
        a13 = A1[2] + B1[2] + C1[2]

        a21 = A2[0] + B2[0] + C2[0]
        a22 = A2[1] + B2[1] + C2[1]
        a23 = A2[2] + B2[2] + C2[2]

        a31 = A3[0] + B3[0] + C3[0]
        a32 = A3[1] + B3[1] + C3[1]
        a33 = A3[2] + B3[2] + C3[2]

        xx = a11 * x[0] + a12 * x[1] + a13 * x[2]
        xy = a21 * x[0] + a22 * x[1] + a23 * x[2]
        xz = a31 * x[0] + a32 * x[1] + a33 * x[2]

        yx = a11 * y[0] + a12 * y[1] + a13 * y[2]
        yy = a21 * y[0] + a22 * y[1] + a23 * y[2]
        yz = a31 * y[0] + a32 * y[1] + a33 * y[2]

        zx = a11 * z[0] + a12 * z[1] + a13 * z[2]
        zy = a21 * z[0] + a22 * z[1] + a23 * z[2]
        zz = a31 * z[0] + a32 * z[1] + a33 * z[2]

        xnew = [xx, xy, xz]
```

```
    ynew = [yx, yy, yz]
    znew = [zx, zy, zz]

    new_local_axes = [xnew, ynew, znew]
    return new_local_axes

def updat_local_sys(local_ref_el, rot_angle):
    new_list = []
    for i in range(0, len(local_ref_el)):
        if local_ref_el[i] is not False:
            x = local_ref_el[i][0]
            y = local_ref_el[i][1]
            z = local_ref_el[i][2]
            rox = rot_angle[i][0]
            roy = rot_angle[i][1]
            roz = rot_angle[i][2]

            new_loc_ref = rotationMatrix_A(x, y, z, rox, roy, roz)
        else:
            new_loc_ref = False
        new_list.append(new_loc_ref)
    return new_list

def Enforce_local_sys(local_ref_el, vertex_list):

    for i in range(1, len(local_ref_el) - 1):

        x = local_ref_el[i][0]
        y = local_ref_el[i][1]
        z = local_ref_el[i][2]

        node_plus = [vertex_list[i + 1][0], vertex_list[i + 1][1],
        vertex_list[i + 1][2]]
        node_min = [vertex_list[i - 1][0], vertex_list[i - 1][1],
        vertex_list[i - 1][2]]
        z = rs.VectorUnitize(rs.VectorSubtract(node_plus, node_min))
        y = rs.VectorCrossProduct(z, x)

        local_ref_el[i] = [x, y, z]
    return

def Tot_kinetic_en(vertex_list, Trns_masses, Rot_masses, trans_vel, rot_vel):
    ROT_Tot_kin_en = 0.0
    TRN_Tot_kin_en = 0.0
    for i in range(0, len(vertex_list)):
        mass_x = Trns_masses[i][0]
        mass_y = Trns_masses[i][1]
        mass_z = Trns_masses[i][2]

        rot_mass_x = Rot_masses[i][0]
        rot_mass_y = Rot_masses[i][1]
        rot_mass_z = Rot_masses[i][2]

        vel_x = trans_vel[i][0]
        vel_y = trans_vel[i][1]
        vel_z = trans_vel[i][2]

        rot_vel_x = rot_vel[i][0]
        rot_vel_y = rot_vel[i][1]
        rot_vel_z = rot_vel[i][2]

        trn_kin_en = (1.0 / 2.0) * ((mass_x * vel_x * vel_x) +
        (mass_y * vel_y * vel_y) + (mass_z * vel_z * vel_z))
        rot_kin_en = (1.0 / 2.0) * ((rot_mass_x * rot_vel_x * rot_vel_x) +
        (rot_mass_y * rot_vel_y * rot_vel_y) + (rot_mass_z * rot_vel_z * rot_vel_z))

        ROT_Tot_kin_en = ROT_Tot_kin_en + rot_kin_en
        TRN_Tot_kin_en = TRN_Tot_kin_en + trn_kin_en

    return [ROT_Tot_kin_en, TRN_Tot_kin_en]

def Masses(vertex_list, elem_local_disps, E, A, time_step, elem_forces, L0):
    scale_f = 1.0
    M = []
    for i in range(0, len(vertex_list)):
        edge_min = vertex_list[i][3]
        edge_plus = vertex_list[i][4]

        vec_p_min = elem_local_disps[edge_min][6]
        vec_p_plus = elem_local_disps[edge_plus][6]
        N_min = elem_forces[edge_min][5]
        N_plus = elem_forces[edge_plus][5]

        if edge_min is not False:
```

```
            S_min = ((E * A) / L0) + (abs(N_min) * 0.015)
        else:
            S_min = 0.0
        if edge_plus is not False:
            S_plus = ((E * A) / L0) + (abs(N_plus) * 0.015)
        else:
            S_plus = 0.0

        S = S_min + S_plus

        mass_x = ((time_step * time_step * S) / 2.0) * scale_f
        mass_y = ((time_step * time_step * S) / 2.0) * scale_f
        mass_z = ((time_step * time_step * S) / 2.0) * scale_f

        M.append([mass_x, mass_y, mass_z])
    return M

def rot_Masses(vertex_list, E, A, time_step, L0, Ix, Iy, G, tor_const):
    scale_f = 50
    Rot_M = []
    for i in range(0, len(vertex_list)):
        edge_min = vertex_list[i][3]
        edge_plus = vertex_list[i][4]

        if edge_min is not False:
            S_min = ((E * Ix) + (E * Iy) + (G * tor_const)) / L0
        else:
            S_min = 0.0
        if edge_plus is not False:
            S_plus = ((E * Ix) + (E * Iy) + (G * tor_const)) / L0
        else:
            S_plus = 0.0

        S = S_min + S_plus

        rot_m_x = ((time_step * time_step * S) / 2.0) * scale_f
        rot_m_y = ((time_step * time_step * S) / 2.0) * scale_f
        rot_m_z = ((time_step * time_step * S) / 2.0) * scale_f

        Rot_M.append([rot_m_x, rot_m_y, rot_m_z])
    return Rot_M

def Create_Vertices(div):
    list = []
    for i in range(0, len(div)):
        vx = div[i][0]
        vy = div[i][1]
        vz = div[i][2]
        if i == 0: edge_min = False
        else: edge_min = i - 1
        if i == len(div) - 1: edge_plus = False
        else: edge_plus = i
        list.append([vx, vy, vz, edge_min, edge_plus])
    return list

def Create_Edges(numb):
    list = []
    for i in range(0, numb):
       v_min = i
       v_plus = i + 1
       list.append([v_min, v_plus])
    return list

def Create_loc_axes(vertex):
    list = []
    for i in range(0, len(vertex)):
        vec_y = rs.VectorUnitize(rs.VectorCreate([vertex[i][0], vertex[i][1],
        vertex[i][2]], [0.0,0.0,0.0]))
        vec_x = [0.0,1.0,0.0]
        vec_z = rs.VectorCrossProduct(vec_x, vec_y)
        list.append([vec_x, vec_y, vec_z])
    return list


Length_spline = 10000.0
Elem_numb = 10

r = Length_spline / math.pi
arc = rs.AddArc3Pt([-r,0.0,0.0], [r,0.0,0.0], [0.0,0.0,r])
div = rs.DivideCurve(arc, Elem_numb, False, True)
rs.DeleteObject(arc)

vertex_list = Create_Vertices(div)
edge_list = Create_Edges(Elem_numb)
```

```
loc_axces = Create_loc_axes(vertex_list)
E = 10000.0             #[N/mm^2] --> 1.0e+7[kN/m^2]
A = 10000.0             #[mm^2]   --> 1.0e-2[m^2]
Ix = 10000000.0         #[mm^4]   --> 1.0e-5[m^4]
Iy = 10000000.0
G = 600.0
tor_const = 420175.0
L0 = (Length_spline / Elem_numb)
time_step = 1.0
C_t = 0.95
C_r = 0.95



rot_vel = reset_zero(vertex_list)
trans_vel = reset_zero(vertex_list)
angles_rot = reset_zero(vertex_list)
ROT_min_tot_kin_ene = 0.0
ROT_min_2_tot_kin_ene = 0.0
TRN_min_tot_kin_ene = 0.0
TRN_min_2_tot_kin_ene = 0.0
Damp_rot = False
Damp_trn = False
factor = 1
a = factor
iter = 100
for cicle in range(0, iter):

    loc_disp = elem_loc_displacem(vertex_list, edge_list, loc_axces, L0)
    loc_forces = elem_loc_forces(loc_disp, L0, E, Ix, Iy, G, tor_const, A)


    if cicle == 0:
        Trns_masses = Masses(vertex_list, loc_disp, E, A, time_step, loc_forces,
        L0)
        print Trns_masses
        Rot_masses = rot_Masses(vertex_list, E, A, time_step, L0, Ix, Iy, G,
        tor_const)
        print Rot_masses

    gl_out = elem_Global_forces(loc_forces, loc_axces, L0)
    gl_forces = gl_out[0]
    gl_moment = gl_out[1]
    R = Out_of_bal_Forces(vertex_list, gl_forces, cicle, iter)
    R[Elem_numb] = [R[Elem_numb][0],0.0,0.0]
    R[0] = [R[0][0],0.0,0.0]
    R[int(Elem_numb/2)] = [0.0, 0.0, R[int(Elem_numb/2)][2]]

    trans_vel = updat_vel(trans_vel, Trns_masses, R, C_t, time_step)
    H = Out_of_bal_Moments(vertex_list, gl_moment, cicle, iter)
    rot_vel = updat_rot_vel(rot_vel, Rot_masses, H, C_r, time_step)
    vertex_list = updat_geometry(vertex_list, trans_vel)
    angles_rot = updat_angleRot(angles_rot, rot_vel)
    loc_axces = updat_local_sys(loc_axces, angles_rot)
    if cicle == a:
        draw_spline(vertex_list, loc_axces, edge_list)
        a = a + factor
        print "R[0][0] = ", R[0][0]
        print "R[Elem_numb][0] =", R[Elem_numb][0]

    if cicle > 5000 and abs(R[0][0]) < 0.1 and abs(R[Elem_numb][0]) < 0.1:
        print "R[0][0] = ", R[0][0]
        print "R[Elem_numb][0] =", R[Elem_numb][0]
        break

draw_loc_sist(vertex_list, loc_axces)
draw_spline(vertex_list, loc_axces, edge_list)
measure_elem_length(L0, loc_disp)
print "L0 =", L0
```